USC–SIPI REPORT #442

IMPROVED BRAIN DYNAMIC CONTRAST ENHANCED MRI USING MODEL-BASED RECONSTRUCTION

By

Yi Guo

August 2017

Signal and Image Processing Institute
UNIVERSITY OF SOUTHERN CALIFORNIA
USC Viterbi School of Engineering
Department of Electrical Engineering-Systems
3740 McClintock Avenue, Suite 400
Los Angeles, CA 90089-2564 U.S.A.

Dedicated to my parents and my wife

Acknowledgments

A great many people have helped me and guided me in completing this thesis, without them it is never possible for me to achieve what I have done today, and I would hope to express my deepest gratitude to these people with this opportunity.

I would like to offer my deepest and most sincere gratitude to my advisor and mentor, Professor Krishna S. Nayak. He is truly an exceptional researcher and an excellent teacher, who taught me many things in research and in personal development. He is always optimistic, funny, and helpful, and his guidance and encouragement help me overcome many difficulties and achieve multiple milestones throughout my PhD. I am forever indebted to him for his help and support in completing my graduate studies.

I would also like to thank Professor Justin P. Haldar for serving on my doctoral committee. His rigorous mathematical knowledge and insight has helped me greatly in times I am stuck with algorithm design and performance. I also learned a great many MRI imaging and reconstruction knowledge from his MRI class and vector space class.

I am also thankful to Professor Hao Li for serving on my doctoral committee. His valuable comments and feedback offered me insightful thoughts on my project, and helped me think the fundamentals of my research topic and the potential impact.

I am thankful to Dr Meng Law, who helped me with scheduling and scanning patients in USC hospital. I am also grateful to learn many clinical knowledge and radiology practice from the helpful discussion with him.

I am also thankful to Dr Mark S. Shiroishi. He is kind and patient in helping me rate image quality of our proposed MRI technique. I also learned a lot about the clinical side of MRI imaging through the collaboration with him in scanning patients.

I am also very grateful to Dr R. Marc Lebel, who helped and collaborated with me throughout my entire PhD study. I have inherited his post-doc project at USC for a smooth start of my PhD journey, and he offered tremendous help in many aspects of my research with his solid knowledge in both clinical and mathematical part of MRI.

I would also like to give my special thanks to Dr Sajan Goud Lingala, who collaborated closely with me in the DCE-MRI project. His solid knowledge in MRI image reconstruction helped me immensely in developing and debugging my algorithms. He is also very kind, patient and helpful, making every discussion easy and fruitful.

I am also privileged to be part of the lively and friendly MREL family. I am grateful to every past and present member. I would like to thank Weiyi Chen, Ahsan Javed, Vanessa Landes, Yannick Bliesener, Yongwan Lim, Ziyue (Brian) Wu, Hung Phi Do and Eamon Doyle for their continuous help and support. I also hope to give my special thanks to Terrence Jao, Yinghua Zhu, and Xin Miao, who helped me greatly in both my research and personal life. I would also like to thank my friends outside the lab for helping me overcome various difficulties during my stay here at USC.

Most importantly, I am deeply grateful to my parents and my wife for their unfailing love, support and the sacrifice they made to help me fulfill my PhD study and realize my dream.

Table of Contents

List of Publications

Journal Articles

1. **Yi Guo**, Sajan Goud Lingala, Yannick Bliesener, R. Marc Lebel, Yinghua Zhu, Krishna S. Nayak. Joint arterial input function and tracker kinetic parameter estimation from under-sampled DCE-MRI using a model consistency constraint. *Magnetic Resonance in Medicine* (in revision)
2. Sajan Goud Lingala, **Yi Guo**, Yinghua Zhu, Robert Marc Lebel, Meng Law, Krishna S. Nayak. Tracer Kinetic Models as Temporal Constraints during DCE-MRI reconstruction, *Medical Physics* (in revision)
3. **Yi Guo**, Sajan Goud Lingala, Yinghua Zhu, R Marc Lebel, Krishna S Nayak. Direct Estimation of Tracer-Kinetic Parameter Maps from Highly Under-sampled Brain DCE-MRI, M*agnetic Resonance in Medicine* DOI: 10.1002/mrm.26540
4. **Yi Guo**, R Marc Lebel, Yinghua Zhu, Sajan Goud Lingala, Mark S. Shiroishi, Meng Law, Krishna S. Nayak. High-resolution Whole-brain DCE-MRI Using Constrained Reconstruction: Prospective Clinical Evaluation in Brain Tumor Patients, *Medical Physics,* 43 (2016): 2013-2023
5. Y Zhu, **Y Guo**, SG Lingala, RM Lebel, M Law, KS Nayak. GOCART: GOlden-angle CArtesian Randomized Time-resolved 3D MRI. *Magnetic Resonance Imaging* 34.7 (2016): 940-950
6. Xin Miao, **Yi Guo**, Terrence Jao, Muhammad Usman, Claudia Prieto, Sajan Goud Lingala, Krishna S Nayak. Accelerated Cardiac CINE MRI Using Locally Low Rand and Finite Difference Constraints, *Magnetic Resonance Imaging* 34.6 (2016): 707-714.

Invited papers

1. **Yi Guo**, Yinghua Zhu, Sajan Goud Lingala, R. Marc Lebel, Mark Shiroishi, Meng Law and Krishna Nayak. High-resolution whole-brain dynamic contrast-enhanced MRI using compressed sensing, 3 August 2015, *SPIE Newsroom.* DOI: 10.1117/2.1201507.006016

Conference Papers

1. **Yi Guo**, Sajan Goud Lingala, R. Marc Lebel, Krishna S. Nayak. Joint estimation of arterial input function and tracer kinetic parameters from under-sampled DCE-MRI, ISMRM 2017, p3751 (Oral Power Pitch Presentation)

2. **Yi Guo**, Sajan Goud Lingala, Krishna S. Nayak. Reconstruction of DCE tracer kinetic parameters from under-sampled data with a flexible model consistency constraint, ISMRM 2017, p2301 (Oral Presentation)

3. **Yi Guo**, Yinghua Zhu, Sajan Goud Lingala, R. Marc Lebel, and Krishna S. Nayak, Direct Reconstruction of Kinetic Parameter Maps in Accelerated Brain DCE-MRI using the Extended-Tofts Model, ISMRM 2016, p0868 (Oral presentation)

4. Sajan Goud Lingala, **Yi Guo**, Yinghua Zhu, Naren Nallapareddy, R. Marc Lebel, Meng Law, and Krishna Nayak. Accelerated brain DCE-MRI using Contrast Agent Kinetic Models as Temporal Constraints, ISMRM 2016, p0651 (Oral presentation)

5. **Yi Guo,** Yinghua Zhu, Sajan Goud Lingala, R. Marc Lebel, and Krishna S. Nayak, Direct Reconstruction of Tracer-Kinetic Parameter Maps from Prospective Highly Under-sampled DCE-MRI, ISMRM data sampling & image reconstruction workshop, 2016 (Oral presentation)

6. Sajan Goud Lingala, **Yi Guo**, Yinghua Zhu, Naren Nallapareddy, R. Marc Lebel, Meng Law, Krishna S. Nayak, Accelerated DCE MRI using contrast agent kinetic models as temporal constraints, ISMRM data sampling & image reconstruction workshop, 2016 (Oral presentation)

7. S.G.Lingala, Y.Mohsin, S.Bhave, X.Miao, **Y.Guo**, K.S.Nayak, E.DiBella, M.Jacob, Data-adaptive reconstruction algorithms for accelerated dynamic MRI: an open-source MATLAB package, ISMRM reconstruction workshop, 2016.

8. KS Nayak, **Y Guo**, Y Zhu, SG Lingala, RM Lebel, N Nallapareddy, MS Shiroishi, M Law. "Improved clinical DCE-MRI pipeline for high resolution, whole brain imaging: application to brain tumor patients." RSNA 2015, Chicago, Oral Presentation: #SSA18-04. (Oral presentation)

9. **Yi Guo**, Yinghua Zhu, Sajan Goud Lingala, R. Marc Lebel, and Krishna S. Nayak, Highly Accelerated Brain DCE MRI with Direct Estimation of Pharmacokinetic Parameter Maps, ISMRM 2015, p0573 (Oral presentation)

10. **Yi Guo**, R. Marc Lebel, Yinghua Zhu, Mark S. Shiroishi, Meng Law, and Krishna S. Nayak, High-resolution Whole-brain DCE MRI of Brain Tumor using Constrained Reconstruction: Prospective Clinical Evaluation, ISMRM 2015, p3050

11. Xin Miao, Sajan Goud Lingala, **Yi Guo**, Terrence Jao, and Krishna S. Nayak, Accelerated Cardiac Cine Using Locally Low Rank and Total Variation Constraints, ISMRM 2015, p0571 (Oral presentation)

12. Yinghua Zhu, **Yi Guo**, Sajan Goud Lingala, R. Marc Lebel, Meng Law, Krishna Nayak, Evaluation of GLACIER sampling for 3D DCE-MRI, ISMRM 2015, p2535

13. Yinghua Zhu, **Yi Guo**, Sajan Goud Lingala, Samuel Barnes, R. Marc Lebel, Meng Law, Krishna Nayak, Evaluation of DCE-MRI Data Sampling, Reconstruction and Model Fitting Using Digital Brain Phantom, ISMRM 2015, p3052

14. Sajan Lingala, **Yi Guo**, Yinghua Zhu, Samuel Barnes, Robert Marc Lebel, Krishna Nayak, Accelerated DCE MRI Using Constrained Reconstruction Based on Pharmaco-Kinetic model dictionaries, ISMRM 2015, p0196

15. Weiyi Chen, **Yi Guo**, Ziyue Wu, Krishna S. Nayak, MRI Constrained Reconstruction without Tuning Parameters Using ADMM and Morozov's Discrepency Principle, ISMRM 2015, p3410

16. R. Marc Lebel, **Yi Guo,** Yinghua Zhu, Sajan Goud Lingala, Richard Frayne, Linda B Andersen, Jacob Easaw, Krishna S Nayak, The comprehensive contrast-enhanced neuro exam, ISMRM 2015, p3705

17. Yinghua Zhu, **Yi Guo**, R. Marc Lebel, Meng Law, Krishna S Nayak, Randomized Golden Ratio Sampling For Highly Accelerated Dynamic Imaging, ISMRM 2014, p4365

18. **Yi Guo**, Xiaoke Wang, Sheng Fang, Kui Ying, Hua Guo, Shi Wang, Enhanced motion correction combining PROPELLER and Parallel Imaging, ISMRM 2012, p4862

Patents

1. Krishna S. Nayak, **Yi Guo**, R. Marc Lebel, Sajan Goud Lingala, Yinghua Zhu, "Method for Improved Dynamic Contrast Enhanced Imaging Using Tracer-Kinetic Models as Constraints", United States Patent Application number: 62/336/033, filed May 2016.

2. Yinghua Zhu, **Yi Guo**, Krishna S. Nayak, Robert Marc Lebel, "DYNAMIC 3D MRI DATA SAMPLING" United States Patent Application 15/075,716, filed March, 2016

Abbreviation

ADMM	Alternating Direction Methods of Multipliers
AIF	Arterial Input Function
B_1	Radiofrequency magnetic field strength
B_1^+	Transmit radiofrequency magnetic field
BBB	Blood Brain Barrier
CT	Computed Tomography
DCE	Dynamic Contrast-Enhanced
DICOM	Digital Imaging and Communications in Medicine
eTofts	Extended-Tofts modelling
FSPGR	Fast spoiled gradient echo sequence
K_{ep}	Rate constant from interstitium to plasma
K^{trans}	Volume transfer constant from plasma to interstitium
l-BFGS	Limited memory Broyden–Fletcher–Goldfarb–Shannon algorithm
MRI	Magnetic Resonance Imaging
mSSIM	Mean Structural Similarity Index
NLCG	Nonlinear conjugate gradient algorithm
PACS	A picture archiving and communication system
Patlak	Linearized PK modelling
PET	Positron Emission Tomography
TK	Tracer-Kinetic
R_1	$1/T_1$, Longitudinal relaxation rate
r_1	Contrast agent relaxivity
rMSE	Root Mean Squared Error
ROI	Region of Interest
SPECT	Single-photon emission computed tomography
T_1	Longitudinal relaxation time constant
v_e	Volume fraction of extravascular extracellular space
v_p	Volume fraction of blood plasma

Abstract

Dynamic Contrast Enhanced Magnetic Resonance Imaging (DCE-MRI) is a non-invasive technique that provides information about the delivery of blood and agents within the blood to bodily organs. In oncology imaging, DCE-MRI is used to generate tracer kinetic (TK) parameter maps to evaluate tumor severity, differentiate malignant from benign, and to evaluate response to therapy. Current DCE-MRI methods have poor reproducibility, low spatial resolution, and limited spatial coverage.

The overall goal of my dissertation is to improve brain DCE-MRI by using constrained reconstruction and model-based reconstruction from under-sampled raw data (sampled below the Nyquist rate). Such techniques can provide substantially higher spatio-temporal resolution, better coverage, and improved image quality with the same scan time and contrast agent dose. Using model-based reconstruction, TK parameter maps, the end-point product of DCE-MRI, can be directly estimated from under-sampled data with improved quality and reproducibility.

I evaluated a specially tailored constrained reconstruction technique for DCE-MRI in brain tumor patients. The proposed technique is able to provide high spatial resolution and whole-brain coverage via under-sampling and constrained reconstruction with multiple sparsity constraints. Conventional fully-sampled DCE-MRI and the proposed whole-brain DCE-MRI were performed on the same brain tumor patients for evaluation. The proposed method is able to provide whole-brain high-resolution DCE-MRI with improved image quality compared to conventional DCE-MRI, using only 1/30th of the raw data. These advantages may allow comprehensive permeability mapping in the brain, which is especially valuable in the setting of large lesions or multiple lesions spread throughout the brain.

I also developed a model-based direct reconstruction technique for DCE-MRI, where the TK parameter maps can be directly estimated from raw-data. By comparison with a state-of-the-art indirect constrained reconstruction technique, the proposed direct approach provides improved TK map fidelity, and enables much higher acceleration up to 100×. With the prospective study, this method is shown to be clinically feasible and provide high-quality whole-brain TK maps.

To address the limitation of the direct reconstruction, I proposed a model consistency constrained reconstruction for DCE-MRI. The proposed reconstruction poses the tracer-kinetic (TK) model as a model consistency constraint, enabling the inclusion of different TK solvers and the joint estimation of the arterial input function (AIF) from highly under-

sampled data. Good quality TK maps and patient specific AIF can be reconstructed at high under-sampling rates up to 100×.

Chapter 1. Introduction

1.1   Motivation

Cancer is the second leading cause of death in the United States, accounting for approximately 600,000 deaths in 2013 (1). Brain cancer refers to cancerous tumors that form inside human brain tissue. Cancerous tumors can be divided into primary tumors that start within the brain, and secondary tumors that have spread from somewhere else, also known as brain metastases. Brain cancer has a high mortality rate, depending on tumor type, tumor size, and how early the tumor is detected. The mortality rate of brain tumor can be greatly reduced if small lesions can be detected and treated early.

A variety of examinations are available for brain tumor evaluation and diagnosis, among which Magnetic Resonance Imaging (MRI) and Computed Tomography (CT) are the most commonly used (2). In clinical practice, multiple modalities are used jointly to accurately diagnose the tumor. Reproduced from (3), Figure 1.1 shows representative CT and MRI images.
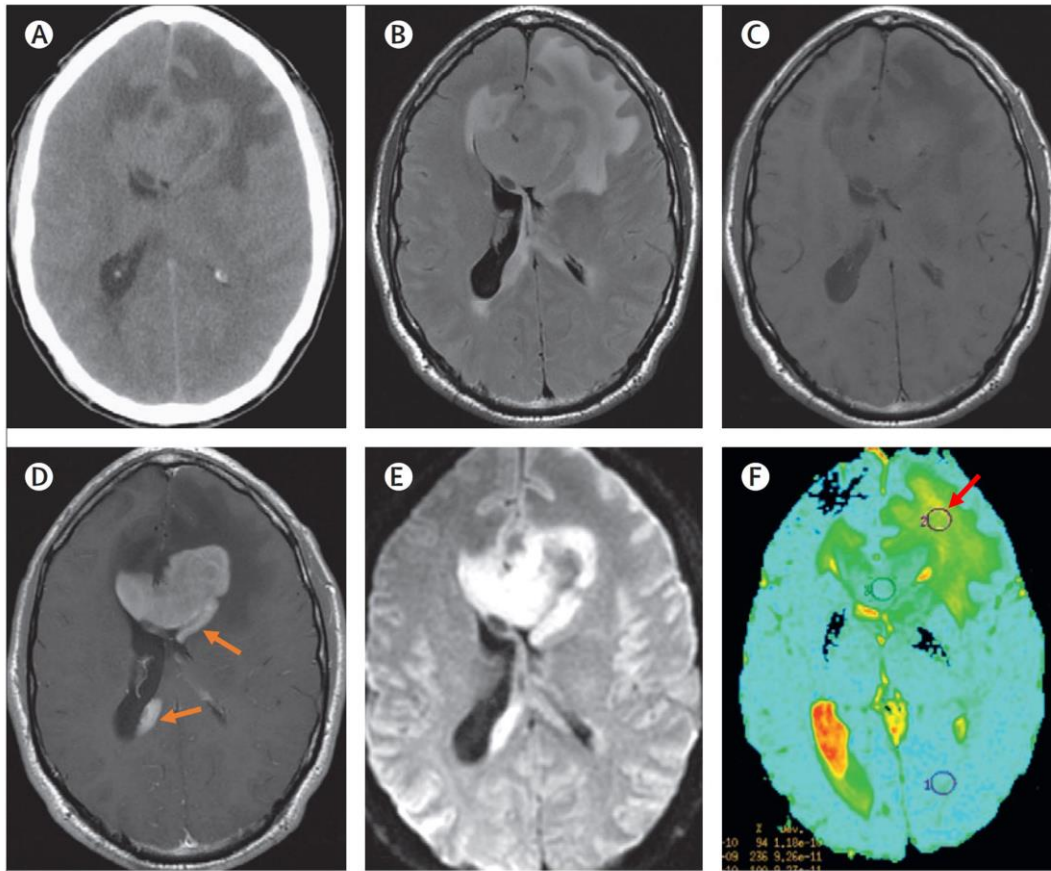
Figure 1.1 Multimodality medical imaging scan of the brain of a middle-aged man with a primary central neural system lymphoma (A) A CT scan shows a spontaneous mild hyperdense lesion. (B) A fluid attenuated inversion recovery (FLAIR)-weighted MRI of a peripheral oedema. (C and D) A T1-weighted spin-echo MRI without (C) and with (D) contrast with homogeneous enhancing of two lesions in contact with the ventricles. Contrast-enhanced T1w MRI provide high detectability of the tumor (see arrows) (E) A diffusion-weighted MRI with a high signal of the lesion. (F) An apparent diffusion coefficient map of a diffusion-weighted MRI that shows a restriction of intratumoral diffusion (see arrow), which is suggestive of a high cellular tumor. Reproduced from figure 7 in Ricard, D., Idbaih, A., Ducray, F., Lahutte, M., Hoang-Xuan, K., & Delattre, J. Y. (2012). Primary brain tumours in adults. The Lancet, 379(9830), 1984–1996.

MRI is a non-invasive imaging tool that provides excellent soft-tissue contrast, arbitrary reformatting, and 3D imaging. Comparing to CT or PET that expose patients to radiation, MRI is safe and noninvasive, making it ideal to longitudinally monitor tumor progression and treatment effectiveness.

As shown in Figure 1.1, MRI provides multiple different contrasts. For brain tumor evaluation, efforts have been made to standardize the imaging protocol in clinical trials, and in (4), the consensus recommends the following key elements for a brain tumor

imaging protocol: (i) a pre-contrast, 3-dimensional, isotropic, inversion-recovery T_1-weighted gradient echo (IR-GRE) sequence; (ii) an axial, 2-dimensional T_2-weighted fluid-attenuated inversion recovery (FLAIR) sequence obtained using a turbo-spin-echo (TSE) readout; (iii) an axial, 2-dimensional, 3-directional (isotropic) diffusion-weighted imaging (DWI) sequence obtained using echo-planar (EPI) or radial acquisition; (iv) an axial, 2-dimensional T_2-weighted TSE sequence; and (v) a post-contrast, 3-dimensional, isotropic, T1-weighted IR-GRE sequence with matching acquisition parameters to pre-contrast T1-weighted images.

The key element for a brain tumor imaging protocol is the pre- and post-contrast T1-weighted images obtained from a contrast injection. Apart from the aforementioned sequences for clinical standardization, emerging MRI techniques like dynamic contrast-enhanced (DCE) or dynamic susceptibility contrast (DSC) perfusion MRI have been proposed to track the contrast agent dynamics during the contrast administration. Comparing to static T_1- or T_2-weighted anatomic images, these dynamic imaging techniques can be used for quantitative assessment of specific pathophysiologic parameters, more accurate grading of intracranial tumors, and differentiation of tumors from normal tissue (5).

1.2 Dynamic Contrast Enhanced Magnetic Resonance Imaging (DCE-MRI)

Current brain tumor evaluation criteria, Response Assessment in Neuro-Oncology Criteria (RANO) (6, 7), can only consider lesions that are larger than 1cm in maximal diameter. This is due to the poor resolution of conventional MRI techniques. DCE-MRI is not part of the RANO criteria yet, but it is increasingly of interest. It can provide important information about neurovascular system, so it may be a powerful tool for evaluating effectiveness of therapies.

DCE-MRI is a noninvasive imaging tool that tracks the delivery of blood to plasma, capillary, and bodily organs by injecting an exogenous contrast agent. In T_1 weighted DCE-MRI, a Gadolinium-based contrast agent will shorten the T_1 value, a key parameter in MRI imaging that will result in change of signal intensity. Thus the delivery of blood can be traced by the brightened signal intensity, and lesions and abnormal regions can be labeled. As shown in Figure 1.2, the blood–brain barrier (BBB) separates the parenchyma of the central nervous system from the blood. By tracking the contrast agent dynamics from blood to abnormal tissues through BBB break down, DCE-MRI is able to assess many brain pathologies that cause an opening of the BBB, such as tumors, multiple sclerosis and acute ischemic strokes. While these diseases show relatively large abnormalities in BBB functionality, there is also growing interest in the application of DCE-MRI to pathologies

associated with more subtle and chronic BBB disruption, such as cerebral small vessel disease, diabetes and Alzheimer's disease (8).
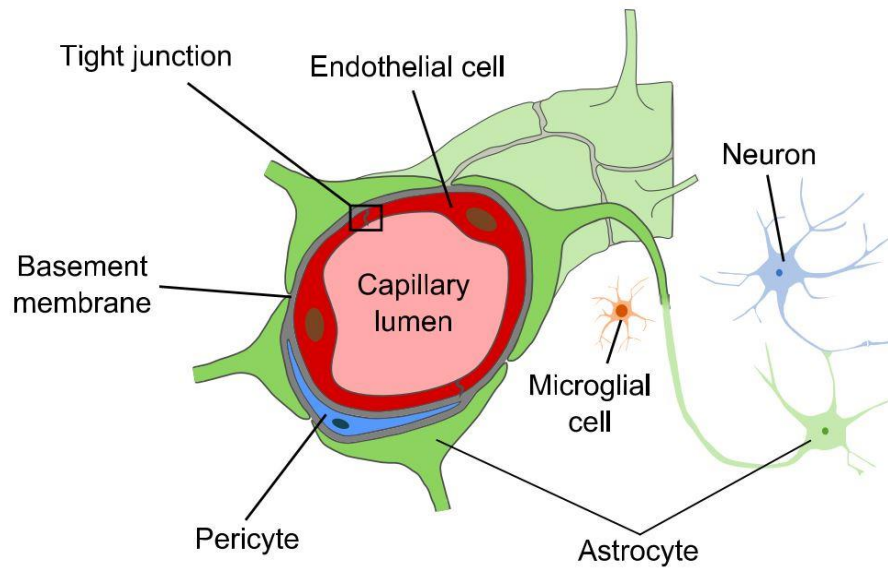

Figure 1.2 Schematic drawing of the neurovascular unit. The BBB is formed by endothelial cells that line brain capillaries and are sealed by tight junctions. Astrocytes, pericytes, microglial cells and basement membranes interact with the endothelium of the BBB, providing functional and structural support. Reproduced from A. K. Heye, et al., "Assessment of blood–brain barrier disruption using dynamic contrast-enhanced MRI. A systematic review," NeuroImage: Clinical, vol. 6, pp. 262–274, 2014.

From the dynamic signal changes in DCE-MRI, tracker-kinetic (TK, or termed pharmacokinetic in previous literatures) parameter maps (K^{trans}, K_{ep} and v_p etc.) can be derived. K^{trans} is an important TK parameter that indicates BBB permeability surface and blood flow. It can be used for direct evaluation of the tumor severity. These enable DCE-MRI to be a powerful tool to characterize tumor biology and treatment response (9–11).

However, DCE-MRI currently is not the standard of care in many centers conducting clinical trials in oncology (12). This is because 1) low resolution and limited coverage of the dynamic scans cannot provide adequate information for the whole-brain; 2) accuracy and reproducibility of quantitative DCE-MRI kinetic modelling is difficult to trust and evaluate due to different TK modelling strategies and reconstruction techniques. The clinical translation of DCE-MRI is considered a major challenge. Improvement of resolution, coverage, and modeling reproducibility can greatly help clinical translation of DCE-MRI, and is the main focus of my research.

1.3 Organization of the Dissertation

- Chapter 2 provides background and review of related technology that is helpful to understand later chapters. It gives high-level description of MRI physics, sampling schemes and reconstruction techniques that are related to the author's work. It also provides detailed description of a DCE-MRI pipeline including sequence, sampling, pre-processing, correction, reconstruction and kinetic modeling.

- Chapter 3 describes a prospective evaluation of brain DCE-MRI with constrained reconstruction. A novel constrained reconstruction with multiple constraints specifically tailored to DCE was applied to brain tumor patients to achieve a whole-brain high-resolution DCE-MRI. Double injection on the same patients allowed us to compare directly to the current best practices. In fifteen brain tumor patients that were scanned, this new approach has shown the potential to vastly improve visualization and characterization of brain lesions with DCE-MRI.

- Chapter 4 describes a novel and efficient reconstruction scheme to directly estimate tracer-kinetic parameter maps from highly undersampled DCE-MRI data. By comparison with a state-of-the-art indirect compressed sensing method, it demonstrates that the proposed direct approach provides improved TK map fidelity, and enables much higher acceleration. With the prospective study, this method is shown to be clinically feasible and provide high-quality whole-brain TK maps.

- Chapter 5 describes a joint AIF and TK estimation framework using a model-consistency constraint. By posing the TK model as a model consistency constraint instead of directly forcing the model. The framework can allow for model deviation and provide better quality TK maps. It decouples the direct reconstruction problem into two well-defined sub-problems, thus greatly reducing the complexity of the algorithm. This formulation also has the benefit of easy inclusion of different TK solver, and joint estimation of AIF from under-sampled data.

Chapter 2. Background

2.1   MRI Physics

This section will introduce basic MRI physics on MR signal generation, T_1 and T_2 relaxation, and concept of k-space and (k,t)-space. It will also introduce Parallel imaging, one of the acceleration techniques that is routinely used in MRI scanner now.

2.1.1   MR Signal Generation

Because of its presence in water and fat in human body, MRI typically utilizes hydrogen protons for imaging. The hydrogen proton naturally has a magnetic moment, or spin, with its positive charge and angular momentum. Naturally the spins have random directions, and will not have any net magnetization in macroscopic scale as shown in Figure 2.1 (a). In a MRI system, a strong constant magnetic field (3 Tesla for the commonly used commercial machines) is present in the bore of the machine. With this external magnetic force (denoted as B_0), the hydrogen spins will accumulate a net magnetization in the direction (M_z) of the external magnetic force, as shown in Figure 2.1 (b). The angular frequency of nuclear precession will be:

$$\omega_0 = \gamma B_0 \qquad\qquad (2.1)$$

This is also known as Larmor frequency. γ is a constant that is nucleus-dependent (42.58 MHz/T for Hydrogen).

If a transverse oscillating magnetic field (denoted as B_1) is introduced with the same frequency as Larmor frequency, it will tip down the magnetization by the angle determined by the strength and duration of B_1, as shown in Figure 2.1 (c) and (d). This angle is called flip angle (FA), this frequency is called resonance frequency, and this oscillating magnetic field is called RF (radio-frequency) pulse, since B_1 oscillates in the radio-frequency range. After RF excitation, the magnetization rotates in xy-plane. The vector component of the magnetization in this plane is called transverse magnetization (denoted as M_{xy}). This rotating transverse magnetization will then give rise to a signal in the receiver coil.
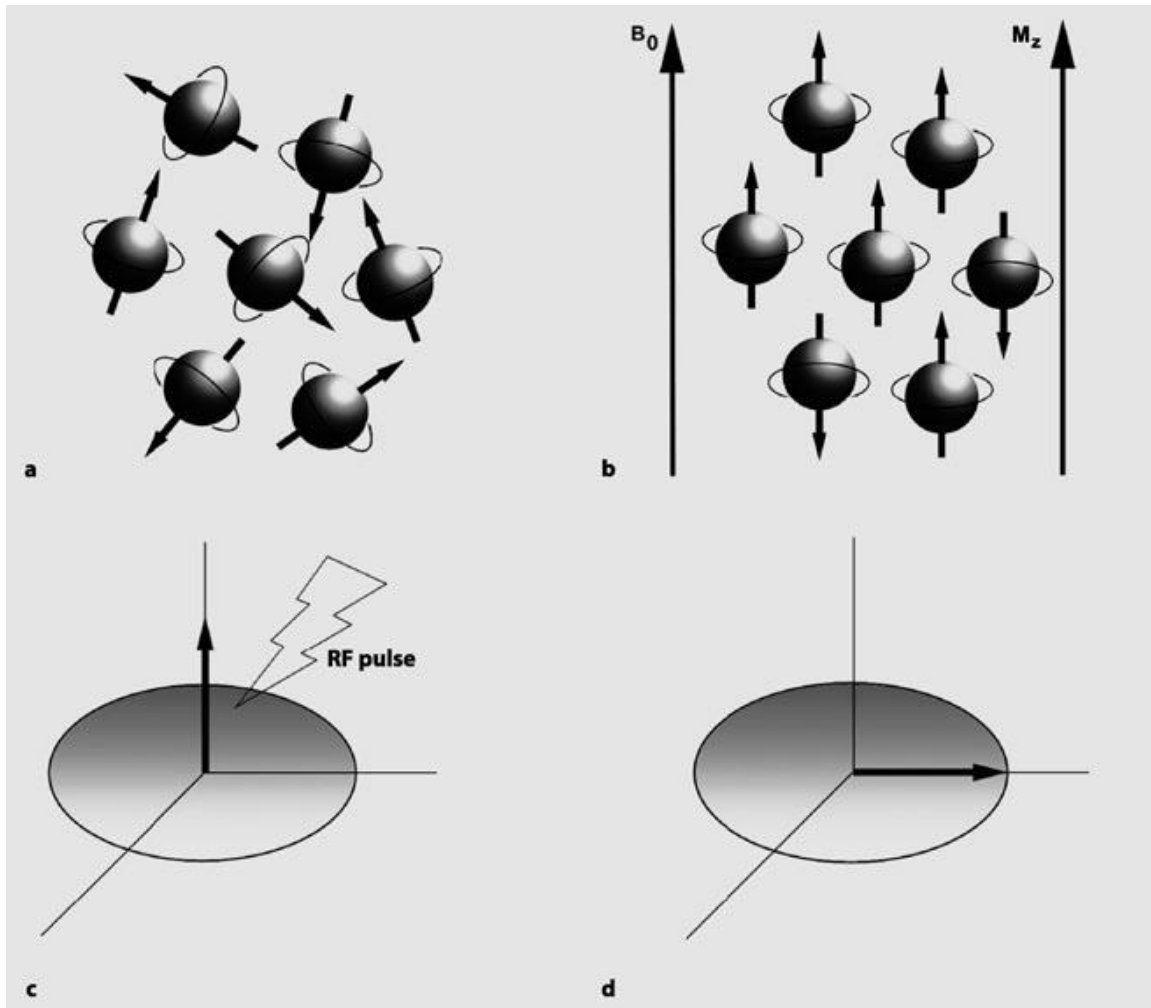
Figure 2.1. With no external magnetic field present, spins rotate about their axes in random direction (a). In the presence of a magnetic field, slightly more spins align parallel to the main magnetic field, B_0, and thus produce longitudinal magnetization, M_z (b). An RF pulse (c) tips the magnetization vector by exactly 90°, causing the entire longitudinal magnetization to flip over and rotate into transverse magnetization, M_{xy} (d). Reproduced from (13).

2.1.2 T$_1$ and T$_2$ Relaxation

The MR signal will rapidly fades and return to stable state due to spin-lattice interaction and spin-spin interaction. The spin-lattice interaction is called T_1 relaxation, and spin-spin interaction is called T_2 relaxation.
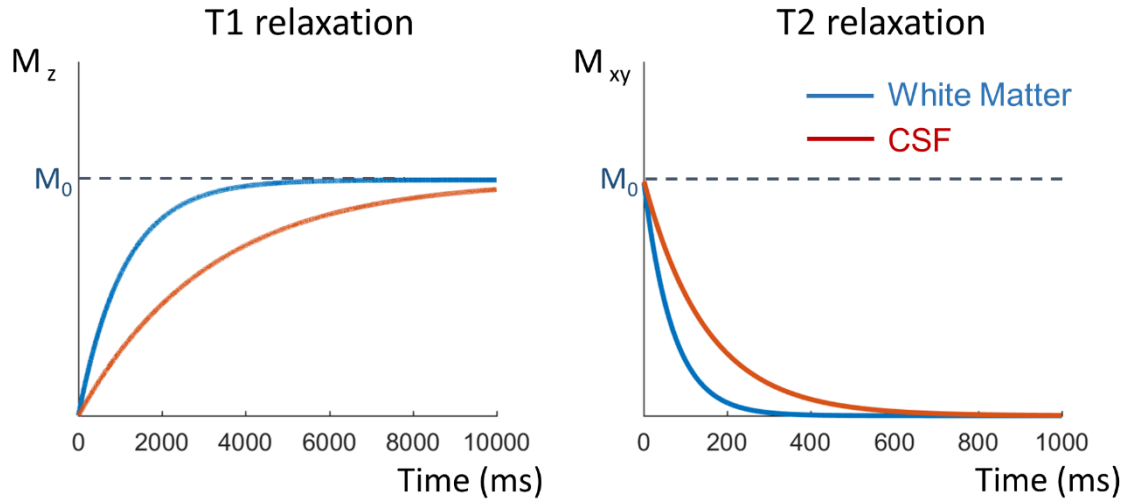
Figure 2.2 T_1 and T_2 relaxation over time for different tissue type. T_1 relaxation will restore the longitudinal magnetization (a), and T_2 relaxation will decrease the transverse magnetization (b).

T_1 relaxation will cause the magnetization to return to stable state, or equilibrium in M_z direction, as shown in Figure 2.2 (a). T_2 relaxation will decrease the transverse magnetization, and eventually destroy the MR signal, as shown in Figure 2.2 (b). Different tissue types will have different T_1 and T_2 relaxation rate, and utilization this property can create MR images of different contrast between tissues. T_1 value of a specific tissue is defined as the time required to restore 63% of the original longitudinal magnetization (M_0), and T_2 value is defined as the time required to lose 63% of the transverse magnetization (M_{xy}). Typical T_1 and T_2 values of different tissues at 3T in literatures (14–16) are listed in Table 2.1.

Table 2.1 Typical T_1 and T_2 values of different tissues at 3T.

Tissue	T_1 value at 3T (ms)	T_2 value at 3T (ms)
White Matter	1110 ± 45	69 ± 3
Gray Matter	1470 ± 50	99 ± 7
Blood	1550	275 ± 50
Skeletal Muscle	1420 ± 38	50 ± 4
Cerebral Spinal Fluid (CSF)	3120	150

If the contrast of a MRI image is weighted primarily by the signal difference caused by T_1 difference, it is called T_1-weighted imaging. Similarly, T_2-weightied imaging is for

contrast primarily caused by T_2 difference. Typical T_1 and T_2-weighted images of the brain is shown in Figure 2.3. In T_1-weighted images, tissues (e.g. CSF) with longer T_1 will be darker, since the signal is not recovered yet. In T_2-weighted images, tissues with longer T_2 will be brighter, since the signal is still preserved.
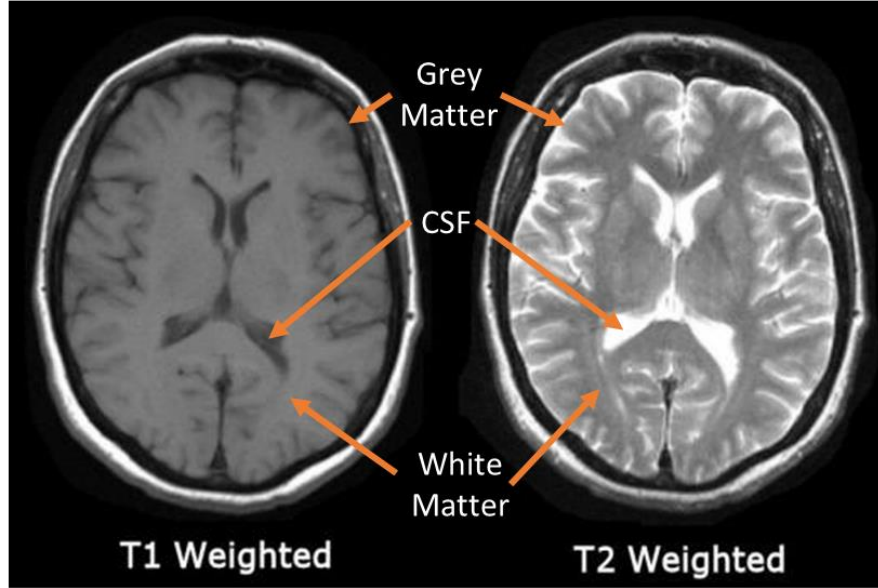
Figure 2.3 Typical T_1 and T_2 weighted images of the brain. In T_1-weighted image, gray matter and CSF are darker because of long T_1 values. In T_2 weighted image, gray matter and CSF are brighter because of long T_2 values, in contrast to T_1 weighted image.

2.1.3   MRI Signal Space

In additional to the constant magnetic field B_0 that is used to create net magnetization, and oscillating magnetic field B_1 that is to excite the signal, another gradient magnetic field that gradually (usually linearly) changes the magnetic field strength based on spatial location is applied to the magnetic core. As a result, the MR signal is coded with spatial information, as shown in the equation below (3D case):

$$S(k_x, k_y, k_z) = \iint I(x, y, z) e^{-i2\pi(k_x x + k_y y + k_z z)} \mathrm{d}x\mathrm{d}y\mathrm{d}z \qquad (2.2)$$

, where I is the 3d image being scanned with spatial coordinate x, y and z, k_x, k_y and k_z are determined by the gradient strength and localization, and $S(k_x, k_y, k_z)$ is the acquired MR signal. Depending on how the gradient is applied for localization, k_x direction is usually called frequency encoding direction, and k_y, k_z direction is called phase encoding direction. In this form, the signal is also in the Fourier transform domain of the image, therefore the MR signal space is called k-space. Normally we use Nyquist rate to sample the k-space at

Cartesian grid, and 3D inverse Fourier transform will reconstruct the images from *k*-space, as shown in Figure 2.4 for one slice in 3D. In the context of dynamic imaging, where a whole (or partial) *k*-space is acquired at some time interval, the *k*-space plus time dimension is also called (*k, t*)-space.
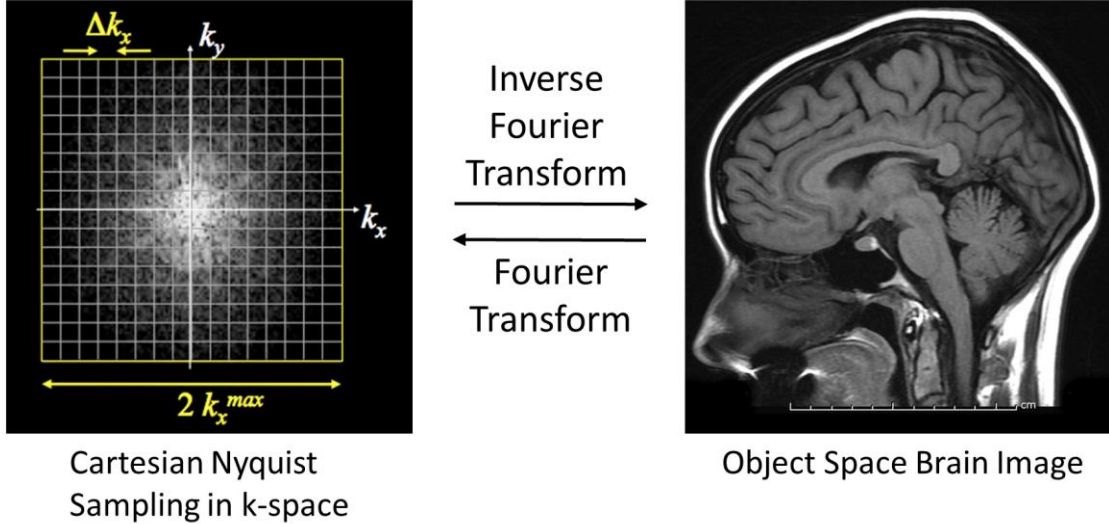
Figure 2.4 Relationship between image and Cartesian Nyquist sampled *k*-space. In *k*-space, Δk_x will determine the field-of-view (FOV) of the image, and k_x^{max} will determine the resolution of the image. Reproduced using images from Karla Miller, FMRIB, University of Oxford.

2.1.4 Parallel Imaging

MRI is intrinsically slow using Cartesian Nyquist sampling, where we need to acquire every point in *k*-space to avoid aliasing in the images. However, if we can utilize multiple coils that are receiving the same signal with different coil sensitivity (weighting of the signal), we are able to restore images by acquiring only part of the *k*-space. This technique is called parallel imaging.

As shown in Figure 2.5, if multiple coils are used to acquire only half of the *k*-space by sample every other line of *k*-space, the resulting individual coil images will be wrapped around. However, by utilizing the different coil weighting (coil sensitivity), the original image can be reconstructed from these multiple coil images. This image space technique is called SENSE (Sensitivity encoding) (17). It targets to solve the image *x* from under-sampled *k*-space *y* using the following equation:

$$x = (E^H \Psi^{-1} E)^{-1} E^H \Psi^{-1} F^{-1} y \tag{2.3}$$

, where E is the coil sensitivity encoding maps, F is Fourier transform, and Ψ is the noise covariance matrix.

Besides SENSE, other variants of parallel imaging exist. The coil sensitivity information can be implicitly used in k-space directly to reconstruct fully-sampled k-space from under-sampled k-space, and such techniques include GRAPPA (18), SPIRiT (19), ESPIRiT (20), LORAKS (21) , etc.

Parallel data aquisition
- Reduction of phase-encoding steps (factor of 1.0-4.0)
- Receiver coil array (at least 2 coil elements)

Individual images
- Reduced field of view in phase-encoding direction
- Different signal weighting resulting from differences in coil sensitivity

Reconstructed image
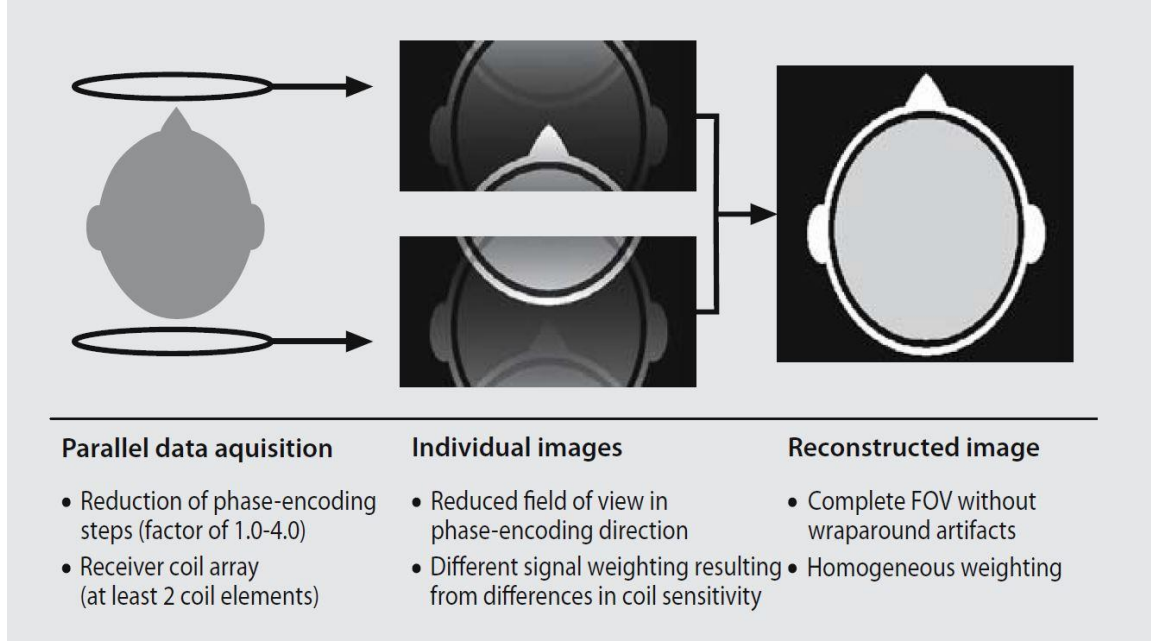- Complete FOV without wraparound artifacts
- Homogeneous weighting

Figure 2.5 In parallel imaging, an array of receiver coils simultaneously collects the MR signals. Scan time is shortened by reducing the number of phase-encoding steps. As a result, the individual images are obtained with a smaller FOV and show the typical wraparound artifacts. A complete image without wraparound artifacts is reconstructed by combining the individual images. Reproduced from Weishaupt D, Köchli VD, Marincek B: How Does MRI Work? 2008.

2.2   DCE-MRI Basics

This thesis focuses on dynamic contrast enhanced MRI (DCE-MRI). DCE-MRI is one of the dynamic MRI techniques that employs continuous T_1-weighted imaging before, during and after a bolus injection of a gadolinium-based contrast agent (GBCA). With the help of additional mapping sequences before DCE-MRI scan, changes in GBCA concentration is derived from changes in signal intensity, then regressed to quantify tracer kinetic (TK) parameters such as K^{trans} (volume transfer constant), v_p (fractional plasma volume), and v_e (fractional extravascular extracellular space volume) (9, 22) . Figure 2.6 from (8) illustrated typical T_1 weighted DCE-MRI images, the signal enhancement of tumor tissue due to contrast injection, and the derived K^{trans} maps.
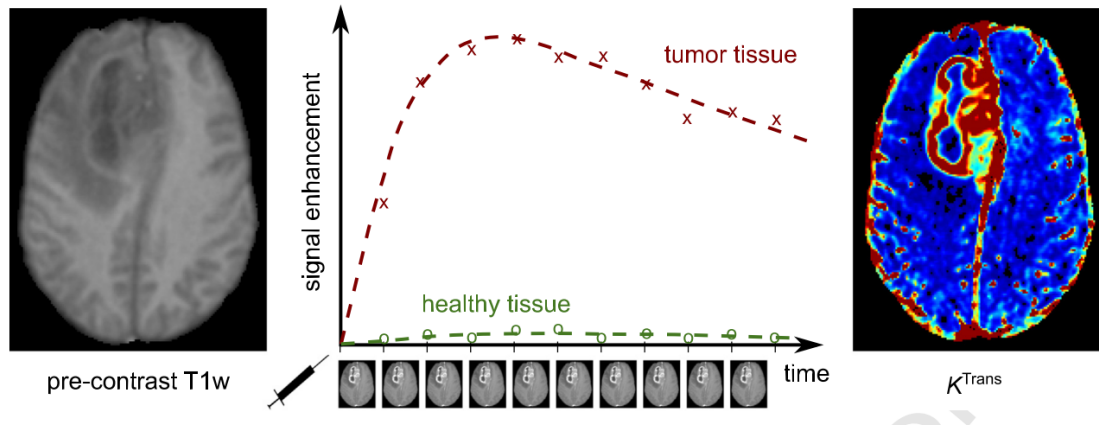
Figure 2.6 Illustration of DCE-MRI. The repeated acquisition of T1-weighted images after contrast agent injection allows the calculation of signal enhancement as a function of time (middle) when compared to the pre-contrast signal intensity (left). These curves can be used to calculate maps of quantitative pharmacokinetic parameters (e.g. K^{trans}, right). Reproduced from A. K. Heye, et al., "Assessment of blood–brain barrier disruption using dynamic contrast-enhanced MRI. A systematic review," NeuroImage: Clinical, vol. 6, pp. 262–274, 2014.

DCE-MRI is used for quantitative assessment of brain tumors (23, 24), multiple sclerosis lesions (25), and Alzheimer's disease (26) and other neurological disorders that involve blood-brain barrier (BBB) disruption. This section will introduce each step of a complete DCE-MRI procedure.

2.2.1 Calibration Scans

B1+ Mapping

B1+ represents the inhomogeneity in the transmitted RF filed, which will affect the actual flip angle applied to the MRI bore. Flip angle will in turn affect the conversion of DCE-MRI signal intensity to contrast concentration curves, and impact the final TK parameter value accuracy. Figure 2.7 shows typical B1+ maps in head phantom and human brain. It shows that the actual flip angle inside the MRI bore is often different from what we prescribe on the scanner console. Ignoring this variation will lead to inaccurate TK mapping results. (12)
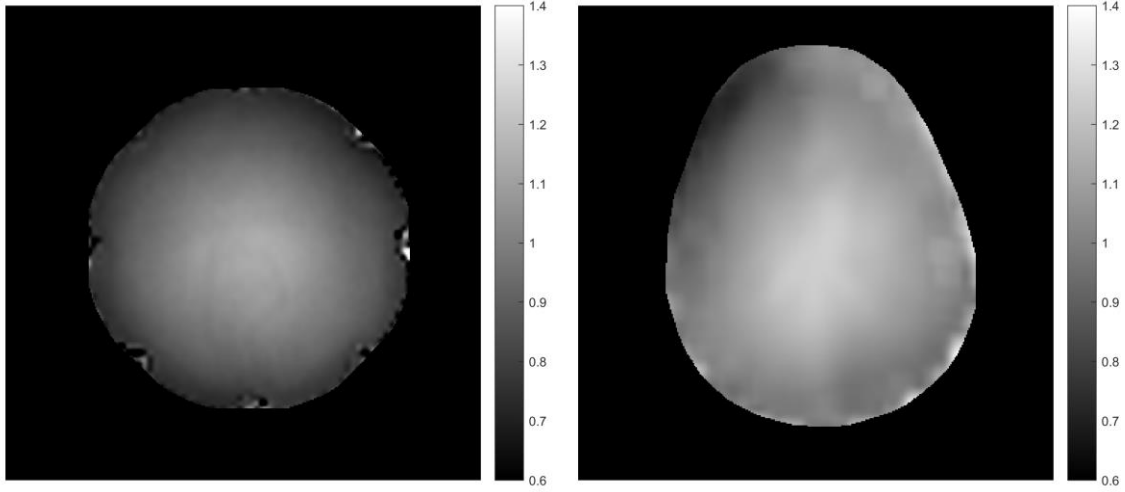
Figure 2.7 Illustration of a typical B1+ maps of a head phantom (left) and human brain (right) in normalized unit, where 1 means the actual flip angle is equal to the prescribed flip angle. The inhomogeneity of the B1+ maps can be clearly seen.

The clinically available 3D double-angle gradient-echo method (DAM) (27) is usually performed to measure B1+ maps. This method acquires two gradient-echo images (I_1 and I_2) with prescribed flip angles of α and 2α. The actual flip angle (hence the B1+ maps) can be calculated as:

$$\alpha = \arccos\left(\left|\frac{I_2}{2I_1}\right|\right)$$

(2.4)

Apart from DAM, a faster and more efficient approach called Bloch-Siegert shift (28) was also proposed recently. This is also the standard B1+ mapping protocol on GE MRI scanners.

T₁ Mapping

Pre-contrast T_1 and M_0 values are also important parameters that affect the accuracy in conversion of signal to contrast concentration curves. Figure 2.8 shows a typical M_0 and T_1 maps of human brain. Mapping the variation of M_0 and T_1 maps is important for accurate TK parameter mapping.
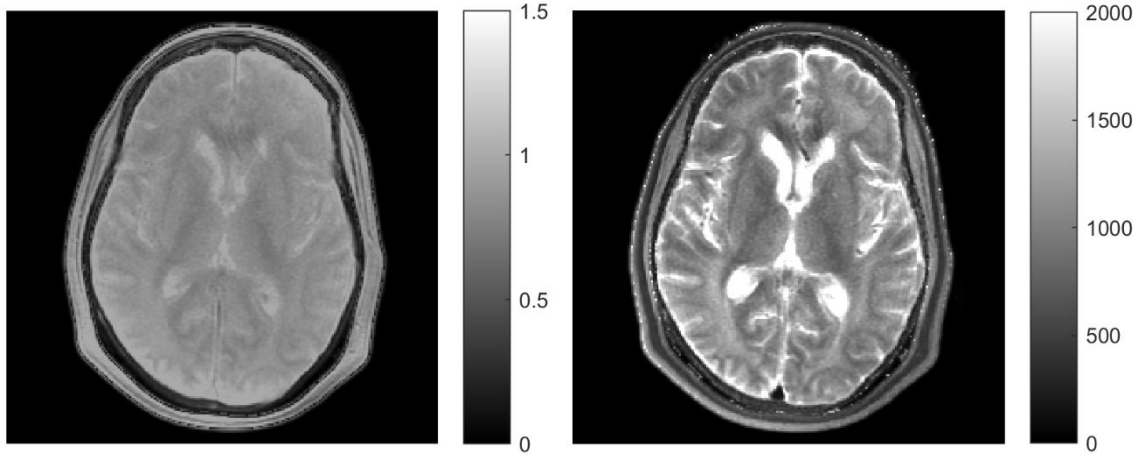
Figure 2.8 Typical M_0 (left) and T_1 (right) maps of human brain. M_0 map is in normalized unit, and T_1 map unit is millisecond. T_1 values are greatly different for different type of tissues in the brain.

Various T_1 mapping techniques exist in MRI, and in DCE-MRI, DESPOT1(29) method is commonly used for the speed and efficiency. DESPOT1 method acquires multiple spoiled gradient echo (SPGR) images (S) with different flip angles (α), and fits the T_1 and M_0 maps using following signal equation:

$$S(\alpha) = \frac{M_0 \sin\alpha(1 - e^{-TR/T_1})}{1 - \cos\alpha e^{-TR/T_1}} \qquad (2.5)$$

, where TR is the repetition time in MRI. The fitting is performed by converting the problem to a linear matrix inversion problem to solve for $e^{-TR/T1}$ using the acquired multiple images $S(\alpha)$, then T_1 can be computed easily from $e^{-TR/T1}$. Figure 2.9 shows SPGR signal intensity versus flip angle at different T_1 value. Small flip angles of 2°, 5°, 10° are often used for T_1 mapping utilizing the linear region of the fitting equation.
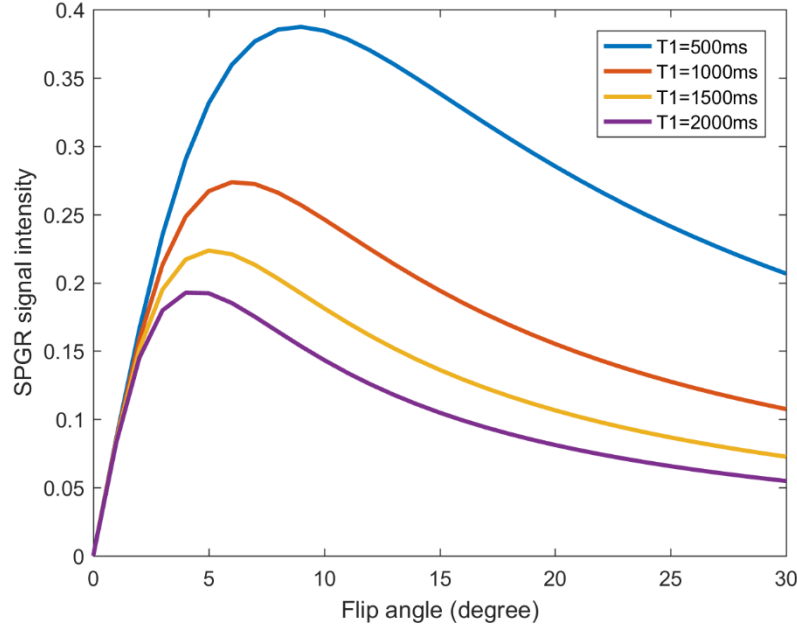
Figure 2.9 SPGR signal intensity versus different flip angle at different T_1 value. Based on these curves, small flip angles of 2°, 5°, 10° are close to linear region, and are used for the fitting the T1 values.

2.2.2   DCE-MRI Scan

Dynamic contrast enhanced MRI uses a fast spoiled gradient echo sequence (SPGR) to acquire a series of images during the administration of a Gadolinium-based contrast agent. Taking account of the intensity of the signal and the contrast between different tissues, a flip angle of 10° to 30° is appropriate to get images with good SNR and tissue contrast. In practice, a flip angle of 15° is usually used for DCE-MRI.

Conventionally, data is sampled at Nyquist rate on the Cartesian grid for proper restoration of the MRI images. SPGR signal intensity follows the same Equation (2.5), and for dynamic images (S), the signal equation is:

$$S(t) = \frac{M_0 \sin\alpha(1 - e^{-TR \cdot R(t)})}{1 - \cos\alpha e^{-TR \cdot R(t)}} \tag{2.6}$$

where R(t) is R_1 (reciprocal of T_1) over time. This equation assumes steasdy state for the spoiled gradient echo sequence, and not applicable to inflow enhancement. The time dimension t is neglected in the following text for simplicity.

2.2.3 Pre-processing for TK modelling

Tracer-kinetic (TK) modelling in DCE-MRI mainly involves fitting the TK parameters using the contrast concentration in tissue (C) and the contrast concentration in artery (also called artery input function, or AIF). This section describes the method to estimate these two variables from the acquired data.

Signal to Concentration Conversion

MRI samples in k-space, which is Fourier transform space of the images. Basic MRI reconstruction involves data correction, inverse Fourier transform, and coil combination (if multiple coils are used). If multiple coils are used and some under-sampling are involved, we often solve the target images (S) by the following least-square problem:

$$S = \arg\min_{S} \| UFE(S) - y \|_2^2 \tag{2.7}$$

where U is the under-sampling matrix, F is the multi-dimensional Fourier transform, E is the coil sensitivity encoding, and y is the acquired k-space data.

This is one of the methods to solve SENSE (17, 30), a parallel imaging technique introduced in section 2.1.4. Iterative algorithms like Conjugate Gradient (CG) algorithm can be used to solve this least-square problem.

After we acquire the dynamic images (S), which is in 4d (3d spatial plus time) in our case, we can get the image differences by subtracting the pre-contrast first image (S_0):

$$\Delta S = S - S_0 \tag{2.8}$$

Then the contrast concentration (C) is converted from ΔS based on the SPGR signal equation (2.6) (31):

$$R = -\frac{1}{TR} \ln \frac{1 - \left(\dfrac{\Delta S}{M_0 \sin\alpha} + \dfrac{1-m}{1-m\cos\alpha} \right)}{1 - \cos\alpha \left(\dfrac{\Delta S}{M_0 \sin\alpha} + \dfrac{1-m}{1-m\cos\alpha} \right)}, m = e^{-TR \cdot R_0} \tag{2.9}$$

$$C = (R - R_0)/r_1$$

where R is the R_1 (reciprocal of T_1) values over time, TR is the repetition time, α is the flip angle, r_1 is the contrast agent relaxivity. R_0 and M_0 are the pre-contrast R_1 and the equilibrium longitudinal magnetization that are estimated from a T_1 mapping sequence as described in section 2.2.1.

AIF Extraction

Before the TK modelling, we need to extract the arterial input function (AIF), which is an essential parameter in the modelling part. AIF is the concentration curve in an artery, which can be determined manually by a radiologist. This ROI can also be determined automatically by clustering or model-based techniques (32, 33). This is called patient-specific AIF, or pat-AIF. Temporal resolution is critical in obtaining a high-quality AIF, and a temporal resolution of one second is preferred, which is difficult to achieve using conventional MRI techniques (34, 35).

In the literature, a fixed population-averaged AIF (pop-AIF) was also proposed (36). Pop-AIF is used when the pap-AIF is difficult to obtain from the data. It is robust to noise and inter-patient variability, but may lead to inaccurate TK values since patient-specific information is not taken account for. Pop-AIF takes a parameterized function form (11 parameters in Parker's pop-AIF model), with a few parameters adjusted by the actual patient data. Other parameterized AIF was also proposed, with the delay and dispersion parameter to be adjusted by the actual data (37). Figure 2.10 shows a default pop-AIF as proposed in (36), and two deformed shapes by adjusting the parameters.
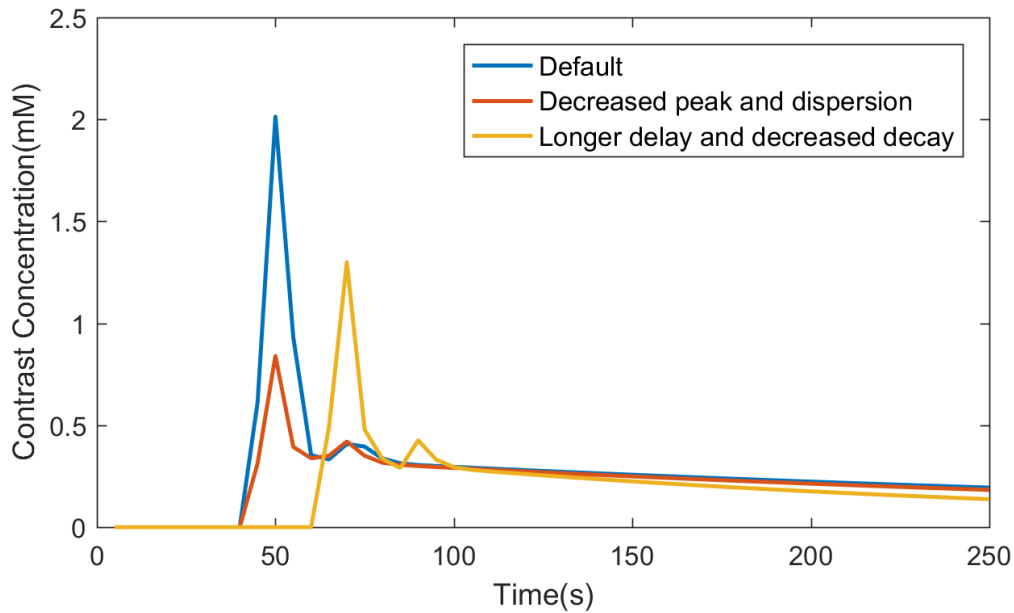

Figure 2.10 Shapes of population-averaged AIF using different parameters. "Default" uses the parameters provided in the literature.

Figure 2.11 illustrates how to extract pat-AIF from a ROI in patient-data, and the resulting TK parameter maps. It shows that using pop-AIF may lead to significantly different TK maps.
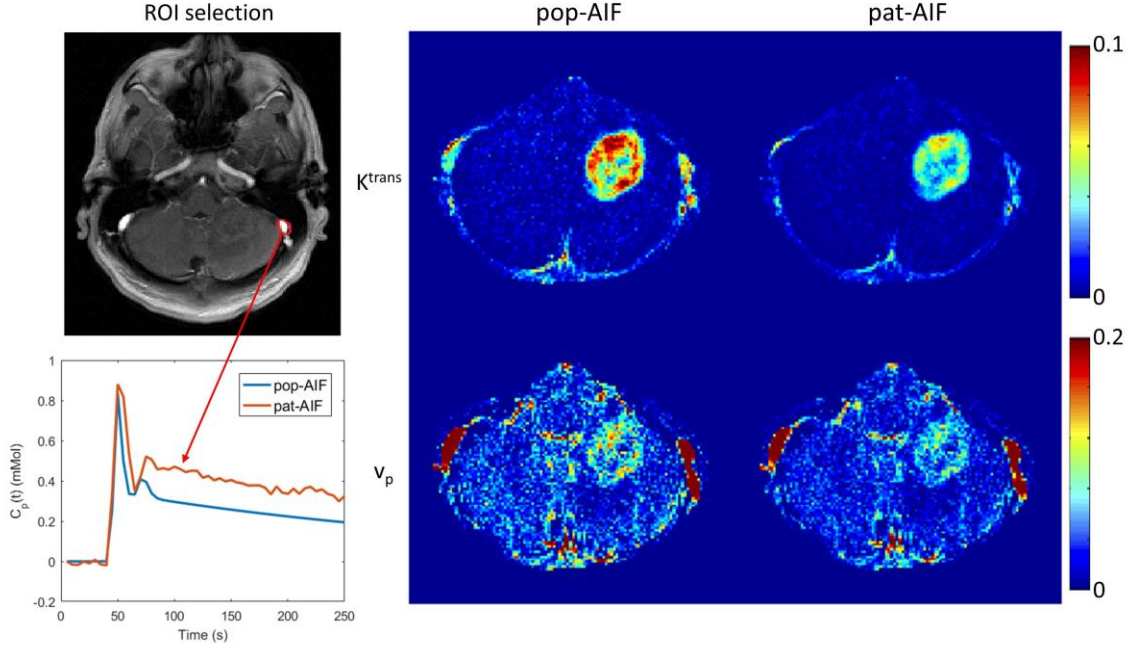
Figure 2.11 Illustration of extracting pat-AIF from a manually selected ROI, and comparison to pop-AIF (left). Patlak model parameter (K^{trans} and v_p) from these two different AIFs (right).

2.2.4 Tracker-kinetic (TK) Modeling

After contrast agent concentration (C) are estimated from the data, TK parameter maps can be derived from these contrast concentration curves. $C(t)$ and $C_p(t)$ are used to denote concentration in tissue and artery (i.e. AIF) in this section. TK parameter maps are the end-point product of DCE-MRI scan, these maps show important physiological information, and are of more importance to radiologists for diagnosis and treatment response. For example, the K^{trans} value, which is the forward transfer rate constant from plasma to intersititium, is correlated to the BBB permeability. This is considered a direct parameter to show tumor grade and severity (22, 23, 38). The plasma volume, v_p, is related to the blood volume in the plasma, and shows the normal or abnormal blood flow in patients (9, 22). K_{ep} is the interstitium-to-plasma rate constant, and is related to the reabsorption of contrast agent.

For the TK parameter modelling, different models exist to convert the concentration curves to TK parameters. Each of these models assume some approximation about the perfusion and flow condition. Table 2.2 lists 4 representative TK models of different complexity and their corresponding parameters and assumptions.

Table 2.2 List of 4 representative TK models and conditions

Model	Parameters	Condition
0. Null	0	insufficient vascular filling
1. Steady-state model	v_p	vascular filling with no microvascular leakage
2. Patlak model	K^{trans}, v_p	leakage without vascular reabsorption
3. extended Tofts model	K^{trans}, K_{ep}, v_p	leakage with reabsorption

In the brain tumor region, it is shown that three parameters of the extended-model are sufficient to fit dynamic contrast enhanced data for glioblastoma. And in slow leakage cases, two parameters of Patlak model provide reasonable approximation (39). The section below will introduce these two widely used TK models.

2.2.4.1 Common TK Models for Brain Tumor Evaluation

Extended-Tofts

A widely used TK model for brain tumor is the extended-Tofts model (eTofts) (9). This model is valid in highly perfused tissues and in weakly vascularized tissues with a well-mixed interstitium (40). The model is defined as the following fitting equation:

$$C(t) = K^{trans} \int_0^t C_p(u)e^{-K_{ep}(t-u)}du + v_p C_p(t) \tag{2.10}$$

The model fits three parameters (K^{trans}, K_{ep}, v_p). Though accuracy is sacrificed comparing to more general models, eTofts still provides meaningful TK values with high precision, and is useful in many clinical applications (40).

Patlak

The Patlak model is a linear simplification of eTofts mode, where backflux from interstitium is neglected. The model is defined as:

$$C(t) = K^{trans} \int_0^t C_p(u)du + v_p C_p(t) \tag{2.11}$$

Although Patlak assumes many extreme approximations, it is still widely used in many centers because it is linear and robust.

2.2.4.2   Model Selection

For this variety of TK models, no one is considered "correct" and gold-standard for DCE-MRI. Like quote from George E. P. Box, "all models are wrong, but some are useful". The models with more parameters to be fit like eTofts will provide better fitting for the data, but increase the variability of the estimated TK parameters (40–42). There lacks ground truth for TK parameters in DCE-MRI, and the injection of contrast agent to human body makes it difficult to test the precision and reproducibility of different modeling and imaging strategies. Many studies used simulated data to test the fitting performance of each model and reconstruction techniques, but this provides limited information about TK modelling in real patient data. If the fully-sampled data is available, a F-test based on the fitting errors of each model can be used to determine which model to use (39). However, this method is difficult to implement in under-sampling reconstruction scenario.

2.3   Sparse Sampling and Constrained Reconstruction

MRI imaging needs multiple phase encoding to encode the spatial information of the MR signal. This phase encoding step takes at least 3-5 ms each time, making a high-resolution 3D image up to 1-2 minute to be acquired. For DCE-MRI, to capture the dynamic changes during a contrast injection, trade-offs have to be made between spatial resolution, spatial coverage, and temporal resolution. Therefore, many techniques have been proposed to accelerate DCE-MRI scans. Most of these techniques focus on reconstructing proper images from under-sampled data. This section will review some of these techniques that are relevant to the author's main contribution.

Parallel imaging is a MRI technique that utilizes the redundancy in coil dimension to accelerate MRI scans. These techniques include SMASH (43), SENSE (17), GRAPPA (18), ESPIRIT (20) etc. As introduced in section 2.1.4 and 2.2.3, SENSE is already routinely used in clinical DCE-MRI to achieve 2x acceleration.

Compressed sensing (CS) is another technique that aims to reconstruct images from sparsely-under-sampled data (44). CS is particularly well suited for dynamic imaging, which can exploit the redundancy of information in the temporal dimension, either through dictionary-learning (45, 46), or high-pass filtering (47, 48). A combination of PI and CS has been shown to greatly accelerate the data acquisition, while achieving significantly higher spatio-temporal resolution and large spatial coverage with only slight image quality penalties (19, 20, 49).

Several groups have employed PI-CS techniques to improve DCE imaging. Zhang et al. (50) employed a locally low-rank constraint in combination with parallel imaging to achieve up to 19× acceleration rate in pediatric patients. Wang et al. (51) used a reference image-based compressed sensing and achieved acceleration factor of 10× without

degrading spatial resolution. Feng et al. (49) used compressed sensing, parallel imaging and golden-angle radial sampling to achieve fast and flexible DCE-MRI. Rosenkrantz et al. (52) examined 20 prostate cancer patients using a similar scheme to evaluate the results from constrained reconstruction against conventional DCE-MRI.

This section will give a general introduction on sparse sampling and constrained reconstruction for dynamic MRI imaging.

2.3.1 Sparse Sampling

Compressed sensing theory relies on random sampling of k-space, and a variety of sampling patterns have been proposed. Various non-Cartesian sampling schemes have been proposed over the years, and the literatures have shown that non-Cartesian sampling have multiple benefits over Cartesian sampling in terms of sampling efficiency, robustness to motion and suppression of off-resonance effects, etc. (30, 53, 54) However, non-Cartesian sampling is also expensive to implement on the MRI machine, and takes additional computational steps and effort for image reconstruction. In the context of 3D imaging, which is used in DCE-MRI (3D plus time), it is easy to sample the Cartesian k-space grid following a non-Cartesian style pattern. This pseudo-Cartesian sampling can benefit from both Cartesian and non-Cartesian sampling. Here we will focus on these pseudo-Cartesian sampling patterns for 3D imaging.

Figure 2.12 illustrates three representative pseudo-Cartesian sampling patterns: Poisson-Disc (PD), Golden-Angle Radial (GA), and Randomized Golden-Angle Radial (RGA). The undersampling rate (comparing to Nyquist fully sampling) is 30 folds (R=30x).

PD is a randomized sampling pattern that is initially proposed for compressed sensing, and has the benefit of creating incoherent artifacts that is easily removable by l_1 norm constraint (55). However, PD is initially proposed for static imaging, and in dynamic 3D imaging, different patterns have to be generated beforehand for each time frame with a fixed temporal window, providing less flexibility for dynamic imaging (56, 57).

GA is derived from conventional radial sampling with a golden-angle of 111.246° between each radial spokes to achieve an efficient coverage of k-space (53). When used in dynamic 3D MRI, GA can be used to continuously sample the (k,t)-space, and a group of spokes can be binned retrospectively to achieve arbitrary temporal resolution. Because of the property of golden-angle, each time frame will still have optimal k-space coverage.

RGA is a newly proposed sampling pattern that is tailored for dynamic 3D MRI, where both the benefits of PD and GA is inherited (57). RGA is based on GA Cartesian sampling, with random sampling of the k_y-k_z phase encode locations along each Cartesian radial spoke. This sampling pattern will have the benefit of incoherent sampling from PD, and arbitrary selection of temporal window from GA. Note that in the published literature, RGA is

acronymed as GOCART for "GOlden-angle CArtesian Randomized Time-resolved 3D MRI", here we still use RGA for easy understanding of the connection to original GA sampling.
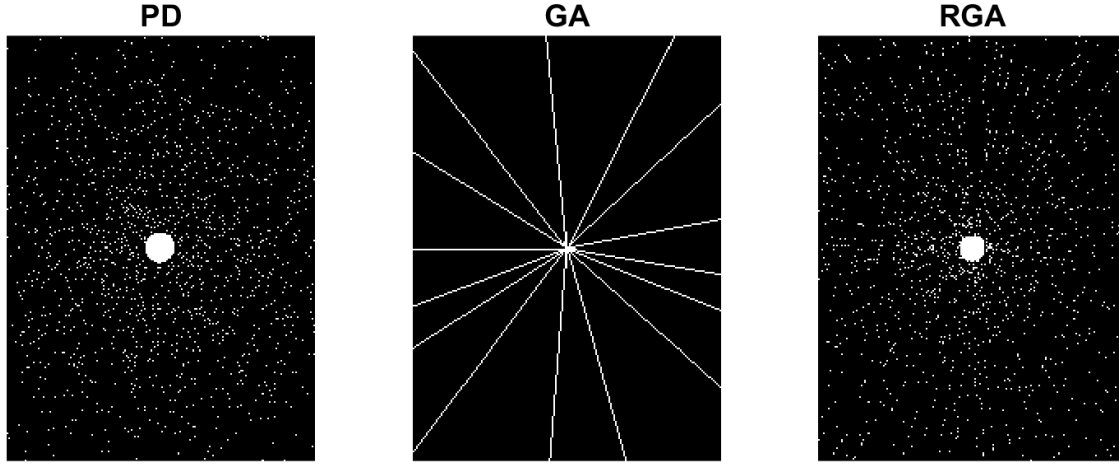
Figure 2.12 Illustration of Poisson-Disc (PD), Golden-Angle Radial (GA), and Randomized Golden-Angle Radial (RGA) sampling patterns at R=30x.

In this work, we mainly used traditional (GA) and randomized golden-angle (RGA) radial sampling patterns.

2.3.2 Constrained reconstruction

After under-sampled k-space data is acquired, we will use certain prior knowledge as constraints to restore the images from these under-sampled data. The reconstruction process mostly involves solving following optimization problem:

$$\hat{S} = \arg\min_{S} \| UFES - y \|_2^2 + \lambda R(S) \tag{2.12}$$

Where the first term is called data consistency, and it enforces that the image to be reconstructed (S) remains consistent with acquired k-space data (y). As introduced in section 2.3.2.2 and 2.2.3, U is the under-sampling matrix, F is the Fourier transform, and E is the coil sensitivity encoding. The second term is the constraints based on some prior knowledge of the images.

In the earlier literatures, l_2 norm constraints are proposed first to improve SNR and convergence speed. With the emergence of compressed sensing, l_1 or l_p norm that approximate l_0 norm condition have been proposed to enforce the sparsity of certain

transform domain of the images. The sections below will discuss different variants of constrained reconstruction, and various algorithms to solve them.

2.3.2.1   l₂ Norm Constraint

As introduced in section 2.1.4, in the initial publication on SENSE (17), it proposed to solve the original problem using matrix inversion (or pseudo-inverse). For simple linear sampling pattern and small data size, it is the most intuitive and straightforward way to solve the problem. However, if complicated sampling pattern is used, or if the data size is large, commonly we target to solve a least-square problem using iterative algorithm (e.g. conjugate gradient). And l₂ norm is used to provide stable convergence and better performance for a least-square problem. For example, Tikhonov regularization is a commonly used l₂ norm constraint (58):

$$\hat{x} = \arg\min_{x} \| UFEx - y \|_2^2 + \lambda \| L(x - x_0) \|_2^2 \tag{2.13}$$

, where L is a positive semi-definite linear transformation, x_0 denotes the prior information about the solution x. The regularization parameter λ determines the relative weights with which these two estimates of error combine to form a cost function. In optimization problem, an L-curve, as illustrated in Figure 2.13, is often used to determine an appropriate value of the regularization parameter that provides a good balance between the data consistency and the prior knowledge.
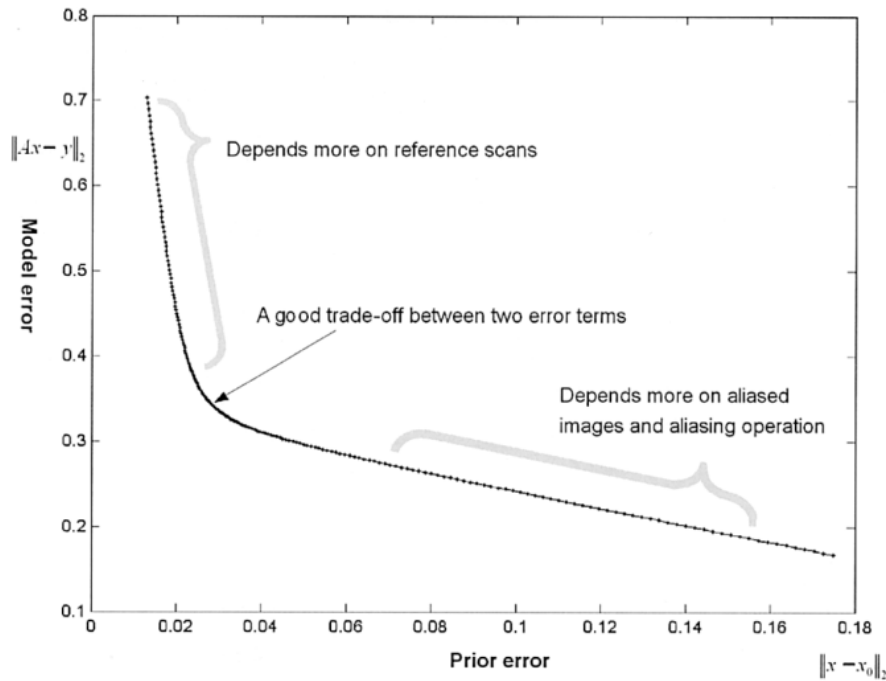
Figure 2.13 An *L*-curve illustrates the two costs during reconstruction of the aliased images from an array. Using distinct regularization, the reconstruction biases toward minimizing either the prior error or the model error. A trade-off between these two error metrics is the use of regularization at the "corner" of the L-curve. Reproduced from Lin F-H, Wang F-N, Ahlfors SP, Hämäläinen MS, Belliveau JW: Parallel MRI reconstruction using variance partitioning regularization. Magn Reson Med 2007; 58:735–744.

For parallel imaging techniques, l_2 norm is mainly helpful for convergence speed and stability, to achieve higher under-sampling rates or better reconstruction image quality, more constraints that better utilize the prior information of the image have been proposed.

2.3.2.2   Compressed Sensing (l_0 and l_1 Constraint)

In additional to SENSE, Compressed Sensing (CS) is a newly proposed under-sampling reconstruction technique that allows for higher acceleration in MRI (44, 59).

As shown in Figure 2.14, MRI images will be sparse in certain transform domain, where most of the signals are zeros. If we just use a portion of the largest values in these transform domain, we can still restore reasonably good quality images. CS technique utilizes this property of MRI image, and target to restore the images from vastly under-sampled *k*-space, with a constraint that the image should be sparse in certain transform domain.
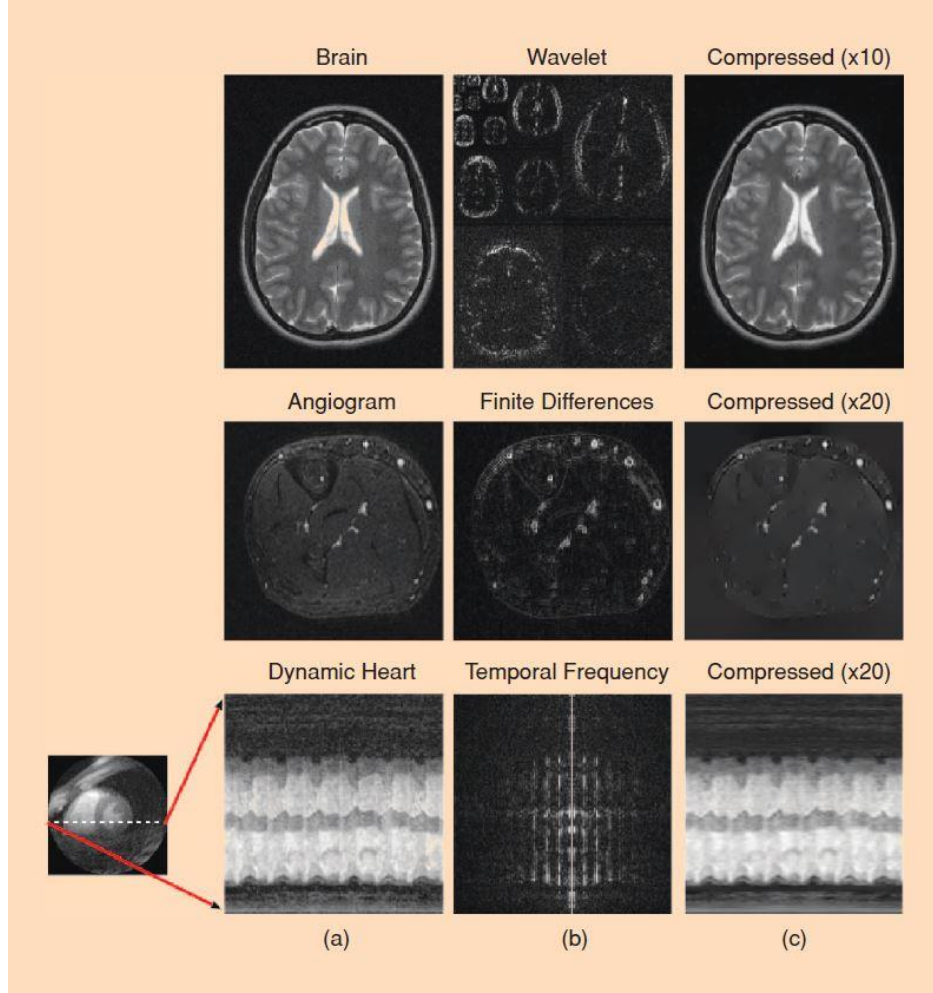
Figure 2.14 Transform sparsity of MR images. (a) Fully sampled images are mapped by a sparsifying transform to a (b) transform domain; the several largest coefficients are preserved while all others are set to zero; the transform is inverted forming a (c) reconstructed image. Reproduced from (59). 59. Lustig M, Donoho DL, Santos JM, Pauly JM: Compressed Sensing MRI. (March 2008):72–82.

Specifically, CS targets to reconstruct the image x from under-sampled k-space data y by solving the following constrained optimization problem:

$$\text{minimize} \qquad \|\psi x\|_0$$

$$\text{s.t.} \qquad \|UFEx - y\|_2 < \varepsilon \qquad\qquad (2.14)$$

, where Ψ is some sparsifying transform, U is the under-sampling matrix, F is Fourier transform and E is the coil sensitivity encoding. The l_0 norm is to enforce the sparsity of the transform domain coefficient. However, directly solving a l_0 norm constrained problem can be challenging, and some approximation approaches have been proposed.

In the initial publication on CS (55), l_1 norm is proposed to approximate l_0 norm, and the problem can be converted to an unconstrained form:

$$\hat{x} = \arg\min_x \| F_u Ex - y \|_2^2 + \lambda \| \psi x \|_1 \tag{2.15}$$

Where λ is the regularization parameter, or constraint penalty. Many iterative algorithms can be used to solve this optimization problem. For example, non-linear conjugate gradient algorithm is proposed to solve the problem by calculating the gradient of the cost function. And for l_1 norm, the gradient is calculated by relaxing the l_1 norm to an approximating l_2 norm.

Another important algorithm for solving constrained reconstruction problem is augmented Lagrangian methods, where auxiliary variables are introduced to split the original problem into easy sub-problems. For Equation (2.15), auxiliary variables u and v can be introduced to split the problem into:

$$\min_{u,v} \| y - UFu \|_2^2 + \lambda \| v \|_1 \ \ s.t \ \ v = Tx, u = Ex \tag{2.16}$$

And convert into an unconstrained problem:

$$\min_{u,v,S_t,e_1,e_2} \| y - UFu \|_2^2 + \lambda \| v \|_1 + \rho_1 \| TS_t - v - e_1 \|_2^2 + \rho_2 \| Ex - u - e_2 \|_2^2 \tag{2.17}$$

And during iteration, each variable can be solved alternatively while keeping other variables constant. This method is also called alternating direction method of multipliers (ADMM). Detailed algorithms how to solve each step can be found in Chapter 3.

Chapter 3. Clinical Evaluation of Constrained Reconstruction in Brain DCE-MRI

3.1   Introduction

T_1-weighted DCE-MRI is a valuable albeit still evolving technique for mapping the spatial distribution of brain vascular parameters such as perfusion, permeability, and blood volume (8, 60). It employs serial T_1-weighted imaging before, during and after a bolus injection of a gadolinium-based contrast agent (GBCA). Changes in GBCA concentration is derived from changes in signal intensity, then regressed to quantify tracker kinetic (TK) parameters such as K^{trans} (volume transfer constant), v_p (fractional plasma volume), and v_e (fractional extravascular extracellular space volume) (9, 22). DCE-MRI is used for quantitative assessment of brain tumors(10, 24, 61), multiple sclerosis lesions (25), and Alzheimer's disease (26) and other neurological disorders that involve blood-brain barrier (BBB) disruption. DCE-MRI is also used in clinical oncologic imaging for assessment of breast (62) and prostate (63) cancer. In brain tumor evaluation, BBB permeability is typically characterized by K^{trans} (9). While its interpretation may be complex, with some dependency on blood flow, K^{trans} correlates with tumor severity and may be a useful biomarker for monitoring therapeutic response and outcome (9, 25, 38, 64–66) .

Despite its usefulness, conventional clinical DCE-MRI is limited by suboptimal image acquisition that results in low spatial/temporal resolution and insufficient spatial coverage. Low temporal resolution has also been linked to poor reproducibility of TK parameters (23). A typical clinical DCE scan provides 2-30 s temporal resolution to detect signal intensity changes resulting from contrast agent perfusion (8, 52). As a result, the in-plane voxel dimensions usually exceed 1 mm^2 and the slices are often greater than 5 mm thick. The spatial coverage is often inadequate to cover the known pathology, such as in the setting of multiple metastatic lesions.

Recently, compressed sensing (CS) theory has inspired a wide array of new data acquisition and constrained reconstruction strategies that aim to reconstruct images from sparsely-under-sampled data (44). CS is particularly well suited for dynamic imaging, which can exploit the redundancy of information in the temporal dimension, either through dictionary-learning (45, 46), or high-pass filtering (47, 48). A combination of parallel imaging (17) (PI) and CS has been shown to greatly accelerate the data acquisition, while achieving significantly higher spatio-temporal resolution and large spatial coverage with only slight image quality penalties (19, 20, 49).

Several groups, including ours, have employed PI-CS techniques to improve DCE imaging. Zhang et al. (50) employed a locally low-rank constraint in combination with

parallel imaging to achieve up to 19× acceleration rate in pediatric patients. Wang et al. (51) used a reference image-based compressed sensing and achieved acceleration factor of 10× without degrading spatial resolution. Feng et al. (49) used compressed sensing, parallel imaging and golden-angle radial sampling to achieve fast and flexible DCE-MRI. Rosenkrantz et al. (52) examined 20 prostate cancer patients using a similar scheme to evaluate the results from constrained reconstruction against conventional DCE-MRI.

Several groups have also utilized under-sampling and constrained reconstruction techniques to accelerate Contrast-Enhanced (CE) Magnetic Resonance Angiography (MRA). CE-MRA is particularly amenable to this approach because subtraction angiograms are sparse in the image domain. Barger et al. (67) used under-sampled 3D projection reconstruction trajectories and a "tornado" view-sharing scheme to achieve isotropic resolution, broad coverage and 4s temporal resolution. The typical aliasing when using under-sampling is mitigated by the high-contrast properties in MRA. Haider et al. (68) used a Cartesian radial technique in combination with 2D SENSE, partial Fourier and view sharing to achieve 1-2 mm isotropic resolution and subsecond temporal resolution. With emerging CS techniques, Trzasko et al. (69) demonstrated reduced noise and artifacts level in Cartesian radial sampling MRA by utilizing a sparsity-driven nonconvex CS method, and Lee et al.(70) achieved 1-mm isotropic resolution, 1.1s frame rate (corresponding to an acceleration factor of >100×) with a CS based GraDeS algorithm. In CE-MRA, high spatio-temporal resolution and broad coverage is achieved by exploiting high image contrast and a high degree of image domain sparsity.

Accelerating DCE-MRI for the purpose of pharmacokinetic modeling is more challenging than for CE-MRA since the reconstruction is not spatially sparse and TK modeling is performed based on every signal containing voxel. Furthermore, reconstruction fidelity must be very high for accurate modeling whereas moderate error in visually assessed angiograms is often tolerable. Finally, the dynamic range of contrast-induced signal change is smaller in tissue than in vessels, enabling subtle compression artifacts to translate into noticeable errors in tissue parameters. The novelty of our proposed approach is that multiple sparsity constraints are employed in different sparse transform domains, each with low weight (56), mitigating biased artifacts producing from one heavy constraint. We have been able to achieve the highest acceleration rate reported in the literature to date, 36×, with excellent image quality. This enabled near isotropic voxel dimensions with whole-brain coverage for DCE-MRI.

Despite the promise of PI-CS methods, these techniques are poorly validated. Most validation has been done by retrospectively discarding data from fully sampled data sets or using phantom simulation. Both approaches provided ground truth, but are imperfect due to unrealistic data acquisition or anatomical features. Prospectively under-sampled studies

demonstrate the potential of the method, but lack ground truth images and have not been well validated. In this work, we present the first, to the best of our knowledge, prospective clinical evaluation of accelerated DCE-MRI using constrained reconstruction in brain tumor patients.

3.2 Materials and Methods

3.2.1 High-Resolution Whole-Brain DCE-MRI

The experimental DCE-MRI scan was based on a conventional Cartesian T_1-weighted 3D SPoiled fast GRadient echo (SPGR) sequence. The flip angle was 15º, TE was 2 ms, and TR was 6 ms. The phase encoding order was altered to follow a Cartesian-grid golden-angle radial scheme (53, 71, 72), which acquired k_y-k_z phase encodes following golden-angle rotating radial spokes. The frequency encoding direction k_x was fully sampled. Cartesian SPGR scans with flip angles of 2º, 5º, and 10º, were performed sequentially for DESPOT1 (73) T_1 mapping prior to both the conventional and experimental DCE scans.

The Cartesian golden-angle radial sampling scheme provides incoherent k-space sampling, even at very high acceleration rates, where only a few spokes are presented within one time frame (49, 52). This approach provides comparable image quality as Poisson-ellipse sampling, which has been used in similar l_1-based reconstruction (72). All samples fall on a 3DFT Cartesian grid, therefore the Fast Fourier Transform operator can be directly applied. We have implemented this sampling scheme on a clinical scanner (3T GE Signa Excite HDx scanner), where the phase encode order table can be generated in response to operator input. The implementation is straightforward, since no additional modification of the existing gradient waveform is needed.

The under-sampled raw data was reconstructed using a sparse SENSE reconstruction scheme that utilizes multiple l_1-norm constraints with very low weights, as described in Ref (56). These sparsity penalties were chosen based on expected spatial and temporal characteristics of DCE-MRI images. Reconstruction involved solving the minimization problem in Equation (3.1), where the final image, x, remains consistent with the acquired data, y, yet is sparse in the temporal finite difference (V) domain, the spatial 'db2' wavelet domain (Ψ), and the spatial total variation domain (TV). The image is related to the acquired data using known coil sensitivities encoding (E) and the under-sampling Fourier transform UF. Coil sensitivity maps were generated by computing a density compensated average of all k-space data acquired at all DCE time points. This resulted in high-SNR time-averaged 3D k-space dataset that was fully-sampled. Individual coil maps were then computed in the

standard way, by dividing each individual coil image by the root sum-of-squares image (17).

$$S_t = \operatorname*{argmin}_{S_t} \| UFES_t - y \|_2^2 + \lambda_1 \| VS_t \|_1 + \lambda_2 \| TVS_t \|_1 + \lambda_3 \| \psi S_t \|_1 \qquad (3.1)$$

This optimization problem is then solved by an efficient augmented-Lagrangian method, Alternating Direction Method of Multipliers (ADMM), which performs variable splitting twice (74). This algorithm is one of many state-of-the-art algorithms to solve these l_1-constrained minimization problems (19, 44). This particular algorithm was chosen because it provides fast convergence (74–76).

All sparsity transforms can be denoted by a tall matrix T, that is $T = [V, TV, \psi]^T$. Dummy variables u, v are used to split Equation (3.1) to Equation (3.2), where λ is a long vector that has λ_1, λ_2 and λ_3 in the corresponding transform location.

$$\min_{u,v} \| y - UFu \|_2^2 + \lambda \| v \|_1 \quad s.t \quad v = TS_t, u = ES_t \qquad (3.2)$$

Then Lagrangian method is used to convert Equation (3.2) to an unconstrained problem in Equation (3.3):

$$\min_{u,v,S_t,e_1,e_2} \| y - UFu \|_2^2 + \lambda \| v \|_1 + \rho_1 \| TS_t - v - e_1 \|_2^2 + \rho_2 \| Ex - u - e_2 \|_2^2 \qquad (3.3)$$

Where e_1, e_2 are Lagrange multiplier terms, and ρ_1, ρ_2 are penalties for the axillary dummy variables. With the Lagrange terms (e_1, e_2), the penalty parameters (ρ_1, ρ_2) need not tend to large values for the equivalence of Equation (3.1) and Equation (3.2) to hold; the value of these parameters does not affect the final solution, just the rate of convergence. We empirically chose them to be 0.05.

Denoting the objective function in Equation (3.3) as $L(S_t, u, v)$, the problem can be decoupled to simpler well-defined sub-problems, where every sub-problem takes an analytical form, and can be solved in a single step. The algorithm relies on iterating between these sub-problems until convergence to a guaranteed global minimum. These steps are:

Initialization :

Select S_t^0, $u^0 = ES_t^0$, $v^0 = TS_t^0$, and $n = 0$

Repeat :

$$S_t^{n+1} = \underset{x}{\operatorname{argmin}}\, L(S_t, v^n, u^n) = [\rho_2 E'E + \rho_1 T'T]^{-1}(\rho_2 C'(u^n + e_2^n) + \rho_3 T'(v^n + e_3^n))$$

$$u^{n+1} = \underset{u}{\operatorname{argmin}}\, L(S_t^{n+1}, v^n, u) = [F_u'F_u + \rho_2 E'E]^{-1}(F_u'y + \rho_2(ES_t^{n+1} - e_2^n))$$

$$v^{n+1} = \underset{v}{\operatorname{argmin}}\, L(S_t^{n+1}, v, u^{n+1}) = shrink(TS_t^{n+1} - e_1^n; \lambda / \rho_1)$$

$$e_1^{n+1} = e_1^n + (v^{n+1} - TS_t^{n+1})$$

$$e_2^{n+1} = e_2^n + (u^{n+1} - CS_t^{n+1})$$

$$n = n + 1$$

Until stopping criterion is met

Note that *E'E=I* because of the properties of the sensitivity maps, the above steps were simplified into 5 steps compared to 7 steps in Ref (74), which accelerated the reconstruction and simplified the workflow.

In this study, regularization penalties were chosen empirically based on retrospective studies. A fully sampled DCE data set was retrospectively under-sampled at the same acceleration rate as our prospective data, then repeatedly reconstructed with a range of constraint penalties. Normalized root Mean squared error (nRMSE) was calculated between the fully-sampled and reconstructed data sets. Penalties were chosen to maintain near-minimal nRMSE, yet provide traction during reconstruction - essentially locating the corner point of the l-curve (77). We employed penalties of 0.01, 0.0001, 0.0001 for temporal finite difference, spatial TV and spatial wavelet respectively for all subsequent reconstructions. In retrospective studies, we found that reconstruction converged well within 100 iterations. We therefore allowed a maximum of 100 iterations in this prospective study, to provide control of the maximum reconstruction time.

3.2.2   Experimental Methods

Fifteen brain tumor patients were recruited from three of our affiliated sites. Informed consent was obtained from patients prior to MRI scan. Our Institutional Review Board approved this study and all procedures.

MRI scans were performed on a clinical 3T scanner (HDxt, GE Healthcare, Waukesha, WI) with an eight-channel head coil. Two DCE scans were performed: a standard ("conventional") scan using the vendor supplied sequence and our highly accelerated ("experimental") scan. Both DCE acquisitions used a 3D SPGR sequence. Prior to each

scan, T_1 maps were acquired using variable flip angle DESPOT1 method (73). The standard clinical post-contrast T_1 weighted scans (Coronal T_1-weighted FSPGR sequence, 1.0 mm^3 isotropic resolution, 22x22x20 cm^3 FOV) were used as the reference for lesion identification (4, 7).

Table 3.1 shows the conventional-then-experimental imaging protocol, which required less than 50 minutes. The contrast agent, Gadobenate dimeglumine (MultiHance Bracco Inc.) was administered with a dose of 0.05 mMol/kg, followed by a 20 ml saline flush in the left arm by intravenous injection for each scan (this results in a total of 0.1 mMol/kg which would be the standard dose for a DCE-MRI with contrast). The two DCE scans were separated by approximately 20 minutes, resulting in residual GBCA present in the second scan. This residue results in underestimation of K^{trans} values for the second scan.

Table 3.1 Comprehensive MRI protocol for a brain tumor patient in our study with a conventional-then-experimental DCE-MRI order. Conventional and experimental DCE scans are in bold, and separated by roughly 20 minutes. The conventional and experimental scans were reversed for the last two patients.

Duration (mm:ss)	Sequence
1:00	Localization and SENSE calibration
4:00	Pre-contrast Axial T1w FSPGR
5:00	Pre-contrast Axial T2w FSE
5:00	Pre-contrast Axial FLAIR
0:45	T1 mapping
4:08	**Conventional DCE**
15:00	Diffusion Tensor Imaging
0:45	T1 mapping
5:29	**Experimental DCE**
2:00	Post-contrast Axial T1w FSPGR
3:00	Post-contrast Coronal T1w FSPGR
<50:00	TOTAL

In this study, a Patlak model was used to estimate TK parameters for conventional and experimental scans. The following equation shows the fitting of K^{trans} and v_p from contrast concentration curves of plasma $C_p(t)$ and tissue $C_t(t)$:

$$\Delta C_t(t) = K^{trans} \int_0^t C_p(\tau)d\tau + v_p C_p(t) \tag{3.4}$$

$C_p(t)$ is the arterial input function (AIF), where we used a population-based analytic form (36), and $\Delta C_t(t)$ is the GBCA concentration change in the tissue, which is derived from the signal intensity in the dynamic images. K^{trans} is the volume transfer constant and v_p is the fractional plasma volume.

The Patlak model is used because it is robust to noise, in part due to its simplicity and the dependence on linear (v.s. nonlinear) estimation(40, 78). The model is based on the assumption that there is no backflux from the interstitium during a short scan (40). This assumption is not satisfied for the second injection in which residual GBCA in the interstitium from the first scan causes backflux that cannot be ignored. Use of this model causes underestimation of K^{trans} values for the second scan, as we illustrate below using simulations.

The double-injection experiment is simulated using the more accurate two-compartment exchange model (2CXM). Figure 3.1 (a) shows simulated $C_p(t)$ and $C_t(t)$ with 20 minutes separation between injections. Figure 3.1 (b) shows the simulated $\Delta C_t(t)$ from first and second injections, where the arrows indicate the altered curve due to residual GBCA. This residual, indicated with yellow circles in Figure 3.1 (a), is directly related to the extracellular extravascular volume fraction and the GBCA concentration in the extracellular extravascular space prior to the second injection. The end result is 16% to 50% underestimation of K^{trans} for the second scan. This projected range is based on TK parameter values reported in the literature for brain tumor (78). Figure 3.1 (c) shows measured $\Delta C_t(t)$ curves from a representative tumor voxel in one case in our study.

To further determine if this underestimation is caused by injection order, we performed experiments in three brain tumor patients, where the conventional DCE-MRI scan was performed twice in a single session. In the three subjects, tumor K^{trans} was underestimated in the second scan by 15%, 0%, and 24%. We consider this data to be anecdotal, but consistent with the simulations and the observed underestimation in the second scan of the conventional-then-experimental and experimental-then-conventional patient scans. Figure 3.2 (a-d) contains zoomed anatomic images from the 24% case before and after contrast injection for the two scans, where contrast residue can be seen in the second scan. Figure 3.2 (e) and (f) contain zoomed K^{trans} maps, where the second scan produced lower estimated K^{trans} compared to the first scan. In this case the mean K^{trans} values in tumor ROI from the second scan was 24% lower than the first scan. Figure 3.2 (g) shows measured $\Delta C_t(t)$ curves in these two conventional scans, which matches the trend observed in simulations, conventional-then-experimental scans, and experimental-then-conventional scans.
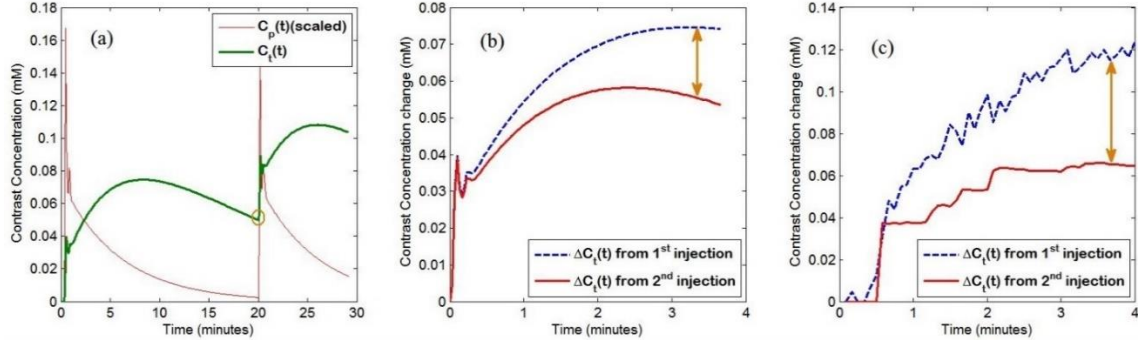
Figure 3.1 (a) The 2CXM simulated contrast concentration curves $C_p(t)$ (scaled by 0.2×) and $C_t(t)$ for double injections, separated by 20 minutes. (b) $\Delta C_t(t)$ calculated from the 1st and 2nd injections, where $\Delta C_t(t)$ from the 2nd injection is lower primarily due to high backflux from the tissue to the plasma. (c) Actual measured $\Delta C_t(t)$ curves in one tumor voxel from a representative patient data, which matched the trend of the simulation.
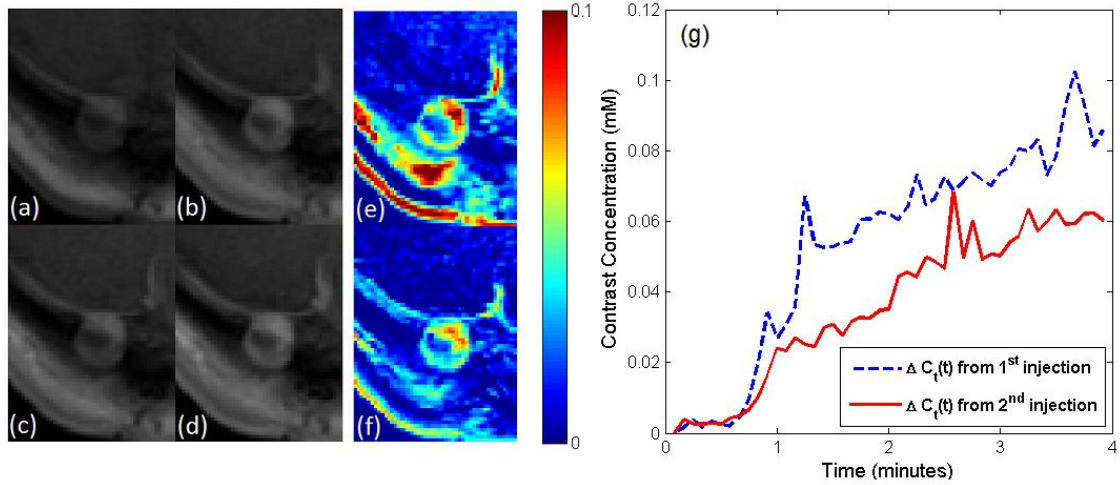

Figure 3.2 (a), (b): Pre- and post- contrast images of first conventional DCE scan, cropped around an enhancing tumor. (c), (d): Pre- and post- contrast images from the second conventional DCE scan. (e): K^{trans} maps from first DCE scan, (f): K^{trans} maps from second DCE scan. (g): Measured $\Delta C_t(t)$ curves in the tumor ROI for the two conventional scans.

Conventional-then-experimental protocols were performed in the first 13 patients, for the last two cases, we switched the order of the conventional and experimental scans and created an experimental-then-conventional protocol. This was for the purpose of verifying that K^{trans} underestimation in the second scan was due to the scan order and residual GBCA, and not due to the imaging methods.

Table 3.2 lists acquisition parameters for the two DCE scans. The experimental scan achieved much smaller voxel dimensions and whole-brain coverage, while maintaining the same temporal resolution as the conventional scan. A net acceleration factor of *30×* was

achieved. All 15 brain scans had the same field-of-view, matrix size, voxel dimensions, scan time, and phase encode order. (k,t)-space was under-sampled in the exact same fashion for all subjects. The injection delay for the experimental method was 60 sec, compared to 20 sec for the conventional method, in order to allow time for fully sampling of 25% of phase encodes prior to contrast arrival.

Table 3.2 Scan parameters for the standard conventional and experimental high-resolution whole-brain DCE-MRI scans. The experimented scan slice thickness is less than one third of that of conventional scan, and the slice number is 17 times greater than that of conventional scan. This enables a whole-brain near-isotropic coverage of the experimental scan while keeping the same temporal resolution.

	Conventional	**Experimental**
TR/TE	6ms/2ms	6ms/2ms
Flip Angle	15º	15º
Matrix size	256×186×6	256×256×100
FOV (cm³)	22×22×4.2	22×22×19
Voxel dimensions (mm³)	0.93×1.3×7	0.93×0.93×1.9
Temporal resolution	5 s	5 s
Injection delay	20 s	60 s
Total scan time	4min 08s	5min 29s
Time frames	50	61
Sampling Pattern	Cartesian 3DFT linear order	Cartesian 3DFT golden-angle radial order
Acceleration factor	2x	30x

3.2.3   Comparisons / Evaluation

The conventional and experimental DCE-MRI scans were registered based on the peak-contrast images using MATLAB image registration toolbox. As the experimental scan had whole-brain coverage, slices within the FOV of the conventional scan were located by registration. For fair evaluation, three adjacent slices of the high-resolution experimental scan were averaged to match the slice thickness of the conventional scan. Then K^{trans} maps were computed using the Patlak analysis (22, 40, 79), and a population-averaged analytic arterial input function (AIF) (36).

Quantitative evaluation was performed using the K^{trans} histogram within radiologist-defined ROI (66, 80–82). Under the guidance of an experienced neuroradiologist (20 years

of experience), tight ROIs were drawn on K^{trans} maps to included the highest K^{trans} values. The maximum K^{trans} values were calculated for both scans and compared.

Qualitative evaluation was performed using radiologists' rating. Two experienced neuroradiologists (10 and 20 years of experience respectively) from our institution reviewed and scored the images. For each subject, three types of images were shown for the conventional and experimental scans (a total of six image sets): 1) time-resolved images of one slice through the tumor (three slices averaged in experimental scan), 2) post-contrast–enhanced images (no slice average for experimental scan) and 3) BBB permeability K^{trans} maps. Radiologists were blinded to the acquisition type (conventional or experimental), and the presentation order for every scan was randomized. A 4-point Likert scale was used to quantify the general image quality, where 3 = good, 2 = average, 1 = poor, 0 = non-diagnostic.

In the second round of qualitative evaluation, the same Neuroradiologists were shown the full resolution conventional and experimental DCE-MRI results, and were asked to evaluate three sub-categories of image quality: (1) SNR, which incorporates the visual appearance of noise, (2) apparent spatial resolution, which incorporates sharpness of the images, and (3) conspicuity of tumor enhancement, which incorporates the detectability and sensitivity of contrast enhancement in the tumor. For each category, readers were asked to determine if the conventional scan was superior, if the two were equal, or if the experimental scan was superior. Conventional and experimental scan images (post-contrast images, time-resolved images, and K^{trans} maps) were shown to the radiologists, who were not blinded to the scan type.

3.3   Results

3.3.1   Experimental Results

Table 3.3 contains the demographic and clinical information for the 15 patients that were included in the data analysis. All experimental data sets were reconstructed using the same empirical constraint penalty values (the λ's in Equation (3.1)). Reconstruction time was roughly 8 hours per dataset.

Table 3.3 Patient demographic and clinical information of the fifteen brain tumor patients participated in the study.

No.	Sex	Age	Symptom	Tumor size (cm)*
001	F	46	Glioblastoma	2.4
002	M	71	Glioblastoma	2.3
003	F	76	Meningioma	1.9
004	F	53	Metastasis	3.4
005	M	26	Astrocytoma	1.6
006	M	77	Meningioma	0.8
007	M	72	Metastatic melanoma	1.0
008	M	65	Glioblastoma	6.0
009	M	71	Glioblastoma	1.5
010	F	65	Metastatic ovarian cancer	1.3
011	F	38	Glioblastoma	0.5
012	F	72	Meningioma	1.4
013	F	22	Glioblastoma	2.4
014	F	78	Metastatic Melanoma	1.6
015	F	59	Meningioma	3.9

* Tumor size was measured by the longest diameter in the post-contrast T1w images.

Figure 3.3 shows typical post-contrast-enhanced DCE-MRI images from two subjects, one with a large 6 cm glioblastoma; the other with multiple metastatic melanoma tumors scattered throughout the entire brain. The experimental approach was able to provide detailed depiction of the entire tumor body and tumor boundary, and capture all the possible small lesions (14 in total) in the whole coverage of the brain (see arrows). The tumor boundary was clearly visualized in any scan plane, and small, scattered lesions were easily identified in coronal/sagittal reformats. Conversely, the conventional scan provided limited spatial coverage (only 4 lesions were captured), and the sagittal and coronal reformats had extremely low resolution in the slice encoding direction. In all cases, the experimental scan provided clearer and crisper depictions of all lesions that were presented.

Another benefit of whole-brain coverage is that it essentially eliminates inflow enhancement artifacts. Figure 3.3 (c) shows bright signal in the sagittal sinus stemming from inflow enhancement in a conventional scan where only a 6cm axial slab is imaged. This inflow enhancement was consistently observed in every conventional scan and is strongest in slices at the edge of the imaging slab. In contrast, Figure 3.3 (d) shows that inflow enhancement was not present in the experimental scans.

Figure 3.4 demonstrates registered anatomic images and K^{trans} maps from two other representative patients, with conventional-then-experimental and experimental-then-conventional protocols respectively. Note that the experimental images were blurred in the slice-encoding direction to match the conventional protocol. Anatomic images yielded similar quality in the regions of interest. K^{trans} measurements from the second scan were consistently 42% to 66% of that from the first scan in the ROI of the tumor, regardless of the scan order. The K^{trans} maps, despite intensity differences (due to scan order), provided comparable information and superior image quality based on the radiologists' ratings, described below.
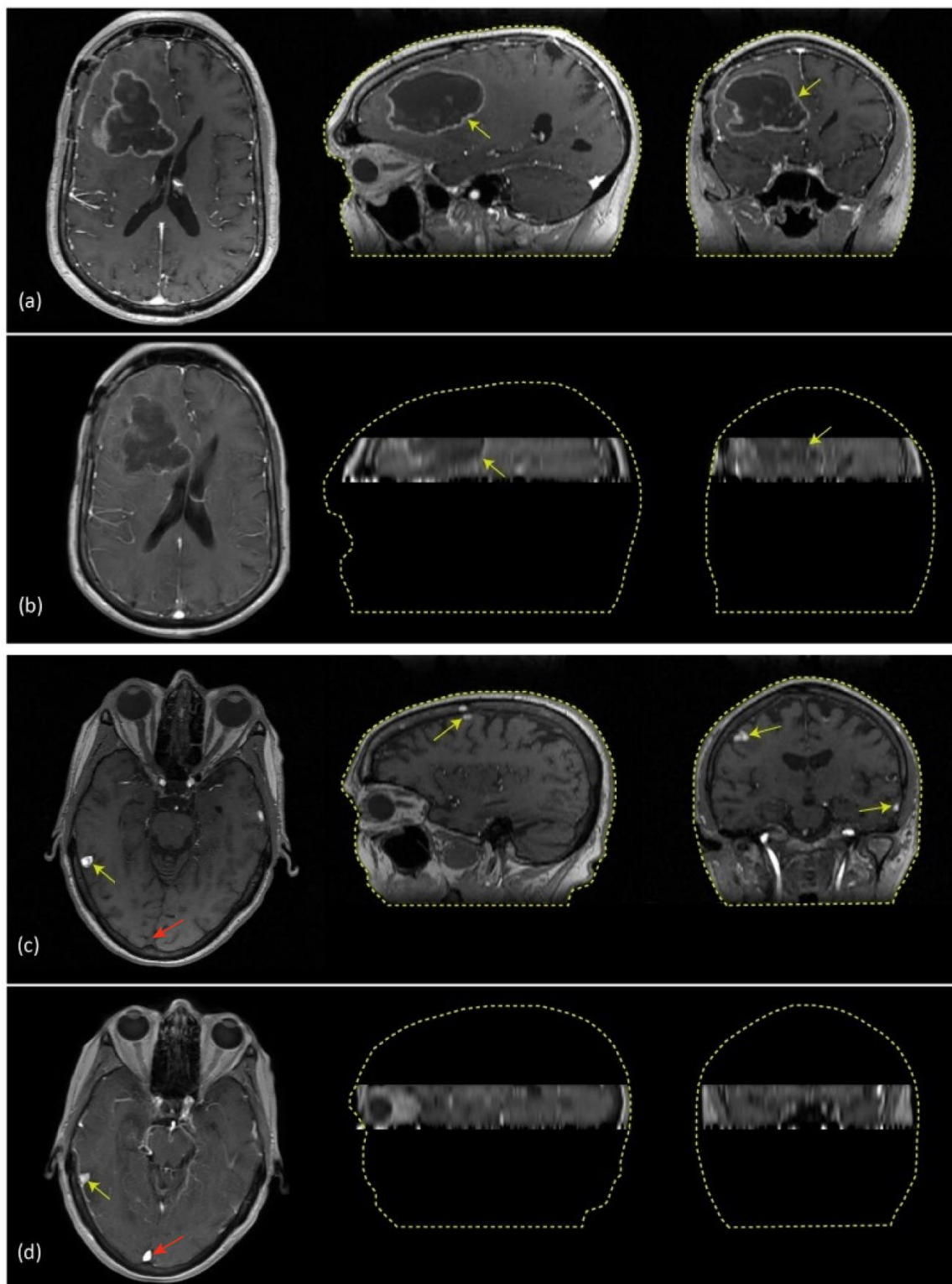
Figure 3.3 Final DCE-MRI time frames from two patients illustrating the volume coverage of (a,c) experimental and (b,d) conventional scans. **(a,b):** 65/M patient with a 6 cm glioblastoma tumor (subject #008). Experimental scan (a) shows significantly larger coverage than the spatial coverage of the conventional scan (b), where on the sagittal and

coral reformats only a thin slab of brain can be covered. **(c,d):** 78/F patient with metastatic melanoma (subject #014), only 4 lesions were captured by the clinical scan (d), all 14 lesions were captured by the experimental scan (c). Note that the conventional scans show bright signal in the sagittal sinus (red arrows) and other blood vessels due to inflow enhancement that are not present in the experimental scans because of the whole-brain coverage. This was consistently observed in all subjects.
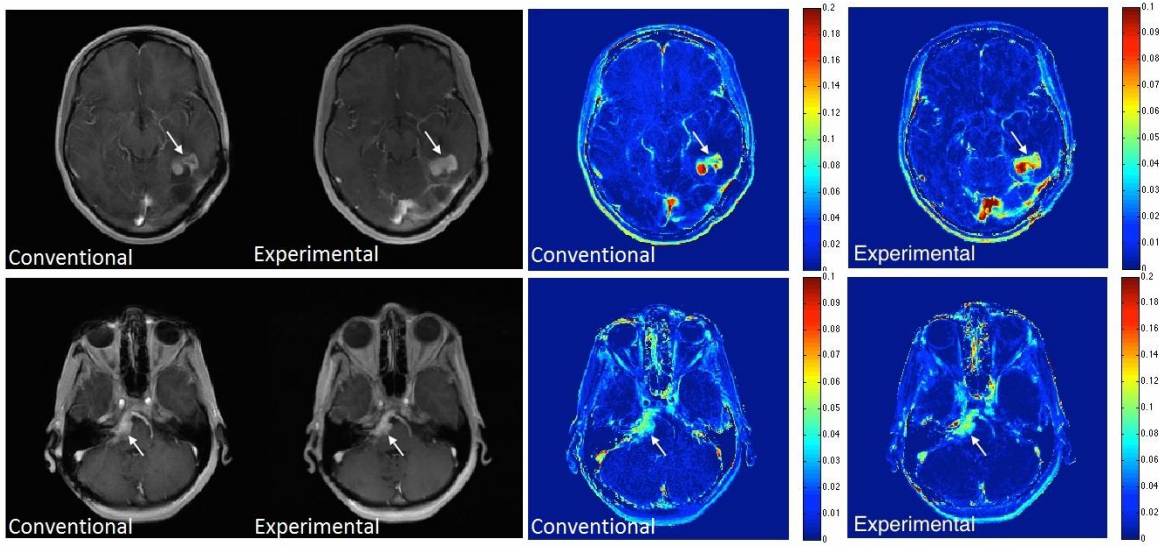

Figure 3.4 Registered anatomic images and K^{trans} maps from two other representative patients. On the left are the registered anatomic images; on the right are K^{trans} maps. The top row is from patient #013 with a glioblastoma (see arrows) using conventional-then-experimental protocol. The bottom row is from patient #015 with a meningioma (see arrows) using experimental-then- conventional protocol. Both sets of anatomical images provide comparable features and image quality, and the K^{trans} maps convey comparable diagnostic information despite intensity differences.

3.3.2 Quantitative Assessment

Figure 3.5 shows a scatter plot of the maximum K^{trans} value within manually segmented tumor ROIs between two DCE-MRI scans. Each pair of scans was performed using one of three possible orderings: conventional-then-experimental (blue circle), experimental-then-conventional (green diamond), and double conventional (red star). Although the second scan underestimates K^{trans}, the two measurements were still highly correlated with correlation coefficient r=0.513. The mean difference between the two scans was 0.036, which corresponds to a consistent negative bias consistent with contrast residue from the previous injection.
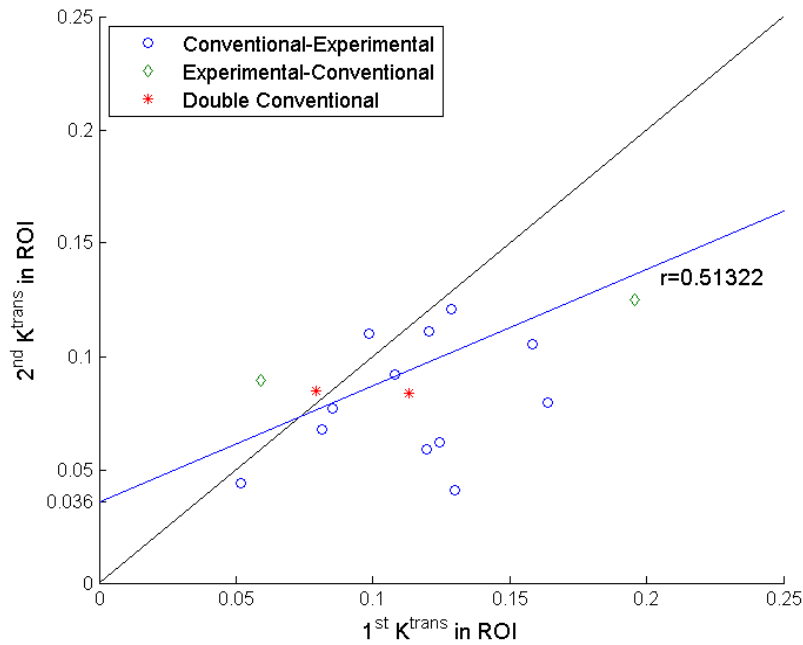
Figure 3.5 Scatter plot of the maximum K^{trans} in tumor ROIs for the 1st and 2nd DCE-MRI scans. Conventional-then-Experimental (13 cases), Experimental-then-Conventional (2 cases) and Double Conventional (2 cases) are all shown. The correlation coefficient was 0.5132. The second scan experienced a consistent underestimation of K^{trans} due to contrast residue.

3.3.3   Qualitative Assessment

Table 3.4 lists the two radiologists' ratings of the images. The Likert scale scores of overall image quality were averaged across image types, and shown for all 15 patients. The three sub-categories, SNR, apparent resolution, and conspicuity of tumor enhancement, were shown as experimental-better (denoted by '+'), scans are equal (denoted by '='), or conventional-better (denoted by '–'). Both radiologists consistently rated the experimental scans as higher or equal in quality to the conventional scans in terms of SNR, effective resolution, and fine details. The conventional scan was not deemed superior to the experimental scan in any of the cases by either radiologist. The radiologists also indicated that they observed "better white/gray matter contrast," "improved resolution and edge sharpness," "reduced phase-encoding artifacts," "reduced noise level," and "better detection of tumor with large coverage of the brain," from the experimental scan images.

Table 3.4 Two radiologists' scores across the 15 patients for conventional and experimental DCE-MRI scans. A 4-point Likert scale was used to score the overall image quality (3 = good, 2 = average, 1 = poor, 0 = non diagnostic), and the average of this score was taken for each patient across the three image types. Three sub-categories of image quality (SNR, apparent resolution, conspicuity of tumor enhancement) were scored as: +: experimental-better, =: equal, -: conventional-better. (I: Radiologist 1. II: Radiologist 2).

NO.	Average Likert score				SNR		Resolution		Conspicuity	
	Conventional		*Experimental*							
	I	*II*	*I*	*II*	*I*	*II*	*I*	*II*	*I*	*II*
1	1	1.67	2	1	+	+	+	+	+	+
2	1	1	2.33	1.67	+	+	=	+	+	+
3	1	1	2	1.67	+	+	+	+	=	+
4	1.67	1.33	2.67	1.67	+	+	+	+	=	+
5	1	1.33	2.33	1.67	+	+	+	+	=	+
6	1.33	1	2.67	2	+	+	+	+	=	+
7	1	2.33	3	2	=	=	=	+	+	+
8	1	1.33	3	2.33	+	+	+	+	+	+
9	1	1.67	2.33	2	+	+	=	+	+	+
10	1	1.33	2.33	1.33	+	+	=	+	=	+
11	1	1.33	3	2	+	+	+	+	=	+
12	1	1.33	3	2	+	+	+	+	=	+
13	1	1	3	2.67	+	+	+	+	=	+
14	1	1	3	2	+	+	+	+	=	+
15	1	0.67	2	2	+	=	+	+	=	=

Histograms of the Likert scores for both conventional and experimental scans are shown in Figure 3.6. The scores for the three image types were combined to show the overall performance of conventional and experimental scans. Qualitative evaluation from the experimental scans (mostly 2 and 3) clearly outperformed that of the conventional scans (mostly 1).
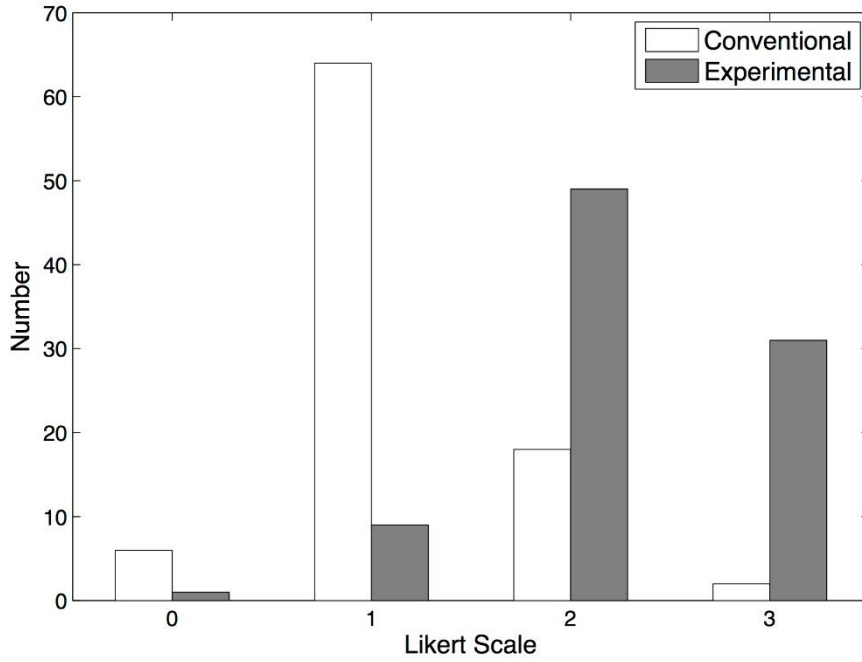
Figure 3.6 Histogram of all conventional and experimental scores combing the three image types. The statistics of conventional and experimental scans are 1.2±0.6 and 2.2±0.7, respectively.

3.4 Discussion

We have implemented a prospective under-sampling and constrained reconstruction scheme for high-resolution whole-brain DCE-MRI. We have performed a pilot comparison study in fifteen brain tumor patients that has demonstrated the strength of this technique and its potential impact on clinical DCE-MRI.

Specifically, we have shown that the DCE-MRI with constrained reconstruction is able to provide much higher spatio-temporal resolution and whole-brain spatial coverage compared to current DCE-MRI methods. This is extremely important when imaging large tumors or patients with multiple metastatic lesions, which the conventional scans fail to completely capture due to poor coverage and/or low spatial resolution. Within the same ROI of the conventional scan, Radiologists' reported improved quality, comparable or better diagnostic information in both anatomic images and K^{trans} maps of the experimental scan.

The experimental images show better SNR, resolution and lesion conspicuity, as well as overall image quality score, despite significant under-sampling. This is due to novelty in the way that raw data are reconstructed. In the conventional scan, each time frame is reconstructed independent of every other time frame. In the experimental scan, each time

frame is under-sampled in *k*-space, but all time frames are reconstructed in a single step and the mutual information between time points is leveraged through the use of temporal constraints. This is precisely the reason that compressed sensing and constrained reconstruction methods can achieve high acceleration factors with equivalent or superior image quality, despite under-sampling each time frame. In DCE-MRI (and similarly, time-resolved MR angiography) rapid temporal changes are limited to spatial positions containing vessels, and temporal changes elsewhere are smooth. This makes the images sparse after a temporal finite difference or high pass filter operator is applied. The experimental method leverages information from several time points, which boosts the effective signal-to-noise ratio and image quality, even at high acceleration rates. Regularization of this kind, with spatial and temporal constraints, is common in image and video de-noising applications not limited to MRI (83–85).

In a typical clinical protocol, conventional high-resolution whole-brain 3D T_1-weighted static image volumes were acquired before the GBCA injection and near the end of the exam, following all GBCA administration. It is worth noting that the first and last time frames of the experimental high-resolution whole-brain DCE scan also constitute pre- and post-contrast-enhanced T_1-weighted images. This could enable the experimental scan to take place of additional static pre- and post-contrast-enhance image acquisitions, saving scan resources and time.

There are several factors that preclude an optimal comparison with the conventional protocol. First, both conventional and experimental scans were performed in the same session with a relatively short interval. The rationale for this was practicality. Brain tumor patients were unwilling to come back on another day for a second MRI scan that was purely for research purposes. The consequence is that there is significant residual GBCA on board prior to the second DCE MRI scan, which could lead to underestimation of K^{trans} values in the second scan. The order of conventional and experimental scans was reversed in the last two cases; and the same K^{trans} underestimation was observed in the second scan, consistent with residual GBCA (not the imaging technique) being the cause. Additionally, due to the short interval between the two scans, tumors that take up contrast slowly may show higher conspicuity on the second scan due to temporal order (e.g. Figure (3.2), top row). A limitation of this study is that only two cases were performed with the experimental-then-conventional order. In both cases, the experimental (first) scan was rated as having higher tumor conspicuity than the conventional (second) scan, but this should be considered anecdotal because of the small sample size.

Another limiting factor for constrained reconstruction is the high computational complexity. Using a powerful workstation and an efficient MATLAB implementation, data reconstruction per dataset required 8 hours at the time the studies were performed. Since

then, we have been able to shorten the reconstruction time to 1.5 hours by incorporating coil compression (86), reduced temporal segmentation, and optimization of the MATLAB implementation. In general, reconstruction time is a limitation for iterative constrained reconstruction techniques, making them problematic for real-time imaging or applications that require immediate availability of image data. Parallelization, GPU based computation, and efficient C-based implementation are being explored by many groups, and these have provided reconstruction speedup on the order of 3 to 200 (52, 87).

This study did not include a quantitative assessment of spatial and contrast resolution, and this remains an important next step in the evaluation of constrained reconstruction techniques in DCE-MRI. Because the experimental method involves non-linear reconstruction, the definition of true spatial and contrast resolution is non-trivial and is an open research question. Partial solutions such as characterization of local point spread functions (88), and validation with digital or physical reference objects (89) exists but require dedicated investigation and are highly object-dependent. There are efforts underway to develop anatomically realistic brain DCE-MRI digital reference objects (90, 91), which will facilitate such work.

Under-sampling and constrained reconstruction for MRI is a rapidly developing area. Several groups, including ours, are developing constraints and quality evaluation techniques to maximize the reconstruction quality. The constraints used in this study have been previously validated in a retrospective study (56), and the prospective study results shown here further demonstrate the application and feasibility of constrained reconstruction for clinical DCE-MRI

3.5   Conclusion

We conclude that high-resolution whole-brain DCE-MRI using constrained reconstruction is clinically feasible and provides superior image quality compared to the current conventional DCE-MRI technique. In our study, the experimental approach provided superior image and pharmacokinetic map quality without compromising diagnostic information compared to the current DCE-MRI approach. The experimental approach also provided complete characterization of all normal and abnormal tissues, and allowed for arbitrary multi-planar reformatting of data. This was a significant advantage in two of the fifteen cases, one with a large glioblastoma multiforme that exceeded the spatial coverage of the conventional scan and had a narrow enhancing margin, the other with 14 metastatic lesions of which only 4 were characterized by the conventional scan. This study represents, to the best of our knowledge, the first prospective evaluation of brain DCE-MRI with constrained reconstruction. Compared to current best practices, this new

approach has the potential to vastly improve visualization and characterization of brain lesions with DCE-MRI.

Chapter 4. Model-based Direct Reconstruction for DCE-MRI

4.1 Introduction

As described in previous chapters, current DCE-MRI with Nyquist sampling is unable to simultaneously provide high spatio-temporal resolution and adequate volume coverage. Compressed sensing (44) and parallel imaging (17, 20) based schemes have been proposed to accelerate acquisition process, primarily to achieve better spatial resolution and coverage while maintaining the same temporal resolution. Notably, Lebel et al. (56) used a temporal high pass filter and multiple spatial sparsity constraints to achieve an undersampling rate (R) of 36x, and showed excellent quality of anatomic images in brain tumor cases. A recent pilot study in brain tumor patients indicated that this approach performs superior to conventional techniques with no apparent loss of diagnostic information (92). The works of Feng et al. (49), Chandarana et al. (93), Rosenkrantz et al. (52), used a golden-angle radial sampling pattern, compressed sensing, and parallel imaging to achieve a comparable acceleration rate of 19.1 to 28.7. These studies showed improved resolution and reduced motion sensitivity in breast, liver, and prostate DCE-MRI, compared to either parallel imaging alone or coil-by-coil compressed sensing alone. We will refer to these techniques as "indirect" methods, since the anatomic image series are reconstructed first, followed by a separate step for TK parameter fitting on a voxel-by-voxel basis.

In this chapter, we propose a framework for "direct" estimation of TK parameter maps from fully-sampled or undersampled (k,t)-space data. We employ a full forward model that converts the TK maps to (k,t)-space, and we pose the estimation of TK maps as an error minimization problem. Our approach is motivated by two factors: 1) spatial TK parameter maps have much lower dimensionality than those of dynamic image series (2-4 parameters, compared to 50-100 time points, per voxel), and 2) TK model-based reconstruction directly exploits what is known about contrast agent kinetics. These allow for robust parameter estimation from an information theoretic perspective, and has the potential to provide the most accurate restoration of TK parameter values, and allow for the highest acceleration.

Model-based direct reconstruction has been previously explored in other applications such as MRI relaxation parameter estimation (94–99), TK parameter estimation in PET (100–102), and TK parameter estimation in MRI (103, 104). Notably, for MRI relaxation parameter estimation, Sumpf et al. (97) used a model-based nonlinear inverse reconstruction to estimate T_2 maps from highly undersampled spin-echo MRI data; Zhao et al. (98) estimated T_1 parameters directly from undersampled MRI data with a sparsity constraint on the parameter maps. For dynamic PET imaging, Kamasak et al. (101) directly estimated TK parameter images from dynamic PET data using a kinetic model-based

reconstruction optimization; Lin et al. (102) used a sparsity constrained mixture model to estimate TK parameters from dynamic PET data, and evaluated with both simulated and experimental PET data.

For DCE MRI parameter mapping, Felsted et al. (103) proposed to use a model-based reconstruction algorithm to solve TK parameters directly from undersampled MRI k-space with a modified gradient descent algorithm. An undersampling factor of R=4 was demonstrated on simulated data; Dikaios et al. (104) proposed a Bayesian inference framework to directly estimate TK maps from undersampled MRI data, and achieved 8x acceleration in phantom and in-vivo prostate cancer data.

While the prior studies demonstrate promise, the full potential of TK model based reconstruction has lacked validation, both at higher undersampling rates, or with prospectively undersampled data from patients. In this study, we explore the maximum potential benefit of the direct TK estimation by testing very high undersampling rates. We validate the approach using retrospective undersampling of fully-sampled data and using prospectively undersampled DCE data sets from brain tumor patients. Compared to prior work, we are able to demonstrate much higher undersampling rates (up to 100×) in the retrospective study, using a more efficient gradient-based algorithm. We use quantitative evaluation (root Mean Square Error (rMSE) in TK parameters) to provide a systematic comparison against a state-of-the-art compressed sensing method that uses spatial and temporal sparsity constraints in 13 brain tumor patients. We also uniquely provide a prospective in-vivo study showing that whole-brain coverage with high spatial resolution can be achieved to capture complete pathological information. We demonstrate the potential of direct reconstruction to enable "parameter-free" reconstruction, when no sparsity constraints are added.

4.2   Theory

4.2.1   Direct TK Mapping

We propose to integrate TK modeling, specifically the Patlak model, into the image reconstruction process. Figure 4.1 illustrates the forward model that relates TK parameter maps to undersampled (k,t)-space.
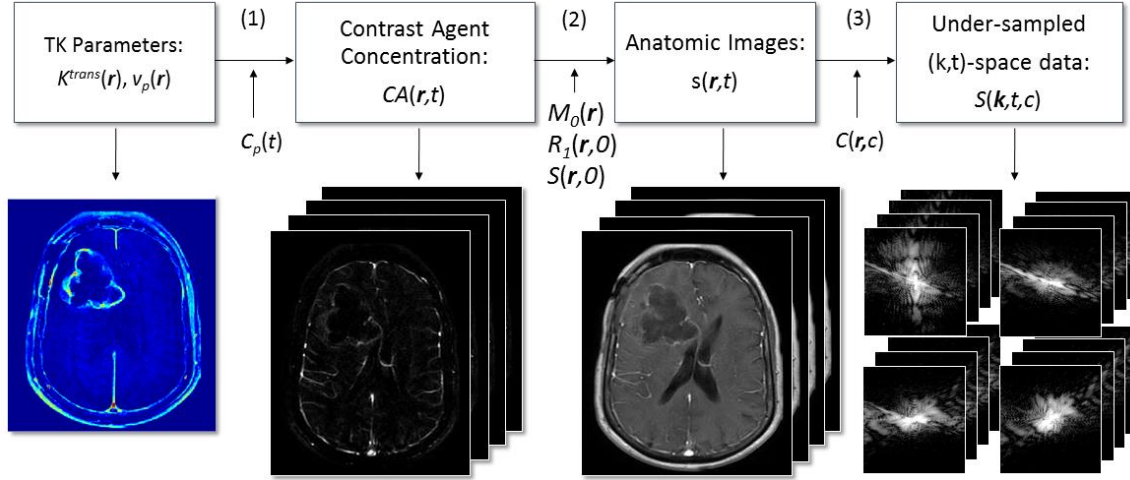
Figure 4.1 DCE-MRI forward model flowchart illustrating the conversion from TK parameter maps to undersampled (k,t)-space. Patlak model is used to convert TK parameter maps to contrast concentration over time, after which the T_1-weighted signal equation is used to obtain the dynamic anatomic images. Fourier transform, sensitivity maps and sampling pattern connect anatomic images to multi-coil (k,t)-space measurements.

We use the vector $\boldsymbol{r} \in (x,y,z)$ to represent image domain spatial coordinates, $\boldsymbol{k} \in (k_x, k_y, k_z)$ to represents k-space coordinates; t, c are the time and coil dimensions. The variables beneath the arrows of each step are known or pre-determined. The steps indicated (above the arrows) in Figure 4.1 are explained below:

1). Contrast agent concentration over time $CA(\boldsymbol{r},t)$ is assumed to follow the Patlak model:

$$CA(\boldsymbol{r},t) = K^{trans}(\boldsymbol{r}) \int_0^t C_p(\tau)\, d\tau + v_p(\boldsymbol{r}) C_p(t) \qquad (4.1)$$

where $C_p(t)$ is the arterial input function (AIF). In this work, we used a population-based AIF from (36). Notice that the AIF requires specifying a delay time. This is estimated from the k-space origin, which is acquired in every time frame, and has shown to accurately detect the time of contrast bolus arrival (105). We assume that the Patlak is appropriate for all voxels in the imaging volume. We have observed that image regions outside of vessels and tumor typically experience no enhancement during the DCE-MRI acquisition which results in a fit to v_p=0, K^{trans}=0.

2). Dynamic anatomic images $s(\boldsymbol{r},t)$ are related to $CA(\boldsymbol{r},t)$ by the steady state spoiled gradient echo (SPGR) signal equation:

$$s(r,t) = \frac{M_0(r)\sin\alpha(1-e^{-TR\cdot[R_1(r,0)+CA(r,t)\cdot r_1]})}{1-\cos\alpha e^{-TR\cdot[R_1(r,0)+CA(r,t)\cdot r_1]}} + \left[s(r,0) - \frac{M_0(r)\sin\alpha(1-e^{-TR\cdot R_1(r,0)})}{1-\cos\alpha e^{-TR\cdot R_1(r,0)}} \right] \quad (4.2)$$

where TR is the repetition time, α is the flip angle, r_1 is the contrast agent relaxivity, $R_1(r,0)$ and $M_0(r)$ are the pre-contrast R_1 (reciprocal of T_1) and the equilibrium longitudinal magnetization that are estimated from a T_1 mapping sequence. In this work, we used DESPOT1 (29) immediately prior to the DCE-MRI scan. $s(r,0)$ is the pre-contrast first-frame, which is fully-sampled in this work. The bracketed [] term resolves differences between the pre-contrast signal and the predicted pre-contrast signal based on the baseline T_1 and M_0 maps (from DESPOT1 sequences) (31).

3). The undersampled raw (k,t)-space data $S(k,t,c)$ is related to $s(r,t)$ by the coil sensitivities $C(r,c)$, and undersampling Fourier transform (F_u):

$$S(k,t,c) = F_u C(r,c)s(r,t) \quad (4.3)$$

In this work, $C(r,c)$ is estimated from time averaged data using the standard root sum-of-squares method (17). The image phase information is assumed to be captured by the complex-valued sensitivity maps.

Combining Equations 4.1-3, we reach a general function f to denote the relationship between TK maps $K^{trans}(r), v_p(r)$ and undersampled (k,t)-space $S(k,t,c)$.

$$S(k,t,c) = f(K^{trans}(r), v_p(r); C_p(t), TR, \alpha, R_1(r,0), M_0(r), r_1, C(r,c)) \quad (4.4)$$

where $C_p(t), TR, \alpha, R_1(r,0), M_0(r), r_1, C(r,c)$ are variables that are known or pre-determined as mentioned above. We solve for the unknown $K^{trans}(r)$, $v_p(r)$ via least-square optimization, formulated as follows:

$$(K^{trans}(r), v_p(r)) = \underset{K^{trans}(r), v_p(r)}{\arg\min} \| S(k,t,c) - f(K^{trans}(r), v_p(r)) \|_2^2 \quad (4.5)$$

This nonlinear optimization problem is solved by a quasi-Newton limited-memory Broyden-Fletcher-Goldfarb-Shannon (l-BFGS) method (106), where $K^{trans}(r)$ and $v_p(r)$ are solved alternatingly. The details of the optimization algorithm and gradient calculation are provided in Appendix 4-A.

Direct reconstruction by itself is "parameter-free". This is in contrast to compressed sensing based algorithms that require tuning of one or more regularization parameters. It is possible to incorporate additional spatial sparsity constraints on the TK maps themselves. In this work, we test the potential value of adding a spatial *'db2'* wavelet constraint (Ψ) to the parameter maps. The optimization problem with sparsity constraint is formulated as follows:

$$(K^{trans}(r), v_p(r)) = \underset{K^{trans}(r), v_p(r)}{\arg\min} \| S(k,t,c) - f(K^{trans}(r), v_p(r)) \|_2^2 + \lambda_1 \| \psi K^{trans}(r) \|_1 + \lambda_2 \| \psi v_p(r) \|_1$$

$$(4.6)$$

4.2.2 Indirect TK Mapping

Current state-of-the-art methods for highly accelerated DCE involve reconstructing intermediate images prior to TK modeling. These indirect methods are the most relevant alternatives to direct TK modeling and serve as a performance benchmark. A basic model for indirect reconstruction solves the minimization problem in Equation (4.7), where the final image, $s(r,t)$, remains consistent with acquired (k,t)-space data $S(k,t,c)$, yet is sparse in the temporal finite differences (V) domain and spatial wavelet domain (Ψ).

$$s(r,t) = \underset{s(r,t)}{\arg\min} \| S(k,t,c) - F_u C(r,c) s(r,t) \|_2^2 + \lambda_1 \| Vs(r,t) \|_1 + \lambda_2 \| \psi s(r,t) \|_1 \qquad (4.7)$$

The image is related to the acquired data using known coil sensitivities $C(r,c)$ and the undersampling Fourier transform F_u. TK modeling (e.g. using a Patlak model) is performed in a last step to estimate the spatial TK maps (e.g. $K^{trans}(r)$, $v_p(r)$) from $s(r,t)$. This optimization problem was solved by an efficient augmented Lagrangian method, alternating direction methods of multipliers (ADMM) (74), to get the anatomic images.

4.3　Methods

4.3.1　Digital Phantom

We simulated realistic DCE-MRI data using a digital phantom with known TK parameter maps and using the Patlak TK model. We used a process identical to Ref. (90), where the segmentation is extracted from patient data. Realistic sensitivity maps were used, and noise was added to each channel according to noise covariance matrix estimated from the patient data. A pre-contrast white-matter SNR level of 20 was chosen to mimic the SNR level in actual DCE data sets.

We retrospectively undersampled (k,t)-space with rates R of 20x to 100x. Ten noise realizations were generated for each R. Undersampling was in the k_x-k_y plane, simulating the k_y-k_z plane as in a prospectively undersampled 3D case, using a randomized golden-angle radial sampling pattern (53, 57). Detailed description and the videos of the undersampling strategies can be found in and the supporting materials. Direct and indirect methods were used to generate the TK parameters from both fully-sampled and undersampled data. TK map rMSE were computed over an ROI containing the entire tumor boundary.

4.3.2   In-Vivo Retrospective Evaluation

We reviewed 110 fully-sampled DCE-MRI raw data sets from patients with known or suspected brain tumor, receiving a routine brain MRI with contrast on a clinical 3T scanner (HDxt, GE Healthcare, Waukesha, WI). The data sets were from patients receiving routine brain MRI with contrast (including DCE-MRI) at our Institution, and the demographics reflect our local patient population. Our Institution follows standard exclusion criteria for MRI with Gadolinium-based contrast (107, 108) which includes: medically unstable, renal impairment, cardiac pacemaker, internal ferromagnetic device that is contraindicated for use in MRI, claustrophobia, and any other condition that would compromise the scan with reasonable safety. The retrospective study protocol was approved by our Institutional Review Board.

The sequence was based on a 3D Cartesian fast spoiled gradient echo sequence (SPGR) with FOV: $22 \times 22 \times 4.2 cm^3$, spatial resolution: $0.9 \times 1.3 \times 7.0 mm^3$, temporal resolution: 5s, 50 time frames, and 8 receiver coils. The flip angle is 15°, and TE is 1.3ms, TR is 6ms. DESPOT1 was performed before the DCE sequence, where three images with flip angle of 2°, 5°, 10° were acquired to estimate T_1 and M_0 maps before the contrast arrival. The contrast agent, Gadobenate dimeglumine (MultiHance Bracco Inc., which has relaxivity r_1 =4.39 $s^{-1}mM^{-1}$ at 37ºC at 3 Tesla (109)) was administered with a dose of 0.05 mMol/kg, followed by a 20 ml saline flush in the left arm by intravenous injection.

Of the 110 cases, we found 18 that had visible tumor larger than 1cm by bi-directional assessment. TK parameter maps K^{trans} and v_p were calculated from the fully-sampled images, and TK model fitting error was computed by taking the l_2 norm between the contrast concentration curves from fully-sampled images, $CA(\boldsymbol{r},t)$, and the fitted concentration curves generated from the TK parameter maps, $\hat{CA}(\boldsymbol{r},t)$. We then examined the Patlak modeling error, defined as:

$$\frac{\|\hat{CA}(\boldsymbol{r},t) - CA(\boldsymbol{r},t)\|_2^2}{\|CA(\boldsymbol{r},t)\|_2^2} \times 100\% \tag{4.8}$$

Of the 18 cases with visible tumor larger than 1cm, 13 cases had Patlak modelling error less than 1%, suggesting that the Patlak model with the population AIF was appropriate. The analysis below was performed on the 13 cases which were fully-sampled, had at least one tumor larger than 1cm, and for whom the Patlak model fitted the fully-sampled data with less than 1% error.

For each selected case, three sets of TK maps were generated from: 1) standard Fourier reconstruction of fully sampled data. These served as the gold standard reference maps. 2) Direct reconstruction method using retrospective undersampling; 3) Indirect reconstruction using retrospective undersampling. We examined R of 20× to 100×, with at increments of 20×. For each R, 10 realizations of the sampling pattern were generated using a different initial angle in the randomized golden-angle radial scheme. This effectively creates multiple noise realizations, since there is almost no overlap in the (k,t)-space sampling pattern (except for the one sample at the k-space origin, which is included in every sampling scheme at every undersampling factor).

For indirect method in Equation (4.7), the regularization parameters were empirically set as $\lambda_1=0.01$ and $\lambda_2=0.0001$. These values are motivated by empirical observations made on retrospective undersampling studies on a number of datasets (around 15) based on a criterion of achieving minimal rMSE between the reconstructed dynamic images from sub-sampled data and fully-sampled data. Both the regularizations were used in Equation (4.7), during experimental comparisons against the direct method with spatial sparsity constraint Equation (4.6). For direct method, regularization parameters were also empirically set as $\lambda_1=0.03$ and $\lambda_2=0.00001$. For fair comparison, when the direct method had no spatial wavelet constraint (Equation (4.5)), λ_2 in Equation (4.7) of the indirect method was set to 0.

The quantitative metric rMSE was computed on TK parameter maps, within a region-of-interest (ROI) containing enhancing tumor. Bland-Altman plots were generated using the difference of the reconstructed K^{trans} maps with respect to the fully-sampled K^{trans} maps within the ROI to test for any systematic bias.

A two-tailed paired STUDENT's t-test was performed based on the rMSE of the two methods in the 13 patients. The null hypothesis was equivalence of the two methods, with the null value being zero. The significance criterion was P value less than 0.05. The assumptions of normality were validated using Shapiro-Wilk test. Bonferroni correction

was applied to correct for multiple comparisons, that is, the significance level for each individual test was set to 0.05/13.

For one data set we applied spatial wavelet sparsity constraints for both methods (Equation (4.6) and Equation (4.7)) to demonstrate the feasibility and determine any possible improvement.

4.3.3   In-Vivo Prospective Evaluation

Prospectively undersampled data were acquired in 4 brain tumor patients (65 M, 71 M, 46 F, 22 F, all Glioblastoma) with Cartesian golden-angle radial k-space sampling (57, 92). 3D T_1-w SPGR data was acquired continuously for 5 minutes. Whole-brain coverage was achieved with a FOV of $22\times22\times20$ cm^3 and spatial resolution of $0.9\times0.9\times1.9$ mm^3. The prospective study protocol was approved by our Institutional Review Board. Written informed consent was provided by all participants.

Five second temporal resolution was achieved by grouping raw (k,t)-space data acquired within consecutive 5 sec intervals. This prospective acquisition undersampled each 5 sec temporal frame by 30×. Note that undersampling is not being used to shorten the scan time, but rather to significantly increase the spatial coverage and spatial resolution. For comparison, the standard clinical protocol at our institution that utilizes Nyquist sampling and 5 sec temporal resolution achieves FOV $22\times22\times4.2$cm^3 and spatial resolution $0.9\times1.3\times7.0$mm^3. For DCE-MRI, the scan time and temporal resolution is kept the same to capture dynamic changes during contrast arrival and wash-out.

Direct estimation of TK maps was performed using the proposed method. Three-plane and panning volume K^{trans} and v_p maps for the 4 data sets are presented for visual assessment. The first frame is necessary in the direct reconstruction process. A detailed description of how to obtain this frame, utilizing the properties of the golden-angle radial sampling pattern, can be found in the supporting materials. These prospectively undersampled DCE-MRI data were obtained 20 minutes after a standard-of-care conventional DCE-MRI scan, therefore there was some residual contrast on board.

4.4   Results

Figure 4.2 shows the convergence performance for the direct method at R=20. Objective function changes are plotted against iteration number, and final results where minimum gradient values reached are shown with different initial conditions. In the experiments, 140–180 iterations were needed to reach the stopping criteria. Convergence was achieved regardless of the initial condition. The reconstruction time for indirect and direct method

was 265s and 296s respectively on Linux workstation (24 core 2.5GHz, 192GB RAM). K^{trans} is reported in the units of min^{-1}, and v_p is reported as percent fraction.
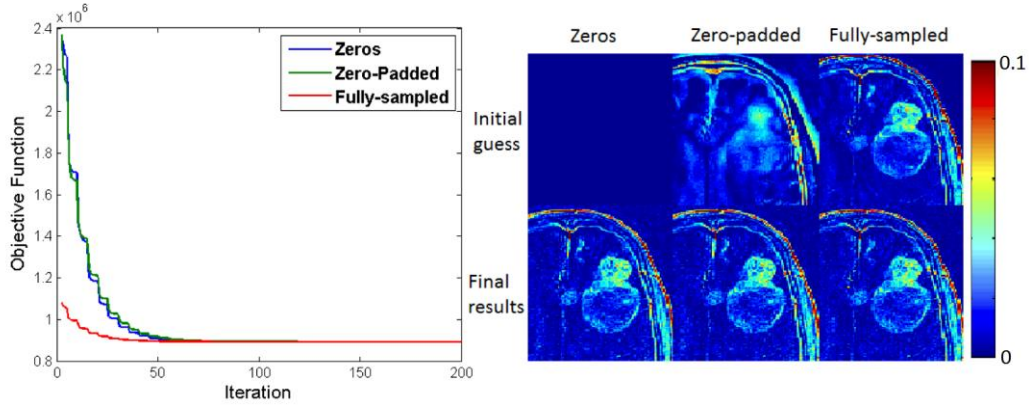

Figure 4.2 Objective function versus iteration number for three initial TK parameter estimates (left), and cropped portions of these initial and final TK maps (shown is the Ktrans map) at a undersampling rate of 20x (right). All initial conditions converged to the same solution. No benefit was observed using a zero-padded k-space relative to a null starting condition.

Figure 4.3 top shows the phantom results (cropped at the tumor part) of indirect and direct reconstruction of the K^{trans} and v_p maps at R=1 (fully-sampled data) and R=60 for both direct and indirect method. At R=1, it is shown that the direct method does not introduce additional error by enforcing the Patlak model into the reconstruction. At R=60, the direct method performs better than indirect method for both K^{trans} and v_p maps, overcoming the large errors and noise introduced by indirect method. Figure 4.3 bottom shows the rMSE (calculated in tumor boundary ROI) performance across different R. Across all R tested, the direct method outperformed indirect method at high undersampling rates.
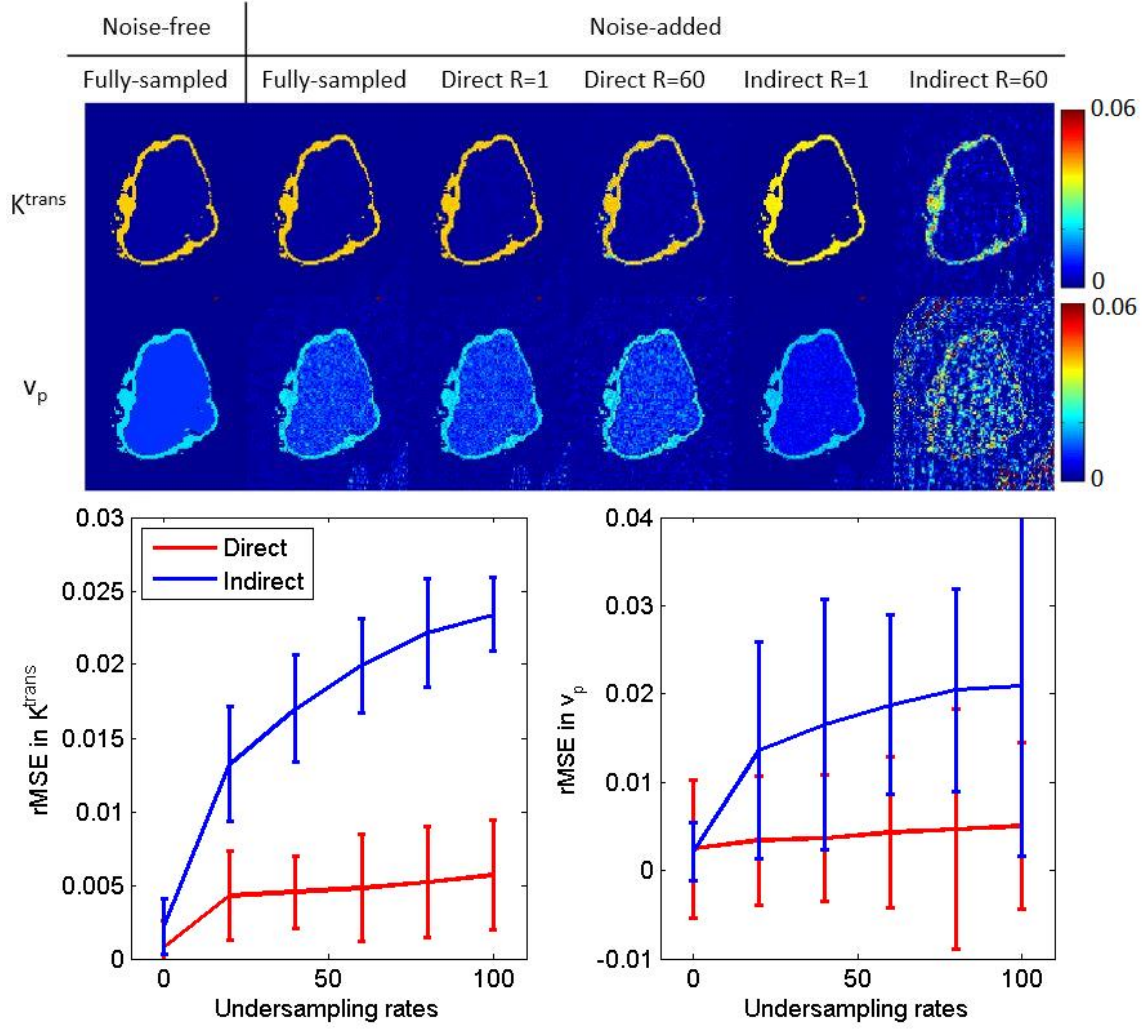
Figure 4.3 Retrospective evaluation of indirect and direct methods on phantom data. The top row contains ground truth K^{trans} and v_p maps that are used to generate the phantom, Patlak fitting results from fully-sampled but noise-added data, and R=1× and R=60× reconstruction results for both direct and indirect methods. Realistic noise (SNR=20) were added to the simulated k-space data. The bottom row contains rMSE across undersampling rates for a region of interest containing the entire tumor boundary (761 voxels). The proposed direct reconstruction produced lower mean rMSE at all sampling rates.

Figure 4.4 shows one representative example of the image results of direct and indirect reconstruction. K^{trans} and v_p maps of a glioblastoma patient at three different undersampling rates obtained from fully sampled data, the proposed direct reconstruction, and via indirect reconstruction are shown. Across all undersampling rates, the direct method qualitatively, and quantitatively depicted equal or more accurate restoration of TK parameter maps compared to indirect method. At R of 20× or less, the direct and indirect methods had equivalent performance. At higher undersampling rates, the indirect method failed to

capture critical tumor signals and tumor shapes in K^{trans} maps and small vessel information in v_p maps, while the direct method was able to provide accurate restoration. The results with spatial wavelet constraints (only 100× shown here) provide improved noise performance and image quality. It is also worth noting that the indirect method tends to underestimate K^{trans} values, while the direct method overcomes this underestimation. This is better observed in the Bland-Altman plots in Figure 4.6.
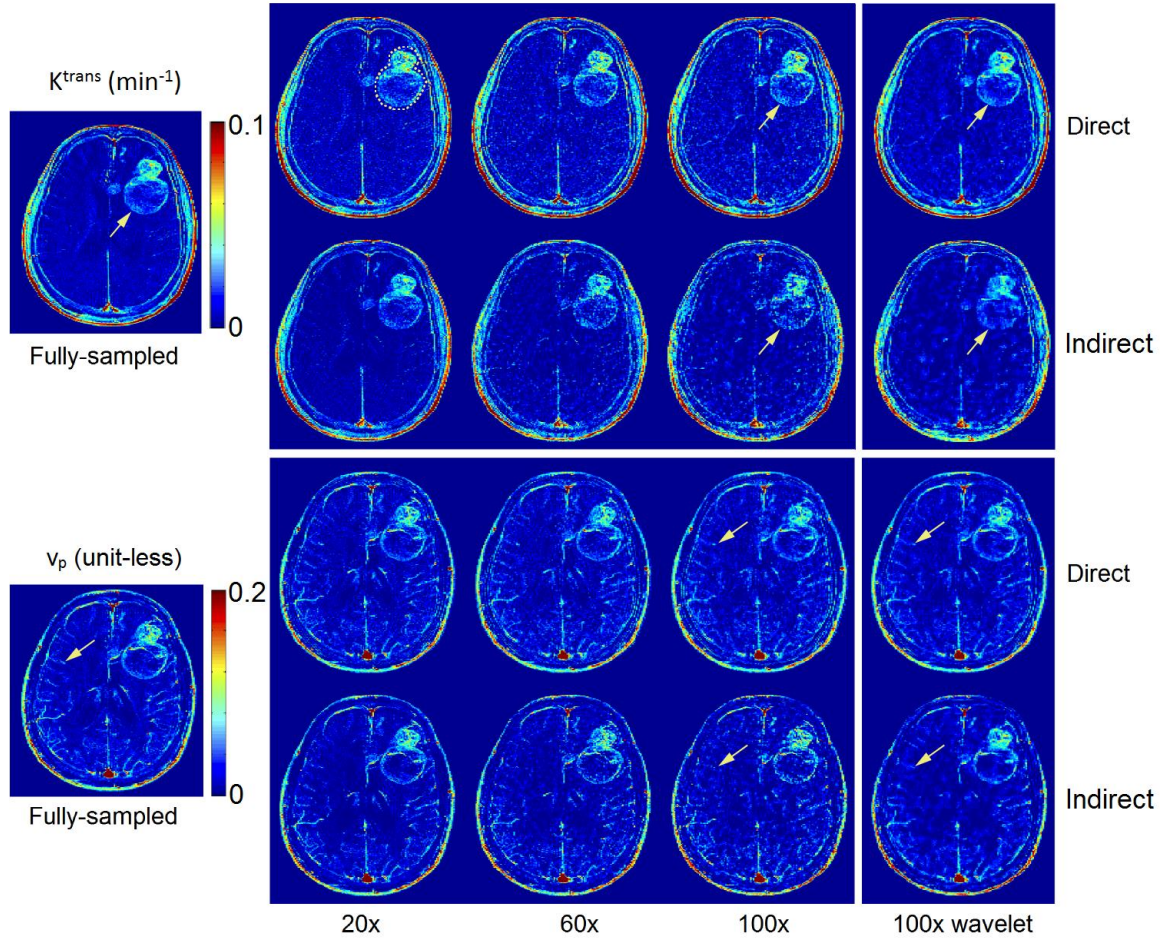

Figure 4.4 Retrospective evaluation of direct and indirect reconstruction of K^{trans} and v_p maps. Both reconstructions are shown without spatial wavelet sparsity constraints in the first three columns, and with the sparsity constraint in the last column. By visual inspection, direct reconstruction outperformed indirect results at all undersampling rates. The direct method provided superior delineation of the tumor boundary and other high resolution features in the K^{trans} maps than did the indirect method. This was particularly true at the highest undersampling rate (see arrows at 100×). For v_p maps, the direct method better preserved small vessel signals (see arrows at 100×) compared to the indirect method. Spatial wavelet constraints, shown on the rightmost column with 100×, provide additional noise suppression.

Figure 4.5 shows tumor ROI K^{trans} rMSE plots for both methods for a range of undersampling rates, and all 13 data sets that we used for retrospective evaluation. The error bars show the variance introduced by varying the initial angle of the sampling patterns. The direct method outperformed the indirect method for all the cases at high undersampling factors (>80×). The cases are ordered (left to right) by decreasing performance of direct reconstruction compared to indirect reconstruction. More detailed analysis can be found in .
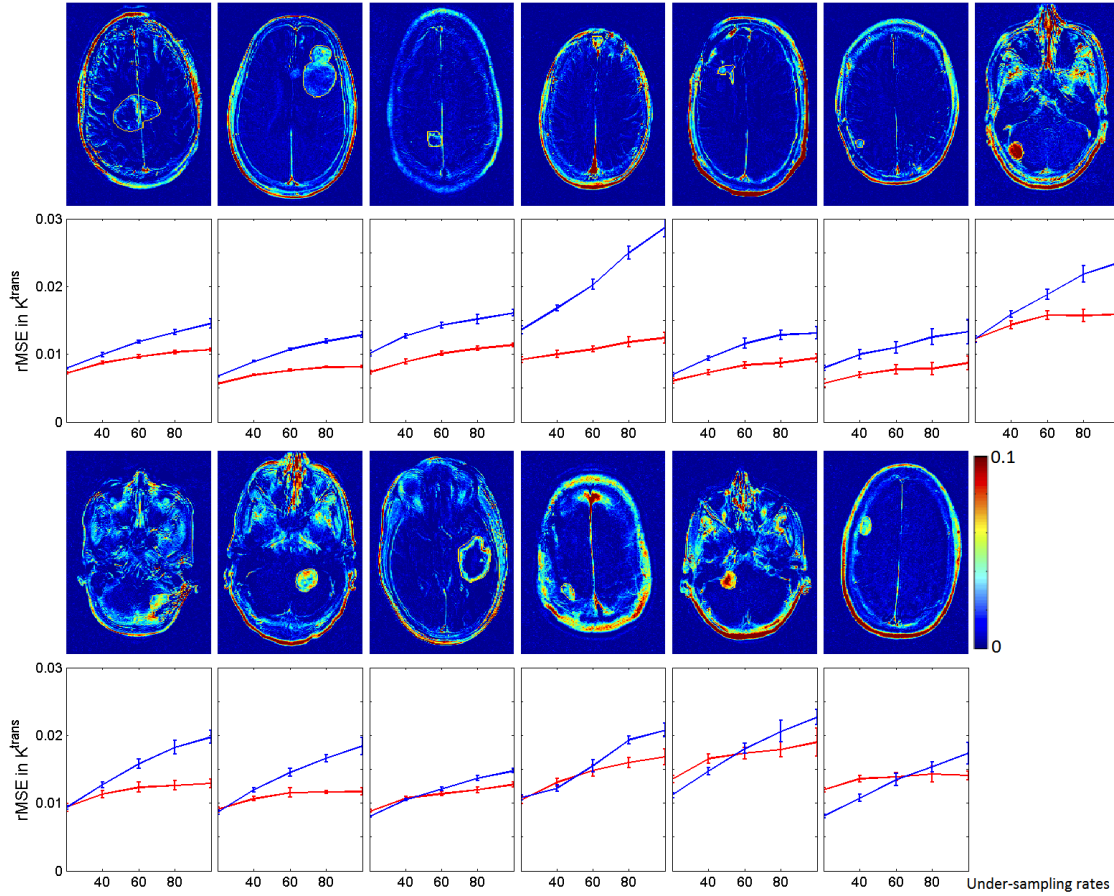

Figure 4.5 Tumor ROI (fully-sampled) and rMSE plot for direct and indirect reconstruction results across different R (20× to 100×) and 13 data sets for K^{trans} s values. The error bar indicate the mean and variance of the rMSE for each R where 10 different realization of sampling patterns were used. The direct method outperformed the indirect method in most cases, especially at R>60×. The variance for the two methods are comparable.

Figure 4.6 shows the Bland-Altman plots of direct and indirect methods for the K^{trans} values combining the ROIs of all the 13 cases. The indirect method tended to suppress

K^{trans} values smaller than 0.02 min^{-1}, and tended to underestimate values larger than 0.02 min^{-1}. This is similar to a soft-thresholding operation, and is illustrated by the green line in Figure 4.6. This may be a side-effect of the temporal finite difference constrained reconstruction that suppresses small temporal changes of concentration. Such a trend was not observed in the direct reconstruction, suggesting that tighter integration the TK model is able to identify and restore low K^{trans} values.
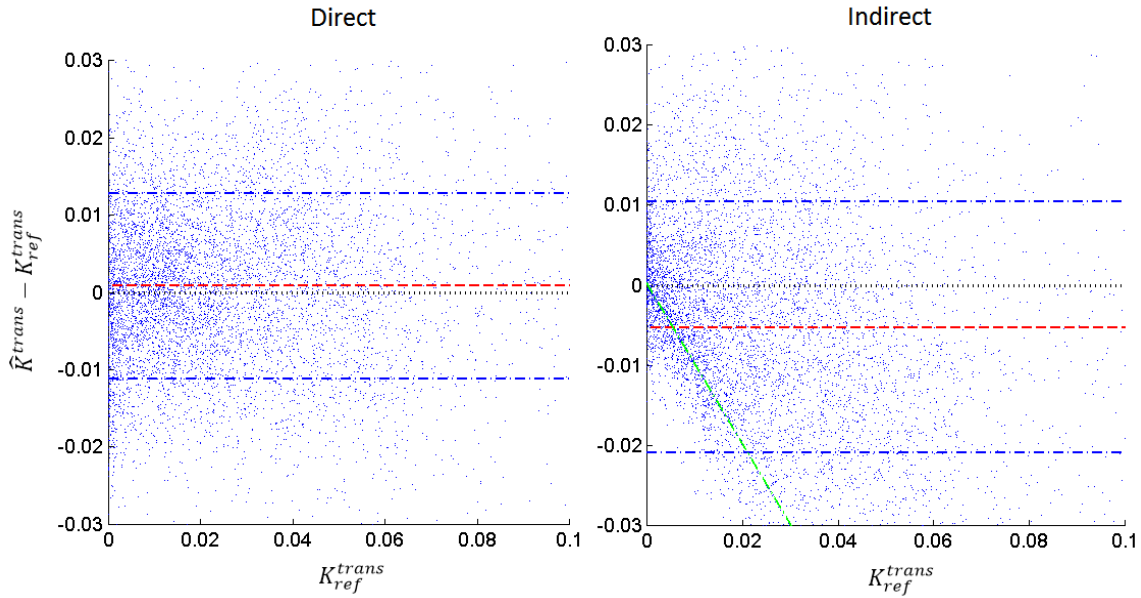

Figure 4.6 Bland-Altman plots of the difference between estimated K^{trans} and reference K^{trans} (from fully-sampled reconstruction) for both direct and indirect method at R=100x. Each dot corresponds to one voxel within the tumor ROI of one of the 13 cases. The indirect reconstruction (right) demonstrated a pattern of underestimating K^{trans} values, especially for $K^{trans} < 0.02$ min-1 (see green line). This may be a side-effect of the temporal finite difference constraint suppressing small concentration changes. In contrast, the direct reconstruction (left) did not demonstrate any considerable bias patterns, and had a lower variance.

Table 4.1 lists the patient demographic information, and the performance of direct and indirect methods at R=60×, evaluated by rMSE for both K^{trans} and v_p maps. The mean and standard deviation of rMSE are listed. The order of presentation in this table matches the order of Figure 6. The normality assumptions are met by Shapiro-Wilk test, and only 4 out of 56 cases (13 patients, 5 undersampling rates) reject the null hypothesis of composite normality assumption at significance level of 0.05. A two-tailed paired STUDENT's t-test was performed between the two methods based on rMSE of K^{trans}, and the last two columns show the smallest R where the direct method started to statistically significantly outperform

the indirect method (p<0.0038 after Bonferroni correction), and the corresponding p-value. The direct method was consistently better than indirect method across multiple data sets at high undersampling rates, and the difference was statistically significant at R>20× for 6 cases, R>40× for 3 cases, R>60× for 1 case, and R>80× for 3 cases.

Table 4.1 Patient demographic information and the rMSE performance (mean and standard diviations) of K^{trans} and v_p for direct and indirect methods at R=60×. The patient order is sorted as the direct reconstruction performance degraded (same as figure 6). At a significance level of p<0.05 (for individual case, p<0.0038 after Bonferroni correction), the direct method performed better than the indirect method for all the cases, with the cut-off undersampling rates varying between 20× to 80×. The p-value for the cut-off undersampling rate is shown in the last column.

No.	Age /Sex	Diagnosis	Indirect 60x		Direct 60x		Significant different at R>	p-value
			K^{trans} rMSE (×10e-4)	v_p rMSE (×10e-4)	K^{trans} rMSE (×10e-4)	v_p rMSE (×10e-4)		
1	75M	Meningioma	117±2.1	237±4.1	96±2.0	219±6.3	20x	$3.72×10^{-7}$
2	74M	Glioblastoma	107±2.0	250±6.2	76±1.2	188±4.2	20x	$6.3×10^{-9}$
3	73M	Glioma	120±3.8	305±9.5	99±3.2	258±9.4	20x	$2.55×10^{-8}$
4	69F	Meningioma	178±4.5	313±8.3	103±3.4	201±6.2	20x	$4.1×10^{-10}$
5	77M	Glioma	90±4.7	191±8.3	82±5.2	178±7.4	20x	$6.86×10^{-6}$
6	39F	Meningioma	114±5.0	192±10.5	83±4.7	191±8.2	20x	$1.75×10^{-6}$
7	54F	Glioma	167±5.1	358±14.5	156±4.4	376±17.3	40x	$2.41×10^{-6}$
8	44F	Meningioma	155±6.4	327±13.1	123±5.6	281±14.3	40x	$6.57×10^{-6}$
9	60M	Glioblastoma	130±5.0	306±10.2	113±5.5	261±10.1	40x	$9.73×10^{-7}$
10	38F	Glioma	134±5.4	457±6.8	129±5.3	424±6.2	60x	$7.42×10^{-5}$
11	63M	Meningioma	135±5.4	361±10.6	136±6.9	352±22.0	80x	$1.25×10^{-6}$
12	73F	Glioma	171±6.1	436±18.2	171±6.6	433±16.5	80x	$3.84×10^{-4}$
13	79F	Glioma	133±9.5	318±13.0	137±4.7	316±12.2	80x	$1.31×10^{-4}$

Figure 4.7 illustrates direct reconstruction of K^{trans} and v_p in two representative prospectively undersampled whole-brain DCE data sets. Panning videos TK maps for all 4 cases are provided in supporting materials. The whole-brain high-resolution TK maps enable visualization of the tumor on any arbitrary reformatted plane, providing a complete

depiction of the pathological information, and evaluation of narrow enhancing margin and small lesions. The reconstruction time was approximately 10 hours. This pilot study demonstrates the feasibility of applying direct TK parameter reconstruction to whole-brain DCE-MRI.

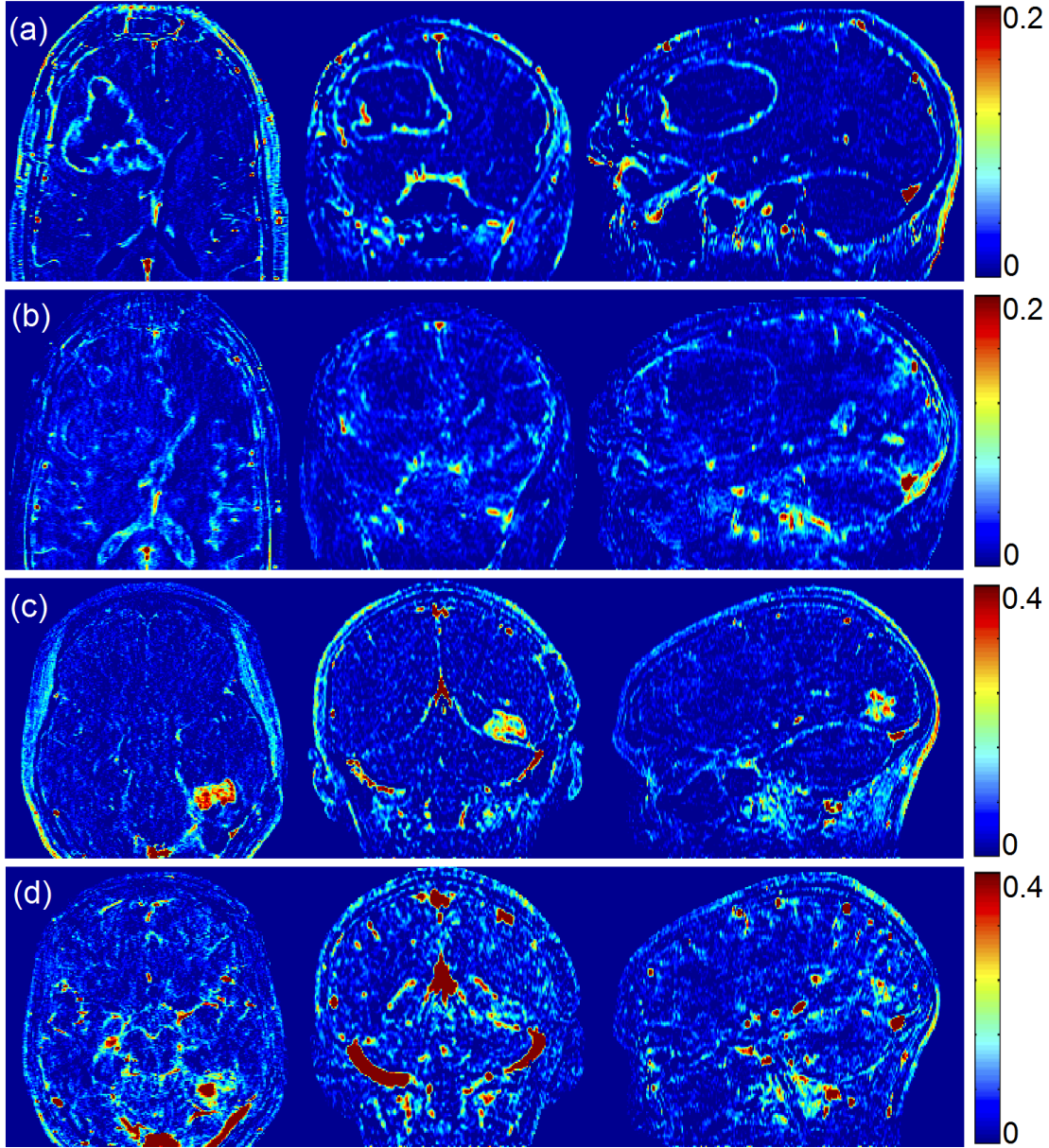**Figure 4.7** Direct reconstruction of K^{trans} ((a), (c)) and v_p ((b), (d)) maps from 2 representative prospectively undersampled data. Although lacking gold standard for the prospective studies, the direct reconstruction provided reasonable K^{trans} values and complete depiction of the entire tumor region. Panning-volume videos for all 4 cases are available in supplementary materials.

4.5   Discussion

We have presented a novel and potentially powerful TK parameter estimation scheme for DCE-MRI, where the TK parameter maps are directly reconstructed from undersampled (k,t)-space. By integrating the full forward model connecting the TK maps to the (k,t)-space data in the reconstruction, this method is able to provide excellent TK map fidelity at undersampling rates up to $100\times$. Higher rates were not tested. The forward model contained the analytic TK model along with specification of the AIF, coil sensitivity maps, and pre-contrast T_1, and M_0 maps obtained from pre-scans. The optimization has the flexibility to incorporate additional spatial sparsity constraints on the TK maps, as demonstrated with a spatial wavelet transform. In the retrospective study, this method outperformed an indirect reconstruction using parallel imaging and compressed sensing. We also uniquely demonstrated the use of this method for prospectively undersampled whole-brain DCE data, where whole-brain TK parameter maps can be produced with excellent image quality.

The proposed method is a "parameter-free" reconstruction, when no spatial constraints are applied to the TK maps. We demonstrated that by simply enforcing the TK model during reconstruction, performance is improved relative to a state-of-the-art compressed sensing reconstruction, without the need to select a constraint or to tune associated regularization parameters. It is straightforward to add sparsity constraints to the optimization problem as shown in Equation (4.7). Such constraints improve the noise performance, but at the expense of tuning regularization parameters. These constraints were found to improve convergence at very high undersampling rates ($>50\times$) where the TK map estimation problem becomes ill-posed.

The prospective study demonstrates that the proposed method can be used to achieve substantially higher spatial resolution and broader spatial coverage DCE-MRI, while maintaining the same temporal resolution and overall scan time. Although not studied in this work, this approach could potentially be used to improve the temporal resolution of DCE-MRI which is known to provide improvements in patient-specific AIF measurement and TK parameter precision (110).

The proposed method estimates the TK maps directly, and rather than reconstructing image time series as an intermediate step. This enables robust parameter estimation and easy-of-use in clinical application. Clinically, intermediate images (typically 50-100 volumes) are not always viewed. The extracted TK maps are of primary interest as they succinctly describe the behavior of the intermediate images. It is worth noting that the proposed method can provide intermediate images using the full forward model described in Figure 4.1. Figure 4.8 compares synthesized images from reconstructed TK maps against

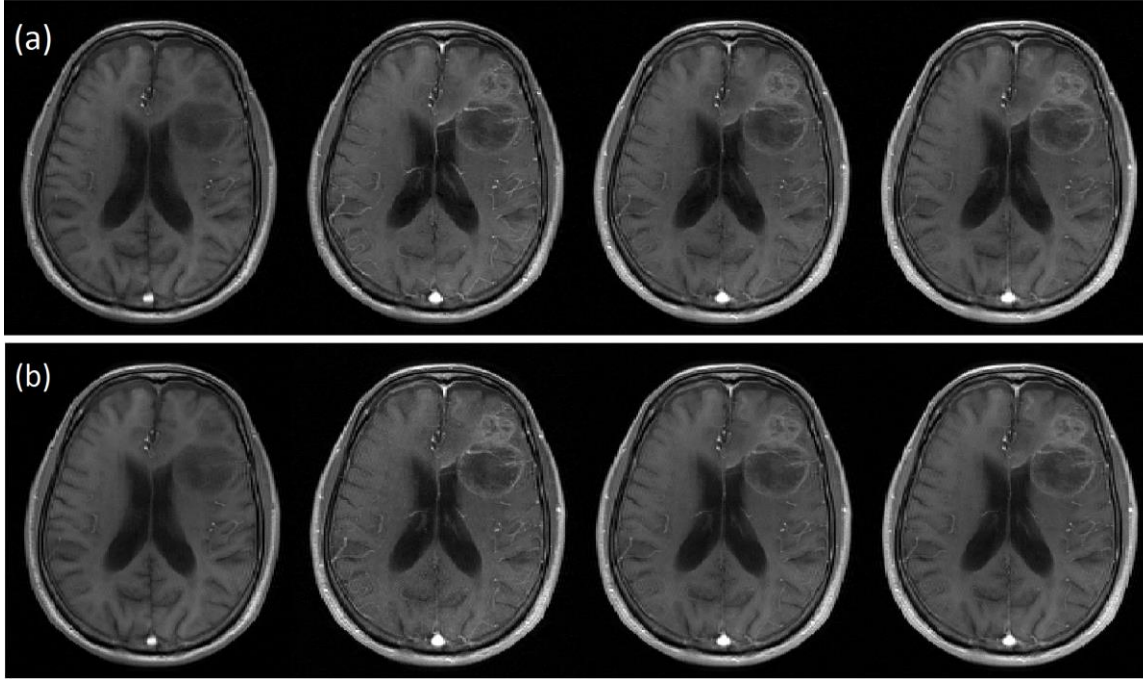fully-sampled anatomic images. The synthesized images show close resemblance to the fully-sampled images.

Figure 4.8 Illustration of intermediate anatomic images from fully-sampled (a), synthesized direct reconstruction at R=30× (b). Images from pre-, peak-, post-, and last-contrast arrival time points are shown from left to right. Anatomic images synthesized from direct estimation of TK parameter maps show similar quality to the fully-sampled and reconstructed anatomic images.

The proposed direct reconstruction scheme requires a-priori definition of the arterial input function (AIF). In this work, we used a population-based AIF, and the time-of-arrival was automatically detected as described in (105). However, other extensions which are blind to the choice of AIF could be explored. For instance, Fluckiger et al. (32) proposed a model-based blind estimation of both AIF and TK parameters from DCE images for fully-sampled data. This approach may be combined with ours to provide joint reconstruction of AIF and TK parameters directly from undersampled data.

This study has a few important limitations. First, we have thus far only demonstrated effectiveness of this approach using the Patlak model. Patlak was chosen because it is widely used and can be linearized and gradients can be readily computed. We also restricted the retrospective study to datasets that fit the Patlak model. It will be important to develop support for more sophisticated models, and utilize data that does not fit the presumed model to fully characterize failure modes. Use of more sophisticated models (e.g. extended Tofts model or 2-compartment exchange model) may fit the data better. Their

inclusion will make the reconstruction problem non-linear, and possibly non-convex. Gradient descent algorithms may not be applicable, as they require analytic solution for the first derivative of $CA(\boldsymbol{r},t)$ with respect to each TK parameter in the model (step 1 for Patlak model in Figure 1). Dikaois et al. (111) recently demonstrated the use of a Bayesian formulation of direct TK parameter estimation in DCE. The rationale was to use an optimal model for different tissue types. The additional complexity of more sophisticated models will necessitate longer reconstruction time, and convergence will require further investigation, and remains as future work.

A second limitation is that the tight integration of TK modeling in our reconstruction could be sensitive to data inconsistencies, such as patient motion. This is equally true for indirect reconstruction. Prospective motion compensation could be added to the proposed model but the complexities involved and efficacy have not been investigated here.

A third limitation is that the intermediate anatomic images are computed during the reconstruction and thus require a similar amount of memory and computation time as indirect methods. This approach is not currently solving the computational limitation of constrained reconstructions but rather provides a framework for improved image quality.

A fourth limitation is that T_1 and M_0 maps are required in the forward model, and were estimated using a separate multiple flip-angle sequence (DESPOT1) performed immediately prior to the DCE scan. Future work could include joint estimation of the pre-contrast T_1 maps and the TK maps, as suggested by Dickie et al. (112).

We compared the direct method with a state-of-the-art indirect method that utilized a temporal finite difference constraint. Compressed sensing techniques are expected to improve steadily as better constraints are identified (113–115); however, if used for TK parameter estimation, a TK model will be applied to the data and model inconsistencies introduced by the intermediate sparsity transforms are likely to propagate into the final parameter maps. Although untested, we hypothesize that our direct estimation method is likely to meet or exceed the image quality of any compressed sensing method.

Our proposed direct reconstruction scheme provides a method for highly accelerated DCE. Extremely high acceleration rates have been demonstrated (up to 100×), enabling full brain DCE with high spatial and temporal resolution. Our method is able to provide a parameter-free reconstruction and so avoids the empirical tuning required in other methods. This technique is easily extendable to DCE-MRI in other body parts such as the breasts, prostate, etc. Future work will include exploration of these additional clinical applications, optimization of data sampling schemes, and integration of more sophisticated TK models.

4.6 Conclusion

We have presented a novel and efficient reconstruction scheme to directly estimate TK parameter maps from highly undersampled DCE-MRI data. By comparison with a state-of-the-art indirect compressed sensing method, we demonstrate that the proposed direct approach provides improved TK map fidelity, and enables much higher acceleration. With the prospective study, this method is shown to be clinically feasible and provide high-quality whole-brain TK maps.

4.7 Appendix 4-A

The optimization problem in Equation (4.5) is solved alternatively by a quasi-Newton limited-memory Broyden-Fletcher-Goldfarb-Shanno (l-BFGS) method. That is, solving one while keeping the other fixed, as the pseudo codes indicated below:

Input initial guess $K^{trans}(\boldsymbol{r})^{(0)}$ $v_p(\boldsymbol{r})^{(0)}$

k=0, while "stopping criteria not met" do {

$$K^{trans}(\boldsymbol{r})^{(k+1)} = \underset{K^{trans}(\boldsymbol{r})}{\arg\min} \| S(\boldsymbol{k},t,c) - y(K^{rans}(\boldsymbol{r}),v_p(\boldsymbol{r})^{(k)}) \|_2^2$$

$$v_p(\boldsymbol{r})^{(k+1)} = \underset{v_p(\boldsymbol{r})}{\arg\min} \| S(\boldsymbol{k},t,c) - y(K^{trans}(\boldsymbol{r})^{(k+1)},v_p(\boldsymbol{r})) \|_2^2$$

k=k+1; }

The gradient of the cost function is evaluated analytically. This can be derived from the model and signal equations. For notational simplicity, the coordinate notations *r, k* and *c* are neglected (*t* is preserved to show the difference in dimension between TK parameter maps and dynamic images). For example, K^{trans} is for $K^{trans}(\boldsymbol{r})$ and $S(t)$ is for $S(\boldsymbol{k},t,c)$.

In Equation (4.5) we denote the cost function as:

$$y(K^{trans},v_p) = \| S(t) - f(K^{trans},v_p) \|_2^2 \tag{4.A1}$$

where for one iteration, v_p and all other known variables are kept constant, and we focus on deriving the gradient of y w.r.t. K^{trans}. We use the derivative chain rule:

$$\frac{\partial y}{\partial K^{trans}} = \frac{\partial CA(t)}{\partial K^{trans}} \frac{\partial s(t)}{\partial CA(t)} \frac{\partial y}{\partial s(t)} \tag{4.A2}$$

, where

$$\frac{\partial y}{\partial s(t)} = C^H F_u^H [k_u(t) - f(K^{trans}, v_p)] \tag{4.A3}$$

$$\frac{\partial s(t)}{\partial CA(t)} = r_1 M_0 \sin\alpha \frac{TR \cdot E_1 \cdot (1 - E_1 \cos\alpha) - (1 - E_1) \cdot TR \cdot E_1 \cos\alpha}{(1 - E_1 \cos\alpha)^2}, E_1 = e^{-TR \cdot R_1(t)} \tag{4.A4}$$

$$\frac{\partial CA(t)}{\partial K^{trans}} = \sum_{t=0}^{t=t_L} \left[\int_0^t C_p(\tau) d\tau \right] \tag{4.A5}$$

Sparsity-based constraints can be optionally applied to the TK maps as shown in Equation (4.7). In this study, we demonstrate the use of wavelet transform, and we denote the wavelet constrained part as $y_1 = \|\psi x\|_1$. For the evaluation of y_1, the l_1 norm is relaxed as in Ref (44):

$$\frac{\partial y_1(K^{trans})}{\partial K^{trans}} = \lambda_1 \psi^H W^{-1} \psi K^{trans} \tag{4.A6}$$

And the ith diagonal element of W is calculated as:

$$(W_i = \sqrt{(\psi K^{trans})_i^* \cdot (\psi K^{trans})_i + \mu}) \tag{4.A7}$$

where μ is a small relaxation parameter.
The gradient w.r.t. v_p is very similar:

$$\frac{\partial y}{\partial v_p} = \frac{\partial CA(t)}{\partial v_p} \frac{\partial s(t)}{\partial CA(t)} \frac{\partial y}{\partial s(t)} \tag{4.A8}$$

where all other parts are the same as above except:

$$\frac{\partial CA(t)}{\partial v_p} = C_p(t) \tag{4.A9}$$

Chapter 5. Joint Arterial Input Function and Tracker Kinetic Parameter Estimation from Under-Sampled DCE-MRI using a Model Consistency Constraint

5.1   Introduction

Dynamic contrast enhanced (DCE) MRI is a powerful technique for probing sub-voxel vascular properties of tissue including fractional plasma volume, fractional extracellular-extravascular volume, and clinically important transfer constants. DCE-MRI involves capturing a series of images before, during, and after administration of a T1-shortening contrast agent. Tracer-kinetic (TK) parameter maps are then computed from the dynamic images to provide information for diagnosis and monitoring treatment response (8, 22, 116). DCE-MRI is used throughout the body, however, in the brain, it has shown value in the assessment of brain tumor, multiple sclerosis, and Alzheimer disease (10, 26, 61).

With conventional Nyquist sampling, DCE-MRI is often unable to simultaneously provide adequate spatiotemporal resolution and spatial coverage. A typical brain DCE-MRI uses 5-10 second temporal resolution, which is a minimum requirement for accurate TK modeling (25, 35). Using Cartesian sampling at the Nyquist rate, only 5-10 slices are achievable. This is typically inadequate in large Glioblastoma cases, and cases with scattered metastatic disease that are often spread throughout the brain (92). Many techniques involving under-sampling and constrained reconstruction have been proposed to overcome this limitation. Earlier, compressed sensing and parallel imaging techniques have been used to reconstruct dynamic images from under-sampled data (49, 50, 56), and whole-brain or high-resolution TK maps can be fitted based on the reconstructed images (92, 93). Another approach is to utilize the TK modeling information to directly estimate TK parameters from under-sampled data. Such model-based reconstruction approaches have been explored in MRI relaxometry (97, 117), PET kinetic parameter estimation (100, 102), and recently, in DCE-MRI TK parameter estimation (103, 104, 118, 119). Compared to conventional compressed sensing techniques that reconstruct dynamic images first, the model-based approach for DCE-MRI reconstruction provides superior results and allows higher under-sampling rates (118, 119).

In conventional DCE-MRI, images are reconstructed for each time point. Patient-specific arterial input functions (AIF) can be identified from vessel pixels using either manual region of interest (ROI) selection or automatic cluster-based ROI selection (33). Some centers use a fixed population-averaged AIF (36), and institutionally-derived AIF, or a delay and dispersion corrected version of these (92). The use of patient-specific AIF (pat-AIF) is known to provide more accurate TK mapping (120). However, the estimation

of pat-AIF from under-sampled data is severely challenged by under-sampling artifacts. The current model-based TK reconstruction approaches therefore rely on population-averaged AIF (pop-AIF), which greatly limits its full potential.

In this work, we propose a novel DCE-MRI reconstruction approach, in which TK maps and dynamic images are simultaneously reconstructed, and TK model consistency is applied as a reconstruction constraint. Furthermore, this method allows for extraction of patient-specific AIFs, a key advantage compared to previous methods. This approach is inspired by recent works in accelerated quantitative MR relaxometry (121, 122), where physical or physiological model consistency was applied as a reconstruction constraint. This consistency constraint allowed for the data fit to deviate from the model, which made the scheme robust to scenarios with model inconsistencies (eg. presence of motion).

The DCE-MRI model consistency constraint requires a regularization parameter that balances the tradeoff between data consistency and model consistency. We show that the formulation allows for easy integration of different TK models and/or different TK solvers. The method is validated using an established physiologically-realistic brain tumor digital reference object and retrospectively under-sampled clinical brain-tumor DCE-MRI data. We also demonstrate its application to prospectively under-sampled high-resolution whole-brain DCE-MRI data.

5.2   Theory

5.2.1   Model Consistency Constraint

We jointly estimate contrast concentration vs time images (C) and TK parameter maps (θ) from the under-sampled data (y) by solving a least-squares problem:

$$(C,\theta) = \arg\min_{C,\theta} \| UFE(\psi C + S_0) - y \|_2^2 + \beta \| P(\theta) - C \|_2^2 \tag{5.1}$$

where Ψ is contrast concentration (C) to image difference (ΔS) conversion, S_0 is the fully-sampled pre-contrast image, U is the under-sampling mask, F is the Fourier transform, E is the sensitivity encoding, and P represents the forward TK modeling (linear for Patlak, nonlinear for all other TK models). This formulation can be simplified to:

$$(C,\theta) = \arg\min_{C,\theta} \| AC - b \|_2^2 + \beta \| P(\theta) - C \|_2^2 \tag{5.2}$$

where $A=UFE\Psi$, $b=(y+UFES_0)$ is the known data.

To solve the least-square optimization problem in Equation (5.2), we alternatively solve for each variable while keeping others constant. For each iteration n:

$$C^{n+1} = \arg\min_{C} \| AC - b \|_2^2 + \beta \| P(\theta^n) - C \|_2^2 \tag{5.3}$$

$$\theta^{n+1} = P^{-1}(C^{n+1}) \tag{5.4}$$

Note that Equation (5.3) is regularized SENSE reconstruction with an l_2 norm constraint that can be solved efficiently using conjugate gradients (CG) (30). Equation (5.4) is backward TK modeling that can be solved using any DCE-MRI modeling toolbox. Because forward modeling (P) and backward modeling (P^{-1}) are used iteratively, the modeling solver should not utilize linearization or other forms of approximation. For example, Rocketship (123) and TOPPCAT(124) are two suitable solvers. Detailed sub-steps and variants of Equation (5.3) and (5.4) can be found in Appendix I.

5.2.2   Joint AIF and TK Parameter Estimation

The proposed formulation allows for joint estimation of the patient-specific AIF. Equation (5.2) can be modified to estimate C, θ and AIF from under-sampled data by solving the following least-squares problem:

$$(C, \theta, AIF) = \arg\min_{C, \theta, AIF} \| AC - b \|_2^2 + \beta \| P(\theta, AIF) - C \|_2^2 \tag{5.5}$$

Similar to the above, we solve each variable alternatively as follows (n^{th} iteration):

$$C^{n+1} = \arg\min_{C} \| AC - b \|_2^2 + \beta \| P(\theta^n, AIF^n) - C \|_2^2 \tag{5.6}$$

$$\theta^{n+1}, AIF^n = P^{-1}(C^{n+1}) \tag{5.7}$$

Equation (5.7) is backward TK modeling from contrast concentration including pat-AIF estimation. This can be performed by identifying an arterial ROI once, using the time-averaged image or post-contrast image. Within each iteration, it is then possible to: 1) apply this ROI to C to estimate the AIF (averaging the pixels), and 2) use the updated AIF during TK modeling. This is a common procedure in TK modeling for DCE-MRI. The only difference is identification of the arterial ROI prior to the reconstruction of the dynamic images.

5.2.3   Theoretical Benefits

The proposed method formulates model consistency as a constraint with a penalty β, and decouples it from data consistency. There are multiple benefits of this formulation: 1. algorithm complexity is greatly reduced compared to recently proposed direct reconstruction techniques that require complex gradient evaluations (103, 111, 118); 2.

different TK models can easily be included in this formulation, as described above; 3. patient-specific AIFs can be estimated jointly with TK maps, as described above; and 4. the penalty β can allow for TK model deviation, reducing errors that may be caused by strict model enforcement (122). This work specifically demonstrates #2 and #3.

5.3 Methods

5.3.1 Data Sources

Digital Reference Object: Anatomically-realistic brain tumor DCE-MRI digital reference object (DRO) was generated based on the method and data provided by Bosca and Jackson (125). The Extended-Tofts (eTofts) model was used to generate contrast concentration curves with known TK parameter maps and pop-AIF (36). Coil sensitivity maps measured on our MRI scanner (3T, 8-channel head coil) were co-registered to the DRO and used to generate realistic MRI k-space data.

Retrospective: Nine fully-sampled brain tumor DCE-MRI data sets were acquired from patients receiving routine brain MRI with contrast (including DCE-MRI) at our Institution. The study protocol was approved by our Institutional Review Board. The acquisition was based on a 3D Cartesian fast spoiled gradient echo sequence (SPGR) with FOV: $22\times22\times4.2cm^3$, spatial resolution: $0.9\times1.3\times7.0mm^3$, temporal resolution: 5s, 50 time frames, and 8 receiver coils. The flip angle was 15°, and TE was 1.3ms, TR was 6ms. DESPOT1 was performed prior DCE-MRI, with flip angle of 2°, 5°, 10° to estimate pre-contrast T_1 and M_0 maps. The contrast agent, Gadobenate dimeglumine (MultiHance Bracco Inc., relaxivity r_1=4.39 s-1mM-1 at 37ºC at 3 Tesla (109)) was administered with a dose of 0.05 mMol/kg, followed by a 20 ml saline flush in the left arm by intravenous injection.

Prospective: Prospectively under-sampled data were acquired in one brain tumor patient (65 M, Glioblastoma) with Cartesian golden-angle radial k-space sampling (57, 92). 3D SPGR data was acquired continuously for 5 minutes. Whole-brain coverage was achieved with a FOV of $22\times22\times20$ cm^3 and spatial resolution of $0.9\times0.9\times1.9$ mm^3. The prospective study protocol was approved by our Institutional Review Board. Written informed consent was provided by the participant.

5.3.2 Demonstration of TK Solver Flexibility

To demonstrate TK solver flexibility, DRO data was retrospectively under-sampled using a randomized golden-angle sampling pattern at R=20× (57). The proposed method with eTofts modeling was used to reconstruct TK parameter maps at R=1× (fully-sampled) and R=20×. An in-house gradient-based algorithm and an open-source TK modelling toolbox, Rocketship (123), were used for the eTofts solver in the proposed algorithm (Equation (5.4)). Tumor ROI rMSE for the K^{trans} maps were calculated for evaluation.

5.3.3 Demonstration of TK Model Flexibility

The nine fully-sampled patient data were fitted to both Patlak and eTofts model to calculate model fitting error, and F-test was performed in the tumor ROI to determine whether Patlak or eTofts model is an appropriate fit (39). If more than 50% of the tumor pixels were appropriately fitted for certain model, this model was selected for the data set. We reconstructed the corresponding TK parameter maps for fully-sampled data (used as reference) and at under-sampling rates of 20×, 60× and 100× for all 10 cases. A randomized golden-angle sampling pattern (57) was used in the k_x-k_y plane, simulating k_y-k_z phase encoding in a 3D whole-brain acquisition. Images were reconstructed using a pop-AIF (36) with patient-specific delay corrected by the delay estimated from k-space center (105). ROI-based K^{trans} rMSE and K^{trans} histograms were calculated based on the reference K^{trans} maps. K^{trans} histogram skewness and 90% percentile K^{trans} values were measured for evaluation (66, 126).

5.3.4 Demonstration of Joint AIF and TK estimation

The cases following Patlak model were reviewed with special attention to vessel signal. Cases that showed significant pre-contrast inflow enhancement were identified and subsequently excluded. With the remaining cases, we performed joint estimation of AIF and Patlak parameter maps from under-sampled data across sampling rates of 20×, 60×, and 100×. For each under-sampling rate, 15 realizations were generated by varying the initial angle of the golden-angle radial sampling pattern (57). Reconstructed patient-specific AIFs were compared to the fully-sampled reference using rMSE and bolus peak difference. ROI-based K^{trans} relative rMSE (normalized by reference 90% percentile K^{trans}) were also calculated for evaluation.

5.3.5   Demonstration with Prospectively Undersampled Data

We demonstrate application of the proposed method for joint AIF and TK parameter estimation on prospectively 30x undersampled high-resolution whole-brain DCE-MRI data. Five second temporal resolution was achieved by grouping raw (k,t)-space data acquired within consecutive 5 sec intervals, effectively $30\times$ under-sampling compared to Nyquist sampling (127). Patient-specific AIF and TK maps were jointly reconstructed using the proposed model consistency constraint approach. Pat-AIF ROI was selected based on time-averaged images. Three-plane of K^{trans} and v_p maps and pat-AIF are presented for visual assessment.

5.4   Results

Figure 5.1 shows the reconstruction results of the DRO at R=1× and R=20×. E-tofts model was used to generate the simulated DCE-MRI data, and also for model-based reconstruction. Empirical β value and iteration number were chosen. Computation time for the conversion from concentration vs time to TK maps, was 3.44s for the in-house gradient-based method, and 31.62s for Rocketship with parallel computing turned on (4 workers). At R=1×, by comparing to the true TK values that are used to generate the phantom, both gradient-based method and Rocketship were able to restore accurate TK maps. AT R=20×, both methods were able to restore good-quality K^{trans} and v_p maps, with slightly degraded K_{ep} maps because of the nonlinearity of the K_{ep} parameter. The proposed method provides better rMSE performance for K^{trans} maps. These results shows that the proposed method is compatible with a third-party solver.
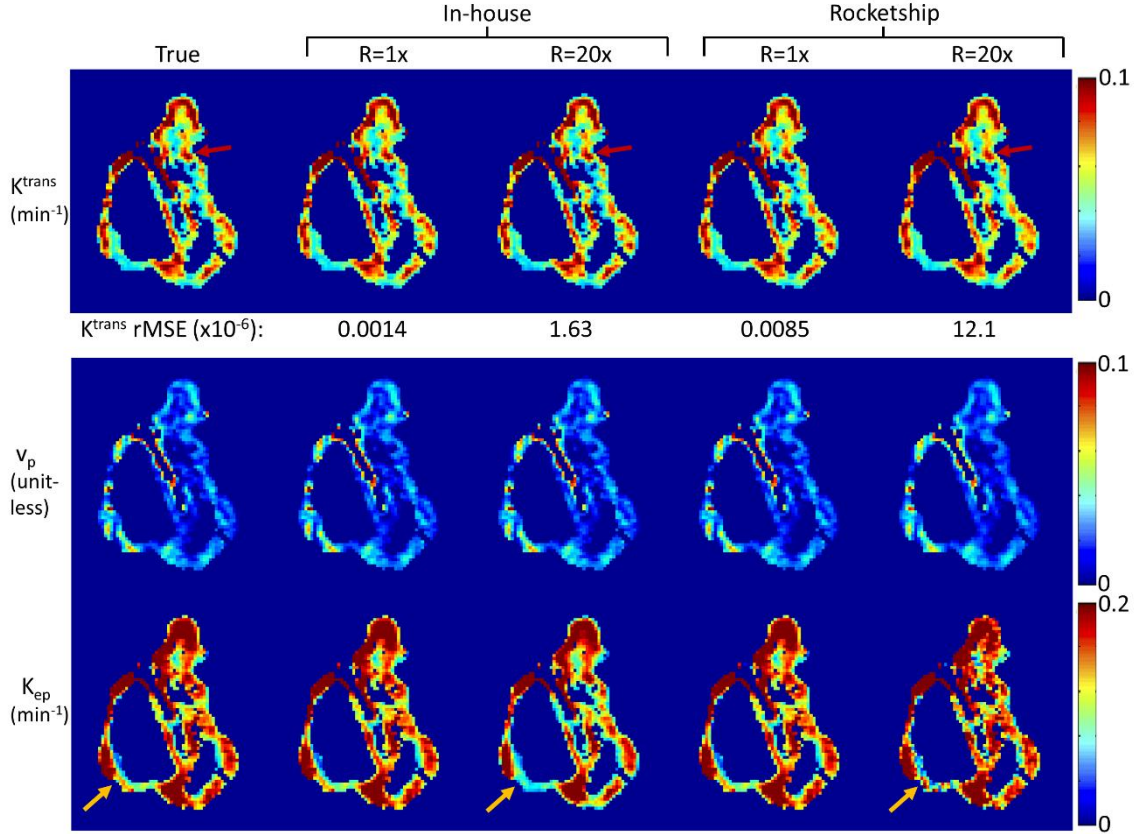
Figure 5.1 The proposed method is compatible with third-party TK solvers. Shown are results using an in-house gradient-based solver and the Rocketship solver, both using the model consistency constraint method on an anatomically-realistic brain-tumor DCE-MRI digital reference object. At R=1x (fully-sampled), both methods are able to restore TK maps accurately. At R=20x, both methods were able to restore good-quality K^{trans} and v_p maps, with slightly degraded K_{ep} maps. The gradient-based method provides better results in terms of K^{trans} rMSE in less computation time.

Figure 5.2 illustrates the impact of regularization parameter β for one representative in-vivo brain tumor dataset, using the Patlak model, at R=20x. The cost function values as a function of iteration number, l-curve, and the final reconstructed TK maps are plotted for different β values. A large β resulted in slow convergence, while a smaller β provided fast convergence. This behavior is expected as ill-conditioning of the problem in Equation (5.3) increases with β (128). TK maps obtained with a large β show poor fidelity as data consistency is violated, while the maps with a small β is equivalent to a SENSE reconstruction without constraints, and demonstrated g-factor related artifacts at R=20×. The L-curve shows the balance between the data consistency and model consistency, based on which the β values in the range of 0.1 to 1 (green highlighted) show similar performance. We then tune the β value in this range for different cases. We found the acceptable range

to be roughly 1 order of magnitude, and consistent among the 4 cases that we carefully examined. This suggests that the parameter could be standardized.
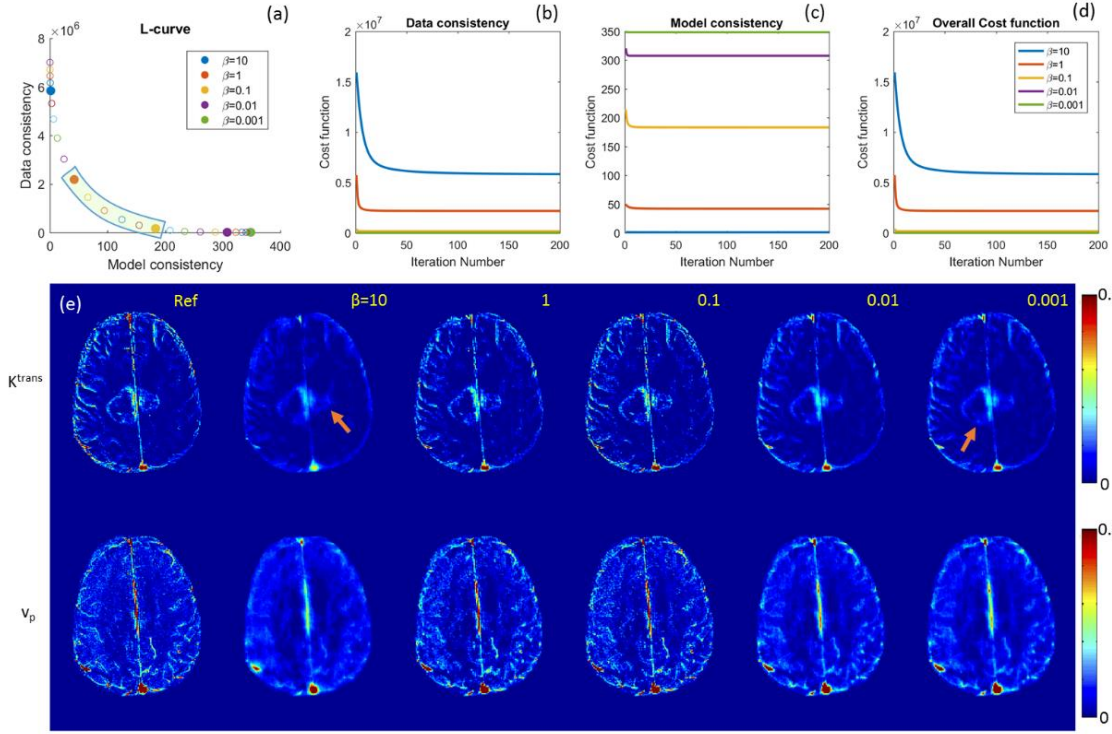

Figure 5.2 Performance for different β values at R=20×. (a) The l-curve shows that β value controls the balance between model and data consistency. (b, c, d) Convergence of the cost function to within 1% of its final value required 116, 24, 10, 4, and 2 iterations for β values of 10, 1, 0.1, 0.01, and 0.001, respectively. (e) Tumor ROI rMSE (K^{trans}) are 9.1, 6.5, 6.4, 8.7, 9.3 (x10^{-3}) respectively for β value of 10, 1, 0.1, 0.01, 0.001. Reconstruction with small β values converged quickly, and is closer to a SENSE reconstruction with associated g-factor losses and undersampling artifacts. Reconstruction with large β values shows slow convergence, and provides inaccurate TK maps since the data consistency is violated.

Based on the tumor ROI F-test, the Patlak model was appropriate for 6 cases, while the e-Tofts model was appropriate for 3 cases. Figure 3 shows two representative cases of Patlak and eTofts model at R=60× and R=100×. K^{trans} and v_p maps on the zoomed-in tumor region are shown (K_{ep} for eTofts is not shown). Based on the K^{trans} rMSE and histograms, the proposed method is able to restore good quality TK parameter maps at under-sampling rates up to 100×, including for the nonlinear eTofts model.
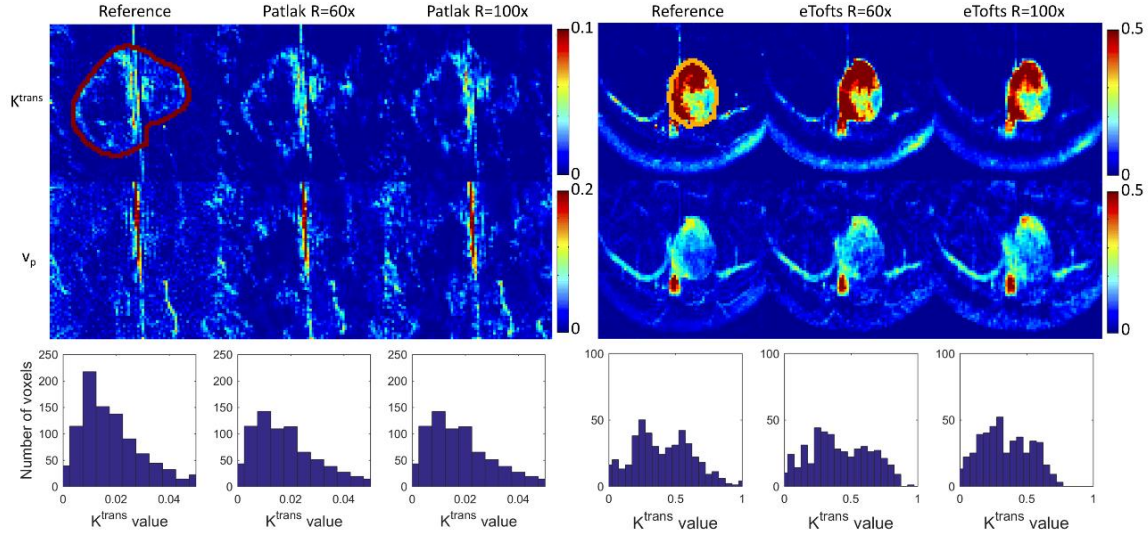
Figure 5.3 Reconstruction of the TK maps of two representative case for Patlak and eTofts model at R=60× and 100×. Tumor ROI (indicated in the reference images) histogram were shown below the respective cases. Quantitative evaluation across all the cases were shown in figure 4. Judging by the histogram and rMSE, the proposed method was able to restore good-quality TK maps at a high under-sampling rate of 100× for both Patlak and eTofts model.

Figure 5.4 shows quantitative evaluation of the reconstruction results focusing on K^{trans} values. For Patlak model reconstruction, the 90 percentile K^{trans} values match well with the reference values across all cases, the histogram skewness are also reasonably matched, and tumor ROI rMSE is almost 0.023 for all cases and under-sampling rates. For eTofts mode, the 90 percentile K^{trans} matched well with reference for one case, and have larger deviation for other cases at R=100×. The maximum rMSE value were at most 0.073.
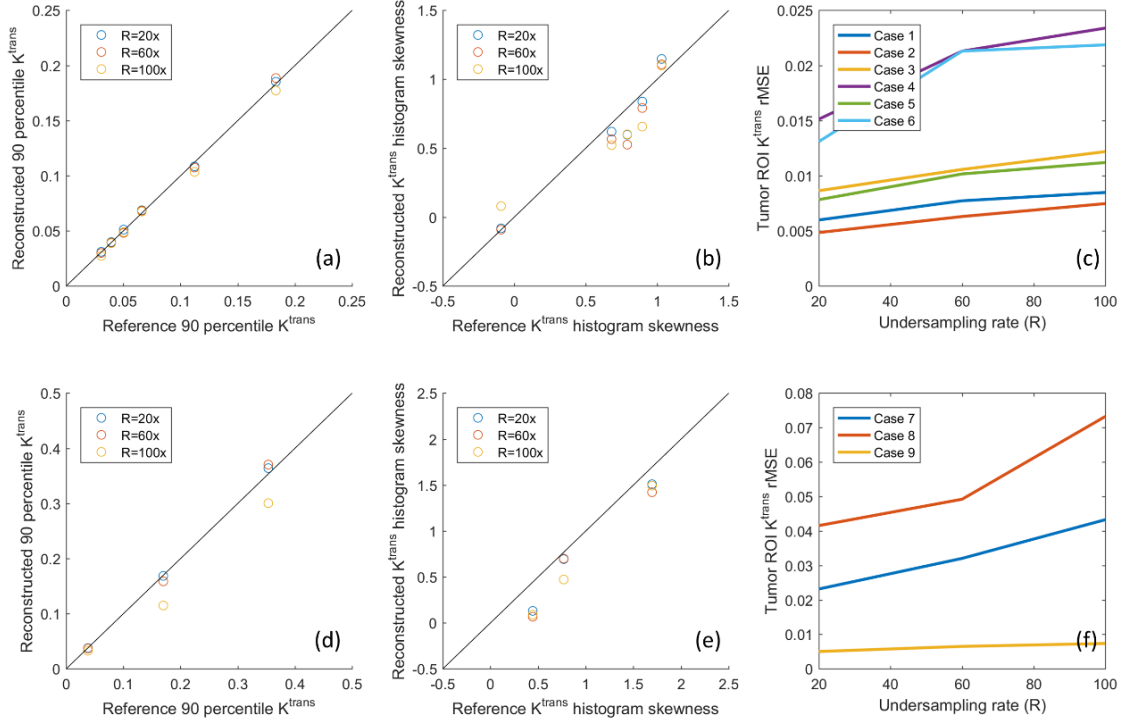
Figure 5.4 Quantitative evaluation of Patlak (top row) and eTofts (bottow row) reconstruction. 90 percentile of the reconstructed K^{trans} values for different cases were plotted against the reference 90 percentile K^{trans}. For Patlak model the values matched well for all cases and under-sampling rates (a). For eTofts model the values matched well for R=20× and 60×, and have larger deviation for R=100× (d). The K^{trans} histogram skewness were also plotted against the reference histogram skewness (b), (e). The tumor ROI K^{trans} rMSE were plotted against different R's across different cases, and rMSE is at most 0.023 for Patlak reconstruction (c) and 0.073 for eTofts reconstruction (f).

Figure 5.5 shows the selection of AIF ROI from under-sampled data, and the comparison of pop-AIF and pat-AIF, and the resulting TK maps. It is known that pop-AIF may not represent patient specific characteristics, and the difference in pop-AIF and pat-AIF can lead to significant errors in the resulting TK maps.
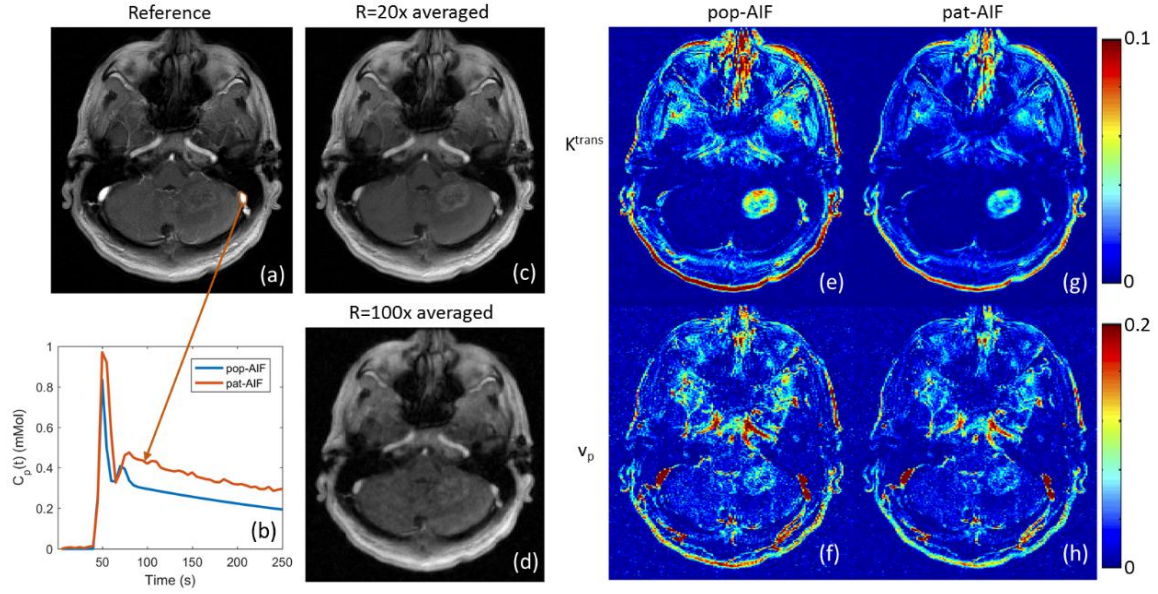
Figure 5.5 Left: Extraction of pat-AIF (b) from a manually selected ROI on the peak contrast frame of fully-sampled images (a). The pop-AIF show in (b) was delay and amplitude corrected. In under-sampling scenario, a time averaged image can be generated (c), and even at R=100× (d), it is straightforward to select an artery ROI from this image for the joint AIF and TK maps reconstruction. Right: Different AIFs can result in different TK maps (e, f, g, h), and pat-AIF is preferred for more accurate TK modeling.

Figure 5.6 shows the reconstruction results of TK maps and pat-AIF (same case in figure 5) at different under-sampling rates. Comparing to the AIF extracted from fully-sampled data, the proposed method is able to restore accurate AIF up to R=100×, with good-quality TK maps restored at the same time.
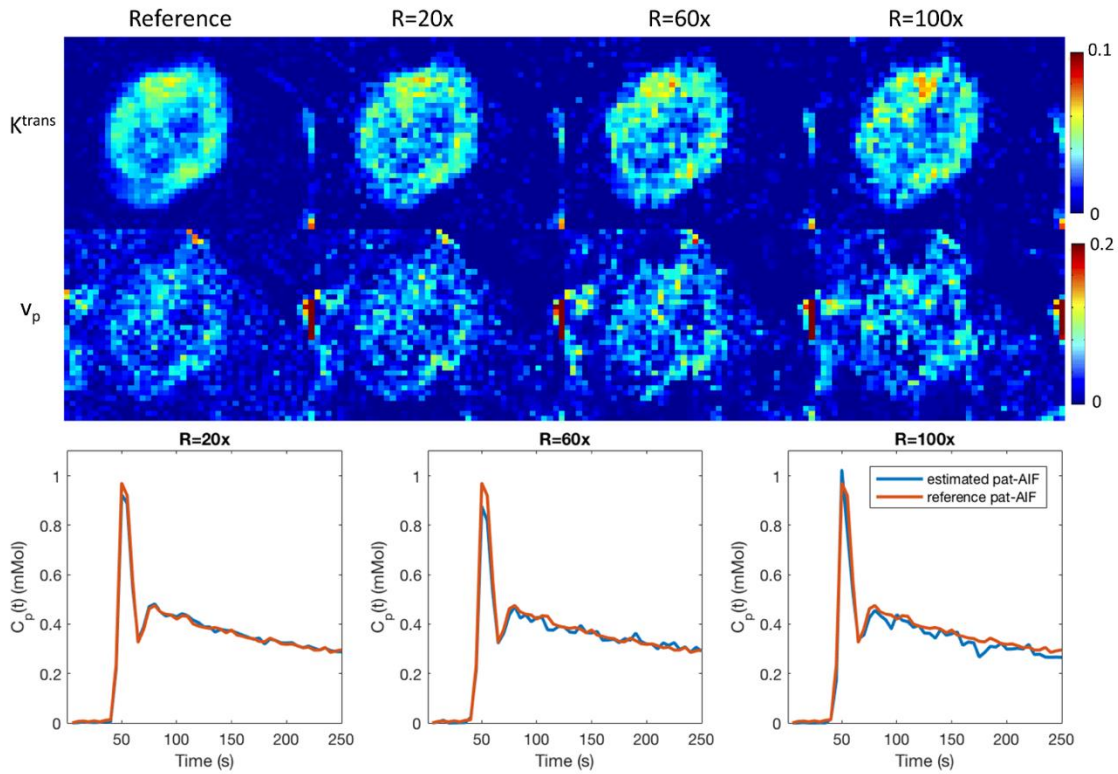
Figure 5.6 Joint reconstruction of TK maps (cropped portion of the case in Figure 5) and AIF at R=20×, 60× and 100×. Comparing to the fully-sampled reference, the proposed method is able to restore both AIF and TK maps at the same time, even at a high under-sampling rate of 100×.

Figure 5.7 show the quantitative evaluation of joint AIF and TK reconstruction across the 4 data sets. Based on the relative rMSE of the TK maps, good-quality TK maps can be restored even at R=100x, with a relative rMSE less than 20%. Multiple noise realizations show that the method is robust noise, with an expected increase in variance at higher under-sampling rates. The shape of the AIF can be estimated at up to R=100×, with AIF rMSE below 0.08 mMol. The peak of the AIF shows larger variance for different noise realization, since the peak is only one point. However, the proposed method is still able to restore the AIF peak up to R=60× with the error at most 0.25mMol across all cases.
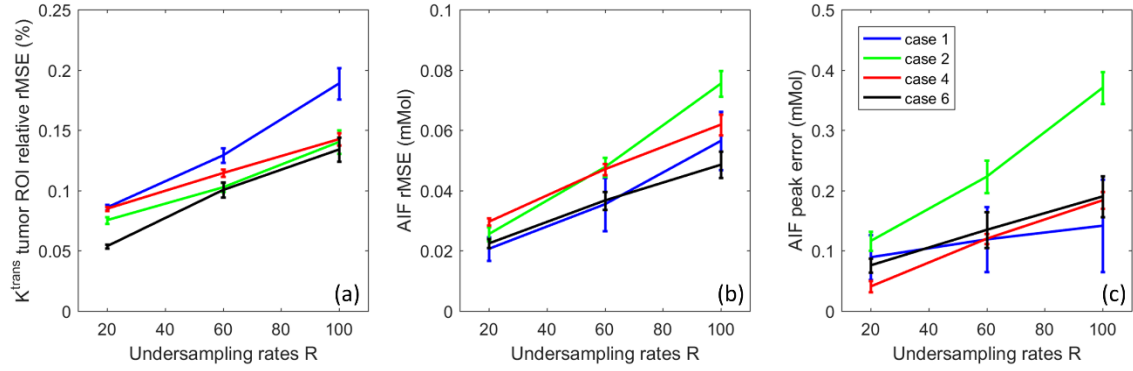
Figure 5.7 Quantitative evaluation of the joint AIF and TK reconstruction for the 4 cases across R=20×, 60× and 100×. (a) K^{trans} relative rMSE was calculated as the spatial rMSE across all tumor pixels, divided by the 90 percentile of the reference tumor K^{trans} value. (b) AIF rMSE was calculated as the temporal rMSE with respect to the reference AIF. (c) AIF peak error was calculated as the reference peak minus the estimated peak. Across different ceases, the rMSE mean and variance all increased with under-sampling rate, as expected.

Figure 5.8 shows reconstruction of pat-AIF and TK maps from prospectively under-sampled data. This demonstrates that whole-brain TK maps can be reconstructed jointly with patient-specific AIF, with no obvious undersampling artifacts in the final TK maps. The clinically-meaningful benefits of under-sampling can be best demonstrated in prospective study, where arbitrary reformats of the 3D TK maps are made possible thanks to the ability to achieve high spatial resolution and whole-brain coverage.
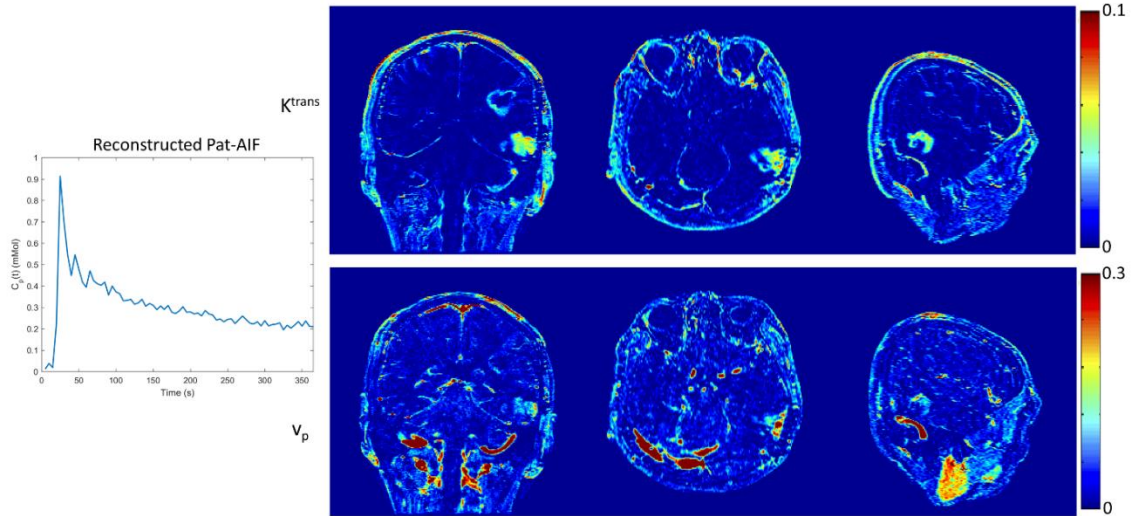

Figure 5.8 Joint reconstruction of Pat-AIF and TK maps from prospective under-sampled data. Whole-brain high-resolution TK maps can be provided together with patient-specific AIF using the proposed model-based reconstruction approach.

5.5 Discussion

We have described, demonstrated, and evaluated a novel model-based reconstruction approach for DCE-MRI, where the TK model is posed as a penalized consistency constraint. By this formulation, we decoupled the TK model consistency from the (k,t)-space data consistency. The two sub-problems can be solved using existing techniques, namely TK modeling (including AIF estimation) and regularized SENSE reconstruction. The proposed approach allows for easy inclusion of different TK solvers, including third-party solvers, and also allows for joint estimation of the patient-specific AIF. We have demonstrated the robustness of the proposed method in one anatomically-realistic brain-tumor DRO, and retrospective study across nine brain tumor DCE-MRI datasets. We also demonstrated the application of the proposed method to prospectively under-sampled data.

Limitations of the Study: The proposed method also has a few important limitations. First, the alternating algorithm proposed is a two-loop iteration, where an iterative solver is needed for each sub-problem. Comparing to a gradient-based direct reconstruction (118), this formulation takes longer computing time. This issue can be addressed by using powerful computers, implementing in C, or using GPU acceleration.

Second, although we demonstrate that the proposed method is compatible with a third-party solver, it requires that the solver does not use any linearization or approximation for the modeling. For complicated TK models, a few linearized approaches have been proposed for fast computation (129, 130). Unfortunately, those methods cannot be integrated into the proposed framework.

Third, although we have shown that this method can include different TK solver, it may be difficult to use a nested model that selects between several different local model based on local fitting errors (39). This type of approach has been shown in recent literature to be advantageous. The quality of intermediate anatomic images in the proposed method, especially in the first few iterations, may make it challenging to generate a modeling mask needed for nested models

5.6 Conclusion

We have demonstrated a novel model-based reconstruction approach for accelerated DCE-MRI. Posing the TK model as a model consistency constraint, this formulation provides flexible use of different TK solvers, joint estimation of patient-specific AIF, and straightforward implementation. Evaluated in digital reference object, retrospective and

prospective study of actual brain tumor patient data, this method provides good quality TK maps and pat-AIF up to under-sampling rates of 100x for both Patlak and eTofts model.

5.7   Appendix 5-A

For the proposed method, we used an alternative approach to solve C and θ from under-sampled k-space, and this appendix explains the detailed steps for sub-problems in Equation (5.3) and Equation (5.4).

In Equation (5.3), we solve the contrast concentration from the measured data using the following equation:

$$C^{n+1} = \arg\min_{C} \| AC - b \|_2^2 + \beta \| P(\theta^n) - C \|_2^2 \qquad (5.A1)$$

Here $A=UFE\Psi$, and we first solve the image difference (ΔS) from b (since we moved S_0 to b) by solving the following least-square problems using CG (or other iterative algorithm for least-square problems). We can use result from previous iteration as initial guess for faster convergence.

$$\Delta S = \arg\min_{\Delta S} \| UFE(\Delta S) - b \|_2^2 + \| \Delta S - \psi P(\theta^n) \|_2^2 \qquad (5.A2)$$

The first term is SENSE, and the second term is an identity constraint to $\Psi P(\theta^n)$ that is constant in this step. P is the forward modeling from TK maps to contrast concentration C, and Ψ is the conversion from contrast concentration C to signal difference ΔS following the steady-state SPGR signal equation:

$$\Delta S = \psi(C) = \frac{M_0 \sin\alpha(1 - e^{-TR \cdot (R_0 + C \cdot r_1)})}{1 - \cos\alpha e^{-TR \cdot (R_0 + C \cdot r_1)}} - \frac{M_0 \sin\alpha(1 - e^{-TR \cdot R_0})}{1 - \cos\alpha e^{-TR \cdot R_0}} \qquad (5.A3)$$

Where TR is the repetition time, α is the flip angle, r_1 is the contrast agent relaxivity. R_0 and M_0 are the pre-contrast R_1 (reciprocal of T_1) and the equilibrium longitudinal magnetization that are estimated from a T_1 mapping sequence. In this work, we used DESPOT1 (29) prior to the DCE-MRI scan.

Note that Ψ is a one-to-one mapping for each voxel, and its inversion ($C = \Psi^{-1}(\Delta S)$) is:

$$R_t = -\frac{1}{TR} \ln \frac{1 - \left(\dfrac{\Delta S}{M_0 \sin \alpha} + \dfrac{1 - e^{-TR \cdot R_0}}{1 - \cos \alpha e^{-TR \cdot R_0}} \right)}{1 - \cos \alpha \left(\dfrac{\Delta S}{M_0 \sin \alpha} + \dfrac{1 - e^{-TR \cdot R_0}}{1 - \cos \alpha e^{-TR \cdot R_0}} \right)} \tag{5.A5}$$

$$C = (R_t - R_0)/r_1$$

Equation (5.A5) is used to compute C after solving for ΔS using Equation (5.A2), this completes the detailed algorithm for solving Equation (5.3).

After C (C(t) used in this equation to avoid confusion) is estimated, Equation (5.4) represents backward TK modelling. For Patlak model, it is:

$$C(t) = P(\theta) = P(K^{trans}, v_p) = K^{trans} \int_0^t C_p(\tau) \, d\tau + v_p C_p(t) \tag{5.A6}$$

Where $C_p(t)$ is the arterial input function (AIF). Patlak model is linear, and a pseudo-inverse can be used to solve $\theta = P^{-1}(C)$.

And for extended-Tofts (eTofts) model, it is:

$$C(t) = P(\theta) = P(K^{trans}, v_p, K_{ep}) = K^{trans} \int_0^t C_p(\tau) e^{-K_{ep}(t-\tau)} \, d\tau + v_p C_p(t) \tag{5.A7}$$

where an extra TK parameter K_{ep} is modeled for better fitting. eTofts is nonlinear and iterative algorithm can be used to solve this model fitting:

$$\theta = \arg \min_\theta \| P(\theta) - C \|_2^2 \tag{5.A8}$$

We use a gradient-based l-BFGS algorithm to solve Equation (5.A8), where we derive the gradient for each TK parameter. Open-source toolbox, Rocketship, was also used for comparison.

Chapter 6. Conclusion

In this thesis, we proposed several novel methods targeted to improve brain DCE-MRI towards high-resolution, whole-brain coverage, and high-fidelity TK maps. DCE-MRI is a valuable dynamic imaging technique that is able to provide powerful biomarker for evaluation of brain tumor, helping diagnosis and therapy response. However, DCE-MRI is not currently the standard-of-care protocol in many centers conducting oncology, due to its low resolution, limited spatial coverage, and low reproducibility for kinetic parameter mapping.

We have proposed a specially tailored constrained reconstruction technique for DCE-MRI in chapter 3. The sampling scheme, sparsifying transform constraints and the reconstruction algorithm are all specially tailored for dynamic imaging to provide truthful dynamic information from vastly under-sampled data. We have conducted the first (to the best of our knowledge) evaluation of prospectively undersampling reconstruction of DCE-MRI in brain tumor patients, and compared to conventional technique that is sampled at Nyquist rate. With 30× under-sampling rate, we were able to achieve a whole-brain high-resolution DCE-MRI. In radiologists' rating, the de-noising properties of the sparsifying constraints also provided improved dynamic image quality in terms of fine details and signal-to-noise ratio comparing to conventional imaging technique. The high-resolution, whole-brain coverage enabled us 3D imaging in any arbitrary plane, providing a complete pathological depiction of some large Glioblastoma tumor, or scattered lesions that spread the whole-brain like metastatic brain tumor.

In chapter 4, We proposed an innovative and rigorous technical development approach in which DCE-MRI acquisition and reconstruction are tailored from an estimation-theoretic point of view to create the most reproducible tracker kinetic (TK) parameter maps. Unlike conventional approaches that optimize the quality of intermediate dynamic images, our proposed methods fully integrated TK models with DCE-MRI acquisition and reconstruction. The TK maps were directly estimated from under-sampled k-space data, and the TK model was implicitly enforced during the reconstruction process. Comparing to earlier indirect method using state-of-the-art compressed sensing techniques, this direct reconstruction technique is able to provide even higher under-sampling rates and better quality TK parameter maps. We have shown up to 100× under-sampling rate in retrospective study, a rate that is never reported in DCE-MRI literature. This ultra-high rate can enable us to further improve the spatio-temporal resolution of DCE-MRI, achieving sub-millimeter isotropic resolution with close to 1 second temporal resolution. We have

also shown the feasibility of the direct reconstruction in prospective under-sampled data, where whole-brain high-resolution TK maps can be reconstructed directly from 30× under-sampled *k*-space.

In chapter 5, we developed and evaluated a model-based DCE-MRI reconstruction framework for joint arterial input function (AIF) and kinetic parameter estimation from under-sampled data. This method poses the TK model as a model consistency constraint, enabling the inclusion of different TK solvers and the joint estimation of the arterial input function (AIF) from highly under-sampled data. Comparing to previously proposed indirect constrained reconstruction, or direct model-based reconstruction, this model consistency constrained reconstruction combined the benefits of both methods, while overcoming the limitations of both methods. By posing the TK model as a model consistency constraint instead of directly forcing the model. The framework can allow for model deviation and provide better quality TK maps. It decouples the direct reconstruction problem into two well-defined sub-problems, thus greatly reducing the complexity of the algorithm. Benefiting from the intermediate images similar to indirect reconstruction, the proposed method also allows for easy inclusion of different TK solver, and joint estimation of AIF from under-sampled data. In digital reference object study, the proposed method is shown to be compatible with a third-party TK solver. In the retrospective study, the proposed method is demonstrated to produce TK maps and patient-specific AIF with minimal error at up to R=100× for both Patlak and eTofts model. In prospective study, the proposed method was able to provide high-resolution whole-brain TK maps and patient-specific AIF at R=30×.

The proposed methods in this dissertation are still far from providing a complete and universal DCE-MRI approaches, especially in clinical translation practice. Several limitations and possible improvement exist to further facilitate the clinical translation of improved DCE-MRI, some of them were discussed in previous chapters. For example, a rigorous reproducibility study is still lacking to prove the proposed method is able to provide reproducible TK mapping in the same patients. For higher under-sampling rate up to 100×, prospective study was not performed to validate if higher spatial or temporal resolution can truly be achieved. Also, the TK model selection is not perfect in the proposed study, and a spatial information based model selection is still a challenging in the proposed methods.

References

1. Centers for Disease Control and Prevention [http://www.cdc.gov/nchs/fastats/leading-causes-of-death.htm]
2. Brain Tumor: Diagnosis [http://www.cancer.net/cancer-types/brain-tumor/diagnosis]
3. Ricard D, Idbaih A, Ducray F, Lahutte M, Hoang-Xuan K, Delattre JY: Primary brain tumours in adults. *Lancet* 2012; 379:1984–1996.
4. Ellingson BM, Bendszus M, Boxerman J, et al.: Consensus recommendations for a standardized Brain Tumor Imaging Protocol in clinical trials. *Neuro Oncol* 2015; 17(August):1188–1198.
5. Essig M, Nguyen TB, Shiroishi MS, et al.: Perfusion MRI: the five most frequently asked clinical questions. *AJR Am J Roentgenol* 2013; 201:W495-510.
6. Wen PY, Macdonald DR, Reardon D a., et al.: Updated response assessment criteria for high-grade gliomas: Response assessment in neuro-oncology working group. *J Clin Oncol* 2010; 28:1963–1972.
7. Lin NU, Lee EQ, Aoyama H, et al.: Response assessment criteria for brain metastases: proposal from the RANO group. *Lancet Oncol* 2015; 16:e270–e278.
8. Heye AK, Culling RD, Hernández CV, Thrippleton MJ, Wardlaw JM: Assessment of blood – brain barrier disruption using dynamic contrast-enhanced MRI . A systematic review. *NeuroImage:Clinical* 2014; 6:262–274.
9. Tofts PS, Brix G, Buckley DL, et al.: Estimating kinetic parameters from dynamic contrast-enhanced T(1)-weighted MRI of a diffusable tracer: standardized quantities and symbols. *J Magn Reson Imaging* 1999; 10:223–32.
10. Law M, Yang S, Babb JS, et al.: Comparison of cerebral blood volume and vascular permeability from dynamic susceptibility contrast-enhanced perfusion MR imaging with glioma grade. *Am J Neuroradiol* 2004; 25:746–755.
11. Larsson C, Kleppestø M, Grothe I, Vardal J, Bjørnerud A: T1 in high-grade glioma and the influence of different measurement strategies on parameter estimations in DCE-MRI. *J Magn Reson Imaging* 2014; 0.
12. DCE MRI Technical Committee. DCE MRI Quantification Profile, Quantitative Imaging Biomarkers Alliance. Version 1.0. Reviewed Draft. QIBA, July 1, 2012. [http://rsna.org/QIBA_.aspx]
13. Weishaupt D, Köchli VD, Marincek B: *How Does MRI Work?* 2008.
14. Stanisz GJ, Odrobina EE, Pun J, et al.: T1, T2 relaxation and magnetization transfer in tissue at 3T. *Magn Reson Med* 2005; 54:507–12.
15. Wansapura JP, Holland SK, Dunn RS, Ball WS: NMR relaxation times in the human brain at 3.0 tesla. *J Magn Reson Imaging* 1999; 9:531–538.
16. Chen L, Bernstein M: Measurements of T1 relaxation times at 3.0 T: implications for clinical MRA. *Proc 9th …* 2001; 9:2001.
17. Pruessmann KP, Weiger M, Scheidegger MB, Boesiger P: SENSE: sensitivity encoding for fast MRI. *Magn Reson Med* 1999; 42:952–962.
18. Griswold MA, Jakob PM, Heidemann RM, et al.: Generalized autocalibrating partially parallel acquisitions (GRAPPA). *Magn Reson Med* 2002; 47:1202–1210.
19. Lustig M, Pauly JM: SPIRiT: Iterative self-consistent parallel imaging reconstruction from arbitrary k-space. *Magn Reson Med* 2010; 64:457–71.

20. Uecker M, Lai P, Murphy MJ, et al.: ESPIRiT-an eigenvalue approach to autocalibrating parallel MRI: Where SENSE meets GRAPPA. *Magn Reson Med* 2014; 71:990–1001.
21. Haldar JP: Low-rank modeling of local k-space neighborhoods (LORAKS) for constrained MRI. *IEEE Trans Med Imaging* 2014; 33:668–81.
22. Tofts PS, Kermode AG: Measurement of the blood-brain barrier permeability and leakage space using dynamic MR imaging. 1. Fundamental concepts. *Magn Reson Med* 1991; 17:357–67.
23. Cramer SP, Larsson HBW: Accurate determination of blood-brain barrier permeability using dynamic contrast-enhanced T1-weighted MRI: a simulation and in vivo study on healthy subjects and multiple sclerosis patients. *J Cereb blood flow Metab* 2014; 34:1655–1665.
24. Yang S, Law M, Zagzag D, et al.: Dynamic contrast-enhanced perfusion MR imaging measurements of endothelial permeability: differentiation between atypical and typical meningiomas. *AJNR Am J Neuroradiol* 2003; 24:1554–9.
25. Cramer SP, Simonsen H, Frederiksen JL, Rostrup E, Larsson HBW: Abnormal blood-brain barrier permeability in normal appearing white matter in multiple sclerosis investigated by MRI. *NeuroImage Clin* 2014; 4:182–189.
26. Montagne A, Barnes SR, Law M, et al.: Blood-Brain Barrier Breakdown in the Aging Human Report Blood-Brain Barrier Breakdown in the Aging Human Hippocampus. *Neuron* 2015; 85:296–302.
27. Cunningham CH, Pauly JM, Nayak KS: Saturated double-angle method for rapid B1+ mapping. *Magn Reson Med* 2006; 55:1326–1333.
28. Sacolick LI, Wiesinger F, Hancu I, Vogel MW: B   1 mapping by Bloch-Siegert shift. *Magn Reson Med* 2010; 63:1315–1322.
29. Deoni SCL, Peters TM, Rutt BK: High-resolution T1 and T2 mapping of the brain in a clinically acceptable time with DESPOT1 and DESPOT2. *Magn Reson Med* 2005; 53:237–41.
30. Pruessmann KP, Weiger M, Börnert P, Boesiger P: Advances in sensitivity encoding with arbitrary k-space trajectories. *Magn Reson Med* 2001; 46:638–651.
31. Li KL, Zhu XP, Waterton J, Jackson a: Improved 3D quantitative mapping of blood volume and endothelial permeability in brain tumors. *J Magn Reson Imaging* 2000; 12:347–57.
32. Fluckiger JU, Schabel MC, DiBella EVR: Model-based blind estimation of kinetic parameters in Dynamic Contrast Enhanced (DCE)-MRI. *Magn Reson Med* 2009; 62:1477–1486.
33. Shi L, Wang D, Liu W, et al.: Automatic detection of arterial input function in dynamic contrast enhanced MRI based on affinity propagation clustering. *J Magn Reson Imaging* 2014:1327–37.
34. Van Osch MJP, Vonken EJP a, Bakker CJG, Viergever M a.: Correcting partial volume artifacts of the arterial input function in quantitative cerebral perfusion MRI. *Magn Reson Med* 2001; 45:477–485.
35. Henderson E, Rutt BK, Lee TY: Temporal sampling requirements for the tracer kinetics modeling of breast disease. *Magn Reson Imaging* 1998; 16:1057–1073.
36. Parker GJM, Roberts C, Macdonald A, et al.: Experimentally-derived functional form for a population-averaged high-temporal-resolution arterial input function for dynamic

contrast-enhanced MRI. *Magn Reson Med* 2006; 56:993–1000.

37. Calamante F, Gadian DG, Connelly A: Delay and dispersion effects in dynamic susceptibility contrast MRI: simulations using singular value decomposition. *Magn Reson Med* 2000; 44:466–73.

38. Shiroishi MS, Habibi M, Rajderkar D, et al.: Perfusion and permeability MR imaging of gliomas. *Technol Cancer Res Treat* 2011; 10:59–71.

39. Bagher-ebadian H, Jain R, Nejad-davarani SP, et al.: Model Selection for DCE-T1 Studies in Glioblastoma. *Magn Reson Med* 2012:241–251.

40. Sourbron SP, Buckley DL: Classic models for dynamic contrast-enhanced MRI. *NMR Biomed* 2013; 26:1004–1027.

41. Sourbron S, Ingrisch M, Siefert A, Reiser M, Herrmann K: Quantification of cerebral blood flow, cerebral blood volume, and blood-brain-barrier leakage with DCE-MRI. *Magn Reson Med* 2009; 62:205–217.

42. Sourbron SP, Buckley DL: On the scope and interpretation of the Tofts models for DCE-MRI. *Magn Reson Med* 2011; 66:735–745.

43. Sodickson DK, Manning WJ: Simultaneous acquisition of spatial harmonics (SMASH): fast imaging with radiofrequency coil arrays. *Magn Reson Med* 1997; 38:591–603.

44. Lustig M, Donoho D, Pauly JM: Sparse MRI: The application of compressed sensing for rapid MR imaging. *Magn Reson Med* 2007; 58:1182–1195.

45. Awate SP, DiBella EVR: Spatiotemporal dictionary learning for undersampled dynamic MRI reconstruction via joint frame-based and dictionary-based sparsity. In *Biomed Imaging*; 2012:318–321.

46. Caballero J, Price AN, Rueckert D, Hajnal J V: Dictionary learning and time sparsity for dynamic MR data reconstruction. *IEEE Trans Med Imaging* 2014; 33:979–94.

47. Gamper U, Boesiger P, Kozerke S: Compressed sensing in dynamic MRI. *Magn Reson Med* 2008; 59:365–373.

48. Jung H, Sung K, Nayak KS, Kim EY, Ye JC: k-t FOCUSS: a general compressed sensing framework for high resolution dynamic MRI. *Magn Reson Med* 2009; 61:103–16.

49. Feng L, Grimm R, Block KT, et al.: Golden-Angle Radial Sparse Parallel MRI: Combination of Compressed Sensing, Parallel Imaging, and Golden-Angle Radial Sampling for Fast and Flexible Dynamic Volumetric MRI. *Magn Reson Med* 2014; 72:707–717.

50. Zhang T, Cheng JY, Potnick AG, et al.: Fast pediatric 3D free-breathing abdominal dynamic contrast enhanced MRI with high spatiotemporal resolution. *J Magn Reson Imaging* 2015; 41:460–473.

51. Wang H, Miao Y, Zhou K, et al.: Feasibility of high temporal resolution breast DCE-MRI using compressed sensing theory. *Med Phys* 2010; 37:4971.

52. Rosenkrantz AB, Geppert C, Grimm R, et al.: Dynamic contrast-enhanced MRI of the prostate with high spatiotemporal resolution using compressed sensing, parallel imaging, and continuous golden-angle radial sampling: Preliminary experience. *J Magn Reson Imaging* 2015; 41:1365–1373.

53. Winkelmann S, Schaeffter T, Koehler T, Eggers H, Doessel O: An optimal radial profile order based on the Golden Ratio for time-resolved MRI. *IEEE Trans Med Imaging* 2007; 26:68–76.

54. Yeh EN, Stuber M, McKenzie C a, et al.: Inherently self-calibrating non-Cartesian

parallel imaging. *Magn Reson Med* 2005; 54:1–8.

55. Lustig M, Donoho D, Pauly JM: Sparse MRI: The application of compressed sensing for rapid MR imaging. *Magn Reson Med* 2007; 58:1182–95.

56. Lebel RM, Jones J, Ferre J-C, Law M, Nayak KS: Highly accelerated dynamic contrast enhanced imaging. *Magn Reson Med* 2014; 71:635–644.

57. Zhu Y, Guo Y, Lingala SG, Lebel RM, Law M, Nayak KS: GOCART: GOlden-angle CArtesian randomized time-resolved 3D MRI. *Magn Reson Imaging* 2016; 34:940–950.

58. Lin F-H, Wang F-N, Ahlfors SP, Hämäläinen MS, Belliveau JW: Parallel MRI reconstruction using variance partitioning regularization. *Magn Reson Med* 2007; 58:735–744.

59. Lustig M, Donoho DL, Santos JM, Pauly JM: Compressed Sensing MRI. (March 2008):72–82.

60. O'Connor JPB, Jackson A, Parker GJM, Roberts C, Jayson GC: Dynamic contrast-enhanced MRI in clinical trials of antivascular therapies. *Nat Rev Clin Oncol* 2012; 9:167–77.

61. Larsson HB, Stubgaard M, Frederiksen JL, Jensen M, Henriksen O, Paulson OB: Quantitation of blood-brain barrier defect by magnetic resonance imaging and gadolinium-DTPA in patients with multiple sclerosis and brain tumors. *Magn Reson Med* 1990; 16:117–131.

62. Khouli RH El, Macura KJ, Jacobs MA, et al.: Dynamic Contrast-Enhanced MRI of the Breast: Quantitative Method for Kinetic Curve Type Assessment. *Am J Roentgenol* 2009; 193:295–300.

63. Rosenkrantz AB, Lim RP, Haghighi M, Somberg MB, Babb JS, Taneja SS: Comparison of interreader reproducibility of the prostate imaging reporting and data system and likert scales for evaluation of multiparametric prostate MRI. *AJR Am J Roentgenol* 2013; 201:W612-8.

64. Paldino MJ, Barboriak DP: Fundamentals of Quantitative Dynamic Contrast-Enhanced MR Imaging. *Magn Reson Imaging Clin N Am* 2009:277–289.

65. Miller JC, Pien HH, Sahani D, Sorensen AG, Thrall JH: Imaging angiogenesis: applications and potential for drug development. *J Natl Cancer Inst* 2005; 97:172–187.

66. Thomas AA, Arevalo-Perez J, Kaley T, et al.: Dynamic contrast enhanced T1 MRI perfusion differentiates pseudoprogression from recurrent glioblastoma. *J Neurooncol* 2015; 125:183–190.

67. Barger A V, Block WF, Toropov Y, Grist TM, Mistretta CA: Time-resolved contrast-enhanced imaging with isotropic resolution and broad coverage using an undersampled 3D projection trajectory. *Magn Reson Med* 2002; 48:297–305.

68. Haider CR, Hu HH, Campeau NG, Huston J, Riederer SJ: 3D high temporal and spatial resolution contrast-enhanced MR angiography of the whole brain. *Magn Reson Med* 2008; 60:749–760.

69. Trzasko JD, Haider CR, Borisch EA, et al.: Sparse-CAPR: highly accelerated 4D CE-MRA with parallel imaging and nonconvex compressive sensing. *Magn Reson Med* 2011; 66:1019–32.

70. Lee GR, Seiberlich N, Sunshine JL, Carroll TJ, Griswold MA: Rapid time-resolved magnetic resonance angiography via a multiecho radial trajectory and GraDeS reconstruction. *Magn Reson Med* 2013; 69:346–359.

71. Doneva M, Stehning C, Nehrke K, Börnert P: Improving Scan Efficiency of

Respiratory Gated Imaging Using Compressed Sensing with 3D Cartesian Golden Angle Sampling. In *ISMRM*. *Volume 19*; 2011:641.

72. Zhu Y, Guo Y, Lebel RM, Law M, Nayak KS: Randomized Golden Ratio Sampling For Highly Accelerated Dynamic Imaging. In *ISMRM*; 2014:4365.

73. Deoni SCL: High-resolution T1 mapping of the brain at 3T with driven equilibrium single pulse observation of T1 with high-speed incorporation of RF field inhomogeneities (DESPOT1-HIFI). *J Magn Reson Imaging* 2007; 26:1106–11.

74. Ramani S, Fessler JA: Parallel MR image reconstruction using augmented Lagrangian methods. *IEEE Trans Med Imaging* 2011; 30:694–706.

75. Afonso M V, Bioucas-Dias JM, Figueiredo MAT: Fast image recovery using variable splitting and constrained optimization. *IEEE Trans Image Process* 2010; 19:2345–56.

76. Afonso M V, Bioucas-Dias JM, Figueiredo MAT: An augmented Lagrangian approach to the constrained optimization formulation of imaging inverse problems. *IEEE Trans Image Process* 2011; 20:681–95.

77. Hansen PC, Dianne Prost O'Leary: The use of the l-curve in the regularization of discrete ill-posed problems. *Soc Ind Appl Math* 1993; 14:1487–1503.

78. Sourbron SP, Buckley DL: On the scope and interpretation of the Tofts models for DCE-MRI. *Magn Reson Med* 2011; 66:735–45.

79. Ewing JR, Knight RA, Nagaraja TN, et al.: Patlak plots of Gd-DTPA MRI data yield blood-brain transfer constants concordant with those of 14C-sucrose in areas of blood-brain opening. *Magn Reson Med* 2003; 50:283–292.

80. Yun TJ, Park CK, Kim TM, et al.: Glioblastoma treated with concurrent radiation therapy and temozolomide chemotherapy: differentiation of true progression from pseudoprogression with quantitative dynamic contrast-enhanced MR imaging. *Radiology* 2015; 274:830–840.

81. Kickingereder P, Wiestler B, Graf M, et al.: Evaluation of dynamic contrast-enhanced MRI derived microvascular permeability in recurrent glioblastoma treated with bevacizumab. *J Neurooncol* 2015; 121:373–380.

82. Bonekamp D, Deike K, Wiestler B, et al.: Association of overall survival in patients with newly diagnosed glioblastoma with contrast-enhanced perfusion MRI: Comparison of intraindividually matched T1 - and T2 (*) -based bolus techniques. *J Magn Reson Imaging* 2014; 42:87–96.

83. Chang SG, Yu B, Vetterli M: Adaptive wavelet thresholding for image denoising and compression. *IEEE Trans Image Process* 2000; 9:1532–1546.

84. Elad M, Aharon M: Image denoising via sparse and redundant representations over learned dictionaries. *IEEE Trans Image Process* 2006; 15:3736–45.

85. Chan SH, Khoshabeh R, Gibson KB, Gill PE, Nguyen TQ: An Augmented Lagrangian Method for Total Variation Video Restoration. *IEEE Trans Image Process* 2011; 20:3097–3111.

86. Zhang T, Pauly JM, Vasanawala SS, Lustig M: Coil compression for accelerated imaging with Cartesian sampling. *Magn Reson Med* 2013; 69:571–82.

87. Gai J, Obeid N, Holtrop JL, et al.: More IMPATIENT: A Gridding-Accelerated Toeplitz-based Strategy for Non-Cartesian High-Resolution 3D MRI on GPUs. *J Parallel Distrib Comput* 2013; 73:686–697.

88. Frahm J, Schätz S, Untenberger M, et al.: On the Temporal Fidelity of Nonlinear Inverse Reconstructions for Real- Time MRI – The Motion Challenge. *Open Med*

Imaging J 2014; 8:1–7.

89. Wech T, Stab D, Budich JC, et al.: Resolution evaluation of MR images reconstructed by iterative thresholding algorithms for compressed sensing. *Med Phys* 2012; 39:4328–38.

90. Zhu Y, Guo Y, Lingala SG, et al.: Evaluation of DCE-MRI data sampling, reconstruction and model fitting using digital brain phantom. In *Proc Int Soc Magn Reson Med*; 2015:3070.

91. Bosca RJ, Jackson EF: An extensible methodology for creating realistic anthropomorphic digital phantoms for quantitative imaging algorithm comparisons and validation. In *ISMRM*; 2015:797.

92. Guo Y, Lebel RM, Zhu Y, et al.: High-resolution whole-brain DCE-MRI using constrained reconstruction: Prospective clinical evaluation in brain tumor patients. *Med Phys* 2016; 43:2013–2023.

93. Chandarana H, Feng L, Ream J, et al.: Respiratory Motion-Resolved Compressed Sensing Reconstruction of Free-Breathing Radial Acquisition for Dynamic Liver Magnetic Resonance Imaging. *Invest Radiol* 2015; 50:749–756.

94. Haldar JP, Hernando D, Liang Z: Super-resolution Reconstruction of MR Image Sequences with Contrast Modeling. *IEEE Int Symp Biomed Imaging From Nano to Macro* 2009:266–269.

95. Ma D, Gulani V, Seiberlich N, et al.: Magnetic resonance fingerprinting. *Nature* 2013; 495:187–92.

96. Welsh CL, Dibella EVR, Adluru G, Hsu EW: Model-based reconstruction of undersampled diffusion tensor k-space data. *Magn Reson Med* 2013; 70:429–440.

97. Sumpf TJ, Uecker M, Boretius S, Frahm J: Model-based nonlinear inverse reconstruction for T2 mapping using highly undersampled spin-echo MRI. *J Magn Reson Imaging* 2011; 34:420–8.

98. Zhao B, Lam F, Liang ZP: Model-based MR parameter mapping with sparsity constraints: Parameter estimation and performance bounds. *IEEE Trans Med Imaging* 2014; 33:1832–1844.

99. Peng X, Liu X, Zheng H, Liang D: Exploiting parameter sparsity in model-based reconstruction to accelerate proton density and T2 mapping. *Med Eng Phys* 2014; 36:1428–1435.

100. Wang G, Qi J: Direct estimation of kinetic parametric images for dynamic PET. *Theranostics* 2013:802–815.

101. Kamasak ME, Bouman C a, Morris ED, Sauer K: Direct reconstruction of kinetic parameter images from dynamic PET data. *IEEE Trans Med Imaging* 2005; 24:636–50.

102. Lin Y, Haldar J, Li Q, Conti P, Leahy R: Sparsity Constrained Mixture Modeling for the Estimation of Kinetic Parameters in Dynamic PET. *IEEE Trans Med Imaging* 2013; 33:173–185.

103. Felsted BK, Whitaker RT, Schabel M, DiBella EVR: Model-based reconstruction for undersampled dynamic contrast-enhanced MRI. *Proc SPIE* 2009; 7262:1–10.

104. Dikaios N, Arridge S, Hamy V, Punwani S, Atkinson D: Direct parametric reconstruction from undersampled (k, t)-space data in dynamic contrast enhanced MRI. *Med Image Anal* 2014; 18:989–1001.

105. Lebel RM, Guo Y, Zhu Y, et al.: The comprehensive contrast-enhanced neuro exam. In *Proc Int Soc Magn Reson Med*; 2015:3705.

106. Liu DC, Nocedal J: On the limited memory BFGS method for large scale optimization. *Math Program* 1989; 45:503–528.

107. Shellock FG, Kanal E: Guidelines and recommendations for MR imaging safety and patient management. III. Questionnaire for screening patients before MR procedures. *J Magn Reson Imaging* 1994; 4:749–751.

108. Kanal E, Barkovich AJ, Bell C, et al.: ACR guidance document for safe MR practices: 2007. *Am J Roentgenol* 2007; 188:1447–1474.

109. Stanisz GJ, Henkelman RM: Gd-DTPA relaxivity depends on macromolecular content. *Magn Reson Med* 2000; 44:665–667.

110. De Naeyer D, De Deene Y, Ceelen WP, Segers P, Verdonck P: Precision analysis of kinetic modelling estimates in dynamic contrast enhanced MRI. *MAGMA* 2011; 24:51–66.

111. Dikaios N, Punwani S, Atkinson D: Direct parametric reconstruction from (k, t)-space data in dynamic contrast enhanced MRI. In *Proc Int Soc Magn Reson Med*; 2015:3706.

112. Dickie BR, Banerji A, Kershaw LE, et al.: Improved accuracy and precision of tracer kinetic parameters by joint fitting to variable flip angle and dynamic contrast enhanced MRI data. *Magn Reson Med* 2015; 76:1270–1281.

113. Lingala S, Hu Y, DiBella E, Jacob M: Accelerated Dynamic MRI Exploiting Sparsity and Low-Rank Structure: k-t SLR. *IEEE Trans Med Imaging* 2011; 30:1042–1054.

114. Hu Y, Lingala SG, Jacob M: A fast majorize-minimize algorithm for the recovery of sparse and low-rank matrices. *IEEE Trans Image Process* 2012; 21:742–53.

115. Miao X, Lingala SG, Guo Y, Jao T, Nayak KS: Accelerated Cardiac Cine Using Locally Low Rank and Total Variation Constraints. In *Proc Int Soc Magn Reson Med*; 2015:571.

116. O'Connor JPB, Jackson A, Parker GJM, Roberts C, Jayson GC: Dynamic contrast-enhanced MRI in clinical trials of antivascular therapies. *Nat Rev Clin Oncol* 2012; 9:167–177.

117. Velikina J V, Alexander AL, Samsonov A: Accelerating MR parameter mapping using sparsity-promoting regularization in parametric dimension. *Magn Reson Med* 2013; 70:1263–73.

118. Guo Y, Lingala SG, Zhu Y, Lebel RM, Nayak KS: Direct Estimation of Tracer-Kinetic Parameter Maps From Highly Undersampled Brain Dynamic Contrast Enhanced MRI. *Magn Reson Med* 2016.

119. Lingala SG, Guo Y, Zhu Y, Barnes S, Lebel RM, Nayak KS: Accelerated DCE MRI using constrained reconstruction based on pharmaco-kinetic model dictionaries. In *ISMRM*; 2015:196.

120. Port RE, Knopp M V., Brix G: Dynamic contrast-enhanced MRI using Gd-DTPA: Interindividual variability of the arterial input function and consequences for the assessment of kinetics in tumors. *Magn Reson Med* 2001; 45:1030–1038.

121. Samsonov A: A Novel Reconstruction Approach Using Model Consistency Condition for Accelerated Quantitative MRI (MOCCA). In *ISMRM*; 2012:358.

122. Velikina J V., Samsonov AA: Reconstruction of dynamic image series from undersampled MRI data using data-driven model consistency condition (MOCCO). *Magn Reson Med* 2015; 74:1279–1290.

123. Barnes SR, Ng TSC, Santa-Maria N, Montagne A, Zlokovic B V., Jacobs RE: ROCKETSHIP: a flexible and modular software tool for the planning, processing and

analysis of dynamic MRI studies. *BMC Med Imaging* 2015; 15:19.

124. Barboriak, D. P., J. R. MacFall, A. O. Padua, G. E. York, B. L. Viglianti and MWD": Standardized software for calculation of Ktrans and vp from dynamic T1-weighted MR images. In *Int Soc Magn Reson Med Work MR Drug Dev From Discov to Clin Ther Trials*; 2004.

125. Bosca RJ, Jackson EF: Creating an anthropomorphic digital MR phantom—an extensible tool for comparing and evaluating quantitative imaging algorithms. *Phys Med Biol* 2016; 61:974–982.

126. Jung SC, Yeom JA, Kim J, et al.: Glioma : Application of Histogram Analysis of Pharmacokinetic Parameters from T1-Weighted Dynamic Contrast-Enhanced MR Imaging to Tumor Grading. 2014:1103–1110.

127. Guo Y, Lebel RM, Zhu Y, et al.: High-Resolution Whole-Brain DCE-MRI Using Constrained Reconstruction: Prospective Clinical Evaluation in Brain Tumor Patients. *Med Phys* 2016.

128. Bertsekas DP: Multiplier methods: A survey. *Automatica* 1976; 12:133–145.

129. Murase K: Efficient Method for Calculating Kinetic Parameters Using T 1-Weighted Dynamic Contrast-Enhanced Magnetic Resonance Imaging. *Magn Reson Med* 2004; 51:858–862.

130. Flouri D, Lesnic D, Sourbron SP: Fitting the two-compartment model in DCE-MRI by linear inversion. *Magn Reson Med* 2016; 76:998–1006.